DEVELOPMENT OF A TURBULENT BOUNDARY LAYER DOWNSTREAM OF A TRANSVERSE SQUARE GROOVE

SUTARDI

DEVELOPMENT OF A TURBULENT BOUNDARY LAYER DOWNSTREAM OF A TRANSVERSE SQUARE GROOVE

By

©Sutardi

A thesis submitted to the School of Graduate
Studies in partial fulfillment of the
requirements for the degree of
Master of Engineering

Faculty of Engineering and Applied Science
Memorial University of Newfoundland
October, 1998

St. John's Newfoundland Canada

National Library
of Canada

Acquisitions and
Bibliographic Services

395 Wellington Street
Ottawa ON K1A 0N4
Canada

Bibliothèque nationale
du Canada

Acquisitions et
services bibliographiques

395, rue Wellington
Ottawa ON K1A 0N4
Canada

Your file Votre référence

Our file Notre référence

0-612-36182-9

Abstract

The development of a constant pressure turbulent boundary layer downstream of a transverse square groove has been investigated at two values of momentum thickness Reynolds numbers (R_θ = 1000 and 3000). The ratio of the cavity depth to the boundary layer thickness (d/δ_1) is approximately 0.072. Experiments were performed in a low-speed wind tunnel using hot-wire anemometry. The wall shear stress (τ_w) was estimated from the velocity profiles using the Clauser chart method and by assuming a power-law velocity distribution. The smooth wall results indicate the Clauser chart is better suited at higher R_θ, whereas the power-law is more appropriate at low R_θ. The effect of the groove on τ_w at the lower R_θ is not significant. At the higher R_θ, the effect of the groove on τ_w is more pronounced. There is a sudden increase in τ_w just downstream of the cavity. The increase in τ_w is followed by an undershoot and an oscillatory relaxation back to the smooth wall value. Integration of τ_w in the streamwise direction indicates that there is an increase in drag of 1.0 percent at R_θ = 1000, and no change in drag at R_θ = 3000. The mean velocity profiles, energy spectra, and turbulent kinetic energy dissipation rate are not affected by the presence of the groove. At R_θ = 3000, there is a reduction in the turbulence intensity (u^+) in the near-wall region ($y^+ \lesssim 10$). In the region $y^+ \gtrsim 10$, there is a good collapse of the smooth- and grooved-wall u^+ profiles. At the lower R_θ, the maximum value of u^+ is reduced by about 4% on the grooved-wall. The wake parameter distribution indicates that the boundary layer over the grooved-wall is not in equilibrium at both R_θ. There is a rapid growth of the internal layer immediately downstream of the groove. This is followed by a much slower growth beyond $x/w \gtrsim 7$.

Acknowledgements

I would like to thank the Indonesian Government for supporting my graduate study at Memorial University of Newfoundland. The financial support from May 1996 to May 1998 is gratefully acknowledged.

My deep gratitude goes to my supervisor Dr. Chan Ching for suggesting the research topic. The frequent enthusiastic discussions with Dr. Ching have helped me with my experiments and thesis writing over the last two years. His helpful hand has been completely invaluable and unforgettable.

In addition, I would like to thank Dr. J.J. Sharp, Dr. L. M. Lye, Dr. G. C. W. Sabin, Dr. R. Seshadri, and Dr. M. J. Hinchey for presenting courses which were very useful in my research.

My thanks to N. Aung for providing enthusiastic help with the wind tunnel work. Furthermore, I would like to express my thanks to Darrel Sparkes for his help with the preparation of the test plate in the wind tunnel test section.

Finally, I am indebted to my wife Heni and my son Farhan for their continuous support, encouragement, and understanding.

Table of Contents

List of Figures and Tables

A) List of Figures

B) List of Tables

List of Symbols

General:

C_f : skin friction coefficient

d : cavity depth, or the outside diameter of tube in Preston tube measurements

d^+ : du_τ/ν

f : circular frequency

f_K : Kolmogorov frequency ($\equiv \dfrac{U}{2\pi\eta}$)

k_1 : one-dimensional wave length

l^+ : internal length scale ($\equiv \nu/u_\tau$)

Δp : static pressure at the wall

Δp^+ : normalized wall static pressure ($\equiv \Delta p d^2/(\rho\nu^2)$)

R_θ : Reynolds number based on θ ($\equiv U_\infty\theta/\nu$)

R_x : Reynolds number based on x ($\equiv U_\infty x/\nu$)

s : distance between cavities

$\vec{S}(t)$: instantaneous velocity vector

t : time

u_τ : friction velocity ($\equiv (\tau_w/\rho)^{0.5}$)

$\tilde{u}(t)$: instantaneous velocity in the x-direction (turbulent flow)

u or u_1 : fluctuation of velocity in the x-direction

U_∞ : free stream velocity

U : mean velocity in the x-direction

v or u_2 : fluctuation of velocity in the y-direction

V : mean velocity in the y-direction

w : cavity width

W : mean velocity in the z-direction, or Cole's wake function

w or u_3 : fluctuation of velocity in the z-direction

x or x_1 : streamwise coordinate measured from the cavity trailing edge

y^+ : yu_τ / ν

y or x_2 : coordinate normal to the wall

z or x_3 : spanwise coordinate

Greek Symbols:

δ : boundary layer thickness

δ^* : displacement thickness

δ_0 : boundary layer thickness near the upstream edge of the cavity

δ_1 : boundary layer thickness at $x/w = 1$

ε : turbulent kinetic energy dissipation rate

η : Kolmogorov length scale ($= (\nu^3/\varepsilon)^{1/4}$)

$\phi_{x,x}(k_1)$: one-dimensional wave number spectrum of u

κ : Karman constant

λ : wave length

λ_{Taylor} : Taylor micro scale

μ : absolute (dynamic) viscosity

ν : kinematic viscosity

π : wake parameter

θ : momentum thickness

ρ : fluid density

τ : time shift (for autocorrelation function) or Kolmogorov time scale ($\equiv (\nu/\varepsilon)^{1/2}$)

τ_{yx} : shear stress at a certain y location

τ_w : wall shear stress

τ^- : Normalized wall shear stress in Bechert equation ($\equiv \tau_w d^2/(\rho \nu^2)$)

ω : radial (angular) frequency ($= 2\pi f$)

Superscripts:

overbar : conventional time average

$+$: denotes normalization by wall variables: u_τ and ν

Subscripts:

1,2 : directions in x_1 and x_2, respectively

Miscellaneous:

$\Im$: integral length scale

Chapter 1

Introduction

The study of fluid mechanics is likely to occupy mankind for a very long time. There is a very broad range of fluid flow problems, from the simple case of inviscid, incompressible, irrotational flow to very complex flows, such as viscous, compressible, three-dimensional flows with heat transfer and chemical reaction. A problem that has been studied for a long time, yet not fully understood, is the skin friction drag due to a turbulent boundary layer. In general, a turbulent boundary layer is very complex and its structure depends on the wall geometry and surface roughness. The simplest case is that of an incompressible, two-dimensional boundary layer over a smooth wall under zero pressure gradient.

Skin friction drag plays a major role in the overall efficiency of aircraft, high-speed vehicles, marine vessels and piping and ducting systems. For example, in transportation applications, overall fuel efficiency can be improved by reducing the total drag force. The required thrust is directly proportional to drag force, and for a typical transport aircraft, skin friction drag can contribute up to 50 % of the total drag at cruising speed (Coustol and Savill, 1991). In internal flows, such as in pipe lines and ducting systems, almost 100% of the drag is due to skin friction. Hence, higher skin friction results in a higher power requirement of the prime mover. Investigations of skin friction drag reduction have been performed intensively over the last five decades, because of the resultant economic benefits.

The nature of the development of the boundary layer plays an important role in skin friction drag. At the leading edge of a surface, the boundary layer is usually laminar.

As the boundary layer develops along the surface, at a certain critical Reynolds number, transition to turbulence occurs. If the boundary layer remains laminar, the total skin friction drag is much less than if the surface is covered by a turbulent boundary layer. Many control schemes have been developed, such as active suction, to maintain a laminar boundary layer over a surface. With laminar flow control, transition of the boundary layer from laminar to turbulent is delayed until a much higher Reynolds number (Haugh, 1972). However, in most practical engineering applications, the boundary layers are turbulent. Most recent research has been devoted to studying skin friction drag reduction in turbulent boundary layers.

1.1 Background of Study

Since Nikuradse (1933) performed his investigation on the effects of wall roughness in pipe flows, many experiments have been performed to determine methods of drag reduction on rough walls. By using passive turbulence control (modification of wall roughness and/or wall geometry), one could potentially reduce skin friction drag, and hence the total drag. Haugen and Dhanak (1966) studied a turbulent boundary layer over a smooth wall with a two dimensional transverse square cavity. They reported that the major component of drag was from the pressure distribution on the cavity walls. Perry et al. (1969) studied turbulent boundary layers over rough walls using *d*-type and *k*-type roughness. The *d*-type roughness is defined as transverse square grooves (cavities) regularly spaced one element width apart in the streamwise direction (Figure 1.1.1(a)). The *k*-type roughness (Figure 1.1.1(b)) is similar to *d*-type roughness, but the roughness element protrudes into the boundary layer. In the *k*-type roughness, the spacing between the roughness elements (*s*) is usually greater than either the element width, *b*, or the element height, *k*. Perry et al. suggested that the turbulent boundary layer over a *d*-type roughness is self-preserving. For self preservation, both the skin friction coefficient (C_f) and $d\delta/dx$ are constant (δ is the boundary layer thickness). Coustols and Savill (1991) reported that a 2-3% net drag reduction can be achieved for a *d*-type roughness if the grooves are spaced 20 element widths apart. A sparse *d*-type roughness, where the distance between two consecutive cavities, *s*, has a range of 10*w* to 40*w*, can reduce the total drag up to 3 %, (Tani, et. al., 1987). Choi and Fujisawa (1993) reported a skin-friction drag reduction of about 1% for a surface with a single cavity, while ignoring the pressure drag on the cavity walls. Matsumoto (1994) concluded that there is a possibility of skin friction drag reduction for sparse *d*-type roughness with *s/w* configurations of 10 and 20. On the other hand, Elavarasan et al. (1996), found an increase in drag up to 3.4 % for $s/w = 20$. Pearson et al. (1995) investigated the shear stress distribution downstream of a single square cavity. They deduced that there was an overshoot in the wall shear stress, τ_w, just down stream of the cavity, followed by an undershoot and an oscillatory relaxation back to the smooth wall value.

Cary et al. (1980) reported a possibility of drag reduction by using small amplitude rigid surface waves. Another passive device used for drag reduction is Large Eddy Break-Up devices (LEBUs). LEBUs act as an outer layer manipulator in a turbulent boundary layer. Such devices consist of thin plates or airfoil cross section elements, and are located in the outer part of the turbulent boundary layer. Hefner et al. (1980) noted an average skin friction drag reduction of about 24% downstream of such a device.

However, the total drag (summation of the skin friction drag and the device drag) was not reduced.

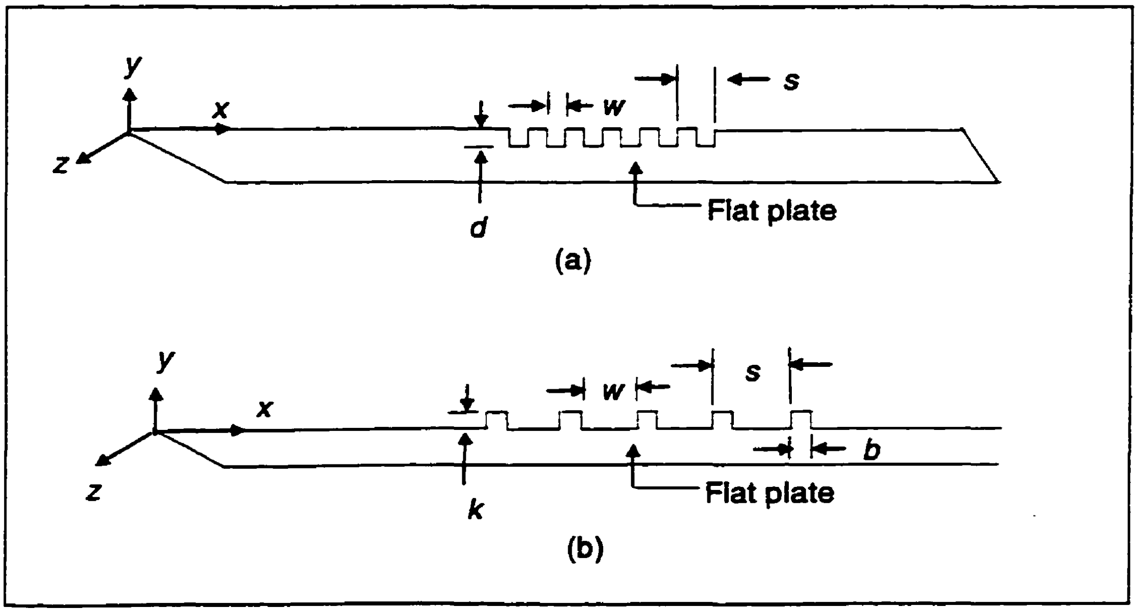

Figure 1.1.1 (a) *d*-type roughness, (b) *k*-type roughness on a flat plate (Reproduced from Perry et al., 1969)

Riblets, or longitudinal V-grooves, when optimally spaced, can reduce the skin friction drag by up to 8 %, (Walsh, 1990), however, the spacing is on the order of a fraction of a millimeter for practical applications, and the machining and maintenance of such surfaces are extremely difficult. The response of the skin friction coefficient in turbulent boundary layers to a sudden change from a rough to smooth wall was studied by Taylor (1993) et al. A sudden drop in C_f below the smooth-wall value immediately after the rough to smooth interface was reported. The skin friction coefficient then gradually increases and approaches the smooth-wall value far downstream of the interface. Another passive drag reducing surface is one having a random pattern of V-shape protrusions (Sirovich and Karlsson, 1997). When the height of the random roughness is optimized, Sirovich and Karlsson reported a drag reduction of 12.5%. However, such a surface is extremely difficult to fabricate, since the width and height of the roughness element is about 200 and 5 wall units, respectively. From an engineering context, the *d*-type roughness is very interesting since the groove size is an order of magnitude larger than that of riblets or the random roughness proposed by Sirovich and Karlsson. Also, this type is the simplest to fabricate and maintain.

1.2 Purpose of Study

The objective of the present study is to determine the effect of a span-wise square groove on the characteristics of a turbulent boundary layer over a flat plate. The effects of the groove on the skin friction and turbulence structure are determined. Experiments were performed in a low-speed wind tunnel at two different Reynolds numbers. Single-normal and X-wire anemometry were used to obtain the velocity profiles and velocity fluctuations in the streamwise and wall-normal directions. In addition, the turbulent wake parameter and power spectra are investigated downstream of the groove. The turbulent kinetic energy dissipation rate and development of the internal layer downstream of the groove are also studied.

1.3 Significance of Study

Despite being studied for many years, there are many aspects of turbulent boundary layers that are still not fully understood. There is still a significant effort devoted to their study, because of the importance of turbulent boundary layers in many practical applications. A study of the effect of a transverse square groove on a turbulent boundary layer should provide some insight into the interaction between the surface and the boundary layer. If the effect of the groove on the boundary layer is understood, then modifications to the surface geometry using sparse *d*-type roughness to achieve a skin friction drag reduction may be possible.

Four methods are employed to estimate the wall shear stress (τ_w) and thus the friction velocity ($u_\tau \equiv (\tau_w/\rho)^{1/2}$, where ρ is the fluid density). The first method is by using a power law approximation for the mean velocity profile in the overlap region. The results from this are in very good agreement with Direct Numerical Simulations (DNS) results (Spalart, 1988), especially at low Reynolds number, where the effects of viscosity are non-negligible. The power law uses an argument that the mean velocity profile in the overlap region has the form $U^+ = C(y^+)^\alpha$, where the constants C and α depend solely on the boundary layer thickness Reynolds number ($R_\delta \equiv U_\infty\delta/\nu$; U_∞ and ν are freestream velocity and fluid kinematic viscosity, respectively, and U^+ and y^+ are defined as U/u_τ and $u_\tau y/\nu$, respectively). The second method is the log-law method (or Clauser chart method). This method assumes that there is a universal mean velocity profile in the overlap region, and is a straight line on a U/u_τ versus log yu_τ/ν plot. This method is usually valid at high Reynolds numbers, where the effect of viscosity can be neglected. Another method to determine the wall shear stress is from the mean velocity gradient in the near-wall region. The velocity gradient is evaluated in the region $y^+ \leq 3$. The last method for determining the wall shear stress is from Preston tube measurements.

1.4 Outline of Thesis

A literature review is presented in chapter 2. The chapter begins with a discussion of the structure of a turbulent boundary layer under a zero pressure gradient, followed by a discussion of velocity and length scales in turbulence. The effect of a span-wise square groove on a turbulent boundary layer is discussed next. This chapter ends with a discussion on the possibility of turbulent boundary layer drag reduction due to a span-wise square groove.

In chapter 3, a description of the experimental facility and instrumentation is presented. Firstly, the wind tunnel is described with details of the tunnel geometry, dimensions, capabilities, and limitations. This is followed by a section on hot-wire anemometry. This section is devoted to the description of the hot-wire probes and anemometer unit. The next part of this chapter describes the Preston tube arrangement and data acquisition system. The last part of chapter 3 describes the method of determining the probe distance from the wall.

Chapter 4 consists of four sections related to data reduction procedures. These sections are for the mean and fluctuating velocity calculations, wall shear stress calculations, and turbulent kinetic energy dissipation rate calculations.

In chapter 5, the experimental results are presented and discussed. The results and discussion include wall shear stress and skin friction coefficient, mean velocity and streamwise turbulence intensity profiles, turbulent wake parameter, power spectra, rate of turbulent kinetic energy dissipation, and internal layers. Some representative results from X-wire measurements are also presented.

Concluding remarks and recommendations are given in chapter 6.

Chapter 2

Literature Review

2.1 Structure of a turbulent boundary layer under zero pressure gradient

Turbulent boundary layers are distinguished from laminar boundary layers by the randomly fluctuating velocity components. For example, the velocity vector ($\vec{S}$) in a laminar boundary layer can be resolved into three orthogonal components, U, V, and W in the streamwise, wall-normal, and spanwise directions, respectively. In turbulent boundary layers, in addition to the mean velocity components, there are fluctuating components denoted by u, v, and w, respectively. Hence, in mathematical forms we have

$$\vec{S} = U\vec{i} + V\vec{j} + W\vec{k} \tag{2.1}$$

for a laminar boundary layer, and

$$\vec{S} = (U + u)\vec{i} + (V + v)\vec{j} + (W + w)\vec{k} \tag{2.2}$$

for a turbulent boundary layer.

2.1.1 Scales in a Turbulent Boundary Layer

Typically, boundary layer flows can be classified into three regimes: laminar, transitional, and turbulent. The velocity fluctuations in turbulent boundary layers play an important role in momentum transfer. In laminar boundary layers, the momentum transfer is essentially by molecular diffusion, whereas in turbulent boundary layers the momentum transfer by the fluctuating velocity plays a significant role. In transitional boundary layers, momentum transfer due to velocity fluctuations can take place, however, the momentum transfer is not as intense as in turbulent boundary layers.

A parameter used to distinguish laminar and turbulent boundary layers is the Reynolds number. This parameter can be interpreted as the ratio of the inertial forces to the viscous forces in the flow. If U and L are the characteristic velocity and length scales, the inertial and viscous terms can be expressed as U^2/L and vU/L^2, respectively. The Reynolds number, R can then be written as

$$R \equiv (U^2/L)/(vU/L^2) = UL/v \qquad (2.3)$$

Turbulent boundary layers are characterized by a large Reynolds number. In such layers, the viscous effects can be neglected, except in the laminar sub-layer region, where the viscosity has a dominant effect. On the other hand, for smaller values of R, the boundary layer will remain laminar, and the viscous effects cannot be neglected throughout the layer. In laminar boundary layers, the inertia term is comparable to the viscous term. If δ is the length scale associated with the viscous term in the laminar boundary layer, one can write

$$U^2/L \sim vU/\delta^2 \qquad (2.4)$$

In terms of the Reynolds number, (δ/L) can be expressed as

$$\delta/L \sim (v/UL)^{1/2} = R^{-0.5} \qquad (2.5)$$

and δ can be interpreted as the boundary layer thickness.

In turbulent boundary layers, in addition to U, there is the characteristic fluctuating velocity (u). For a time interval scale dt, we can assume that

$$dt \sim \delta/u \qquad (2.6)$$

For the same time interval, the associated displacement of the large scale, L, is then

$$dt \sim L/U \tag{2.7}$$

Therefore, the order of magnitude of the ratio of the smaller scale to the larger scale can be written as

$$u/U \sim \delta/L \tag{2.8}$$

Richardson (1922) proposed that a cascade of energy takes place in the turbulent boundary layer. The energy is received from the external flow by the large eddies, and cascades through the eddies in the inertial range to the smallest eddies, where the energy is dissipated into heat by viscosity. The inertial range refers to the range of eddies where no energy is added by the mean flow and no energy is taken out by viscous dissipation (Tennekes and Lumley, 1972).

The turbulent kinetic energy dissipation rate plays an important role in turbulent flow analysis. In isotropic turbulence, the dissipation rate, ε, is given by

$$\varepsilon = 15\nu\overline{(\partial u/\partial x)^2} \tag{2.9}$$

Values of $\overline{(\partial u/\partial x)^2}$ can be obtained experimentally using Taylor's frozen hypothesis. The hypothesis states that if the turbulent velocity fluctuations are small compared to the mean velocity, then the autocorrelation of the fluctuating velocity with time delay τ will be the same as the spatial correlation with separation $U\tau$ in the streamwise direction (Bradshaw, 1971). In mathematical form, Taylor's hypothesis can be expressed as

$$\frac{\partial u}{\partial x} = \frac{1}{U(y)}\frac{\partial u}{\partial t} \tag{2.10}$$

$\partial u/\partial t$ can usually be obtained from instantaneous velocity measurements.

The dissipation of the turbulent kinetic energy takes place in the smallest eddy range. The mean energy dissipation, ε, per unit mass per unit time can be thought of as direct dissipation of turbulent kinetic energy into thermal internal energy. The most important parameter that governs this phenomenon is the kinematic viscosity ν. The dissipation (ε) and ν can be used to obtain the smallest scales of length (η), time (τ), frequency (f_K), and velocity (υ), in the flow, and are referred to as the Kolmogorov scales (Tennekes and Lumley, 1972)

$$\eta = (\nu^3/\varepsilon)^{1/4} \tag{2.11}$$

$$\tau = (\nu/\varepsilon)^{1/2} \tag{2.12}$$

$$f_K = U/(2\pi\eta) \tag{2.13}$$

$$\upsilon = \eta/\tau = (\nu\varepsilon)^{1/4} \tag{2.14}$$

It can be assumed that the rate of energy transfer in the large-scale range is proportional to u/δ (Tennekes and Lumley, 1972). In an equilibrium turbulent boundary layer, the rate of energy dissipation is proportional to the rate of energy transfer to the large scale eddies. Hence, (after Taylor, 1935)

$$\varepsilon \sim u^3/\delta \tag{2.15}$$

With Eq. (2.15) we can formulate the following scale relations

$$\eta/\delta \approx (\nu^3/\varepsilon)^{1/4}/\delta = (\nu^3\delta/u^3)^{1/4}/\delta = (\nu/(u\delta))^{3/4}$$

or

$$\eta/\delta \approx R^{-3/4} \tag{2.16}$$

The time scale relation is then,

$$\tau/(\delta/u) \approx (u/\delta)(\nu/\varepsilon)^{1/2} = (u/\delta)(\nu/(u^3/\delta))^{1/2} = (\nu/(u\delta))^{1/2}$$

or

$$\tau / (\delta / u) \approx R^{-1/2} \tag{2.17}$$

and the velocity scale relation is

$$\upsilon / u \approx (\nu\varepsilon)^{1/4} / u = (\nu u^3 / \delta)^{1/4} / u = (\nu / (u\delta))^{1/4}$$

or

$$\upsilon/u \approx R^{-1/4} \tag{2.18}$$

As the Reynolds number increases, the Kolmogorov length, time, and velocity scales become much smaller than the corresponding large scales.

In addition to the Kolmogorov length scale, the Taylor microscale (λ_{Taylor}) and integral length scale ($\Im$) are often used in the analysis of turbulent flows. The Taylor microscale, with dimension of length, is defined as (after Tennekes and Lumley, 1972)

$$\lambda_{Taylor} \equiv \left[\frac{\overline{u^2}}{\overline{(\partial u / \partial x)^2}} \right]^{1/2} \tag{2.19}$$

By recalling Taylor's frozen hypothesis, based on Eq. **(2.10)**, we can obtain

$$\rho(\tau) = \rho(\ell) \tag{2.20}$$

where $\rho(\ell)$ is the spatial correlation with separation ℓ ($\ell = U\tau$). Figure 2.1.1 shows a typical spatial correlation curve.

The area under the spatial correlation curve is the integral length scale, $\bar{\Im}$, so that

$$\Im \equiv \int_0^{\infty} \rho(\ell)\, d\ell \tag{2.21}$$

The Taylor microscale and the integral length scale are far larger than the Kolmogorov length scale.

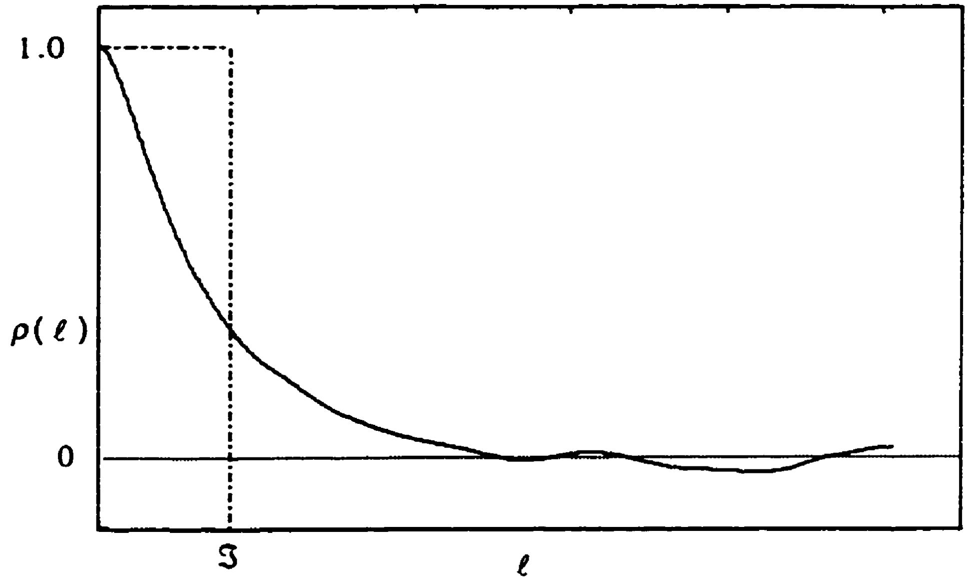

Figure 2.1.1 A typical spatial correlation curve

2.1.2 Mean Velocity Profiles

The mean velocity profiles of turbulent boundary layers, when normalized by outer variables, U_∞ and δ, are affected by Reynolds number, while the normalized mean velocity profiles of laminar boundary layers are independent of Reynolds number. A comparison between normalized laminar and turbulent mean velocity profiles are shown in Figure 2.1.2. The turbulent boundary layer profiles become flatter as the Reynolds number increases.

In turbulent boundary layers, the total shear stress is made up of two components: the viscous shear stress $\left(\mu \frac{dU}{dy}\right)$, and the Reynolds shear stress $(-\rho\overline{uv})$. The viscosity effect dominates in the innermost part of the turbulent boundary layer, from $y/\delta = 0$ to $y/\delta \sim 0.02$. In the region very close to the wall, say $0 \leq y/\delta \leq 0.003$, only the viscous shear stresses are present. This region is usually referred to as the laminar sublayer. The laminar sublayer thickness is very thin, and it may be even smaller than the surface roughness.

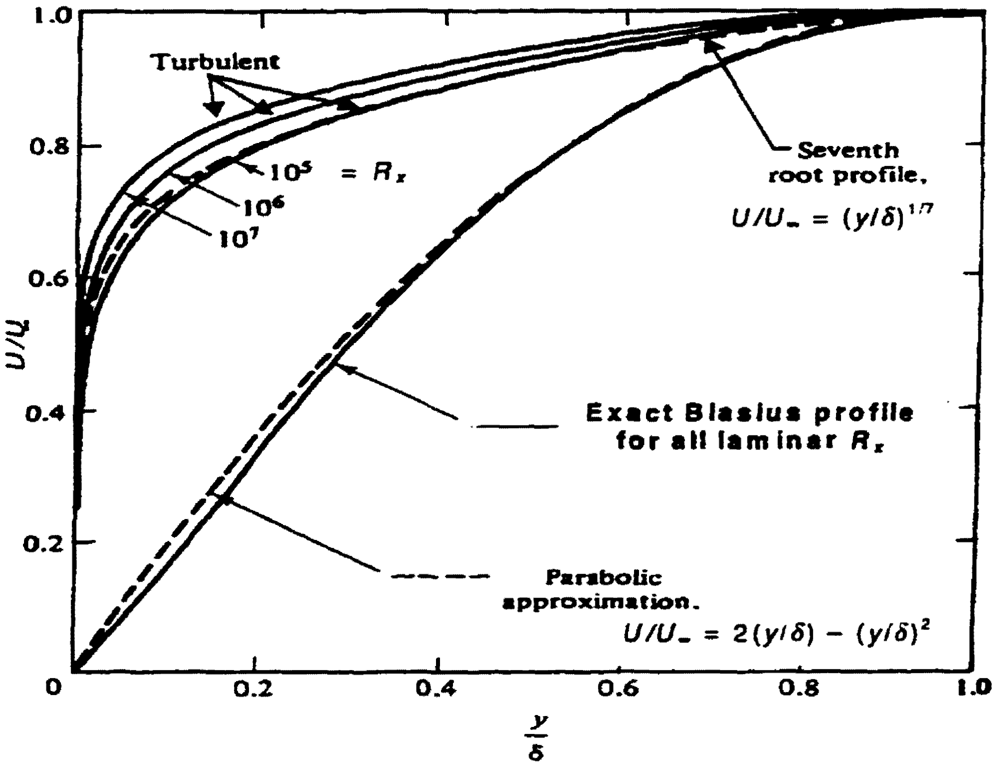

Figure 2.1.2 Comparison of non-dimensional profiles for flat plate laminar and turbulent boundary layers (Reproduced from White, 1986)

As the surface roughness becomes comparable to the laminar sublayer thickness, the velocity profiles are affected by the surface roughness. On the other hand, laminar boundary layer profiles are not affected by the surface roughness. The dependence of turbulent velocity profiles on the surface roughness is shown in Figure 2.1.3. From the figure, it can be seen that the mean velocity profiles in a turbulent boundary layer are affected by Reynolds number and/or surface roughness. For the two cases shown in the figure, the roughness results in a downward shift of the velocity profile, indicating a higher wall shear stress.

Turbulent boundary layer velocity profiles are often approximated with a 1/7th power-law when plotted as (U/U_∞) versus (y/δ) (Figure 2.1.2). From this figure, it is obvious that a single power law approximation is not valid for the entire range of Reynolds number. In fact, experimental data show a wide range of exponents if power-laws are used to approximate the velocity profiles. The numerical values of the exponent depend on Reynolds numbers and vary from 1/3 to 1/10 (Clauser, 1956).

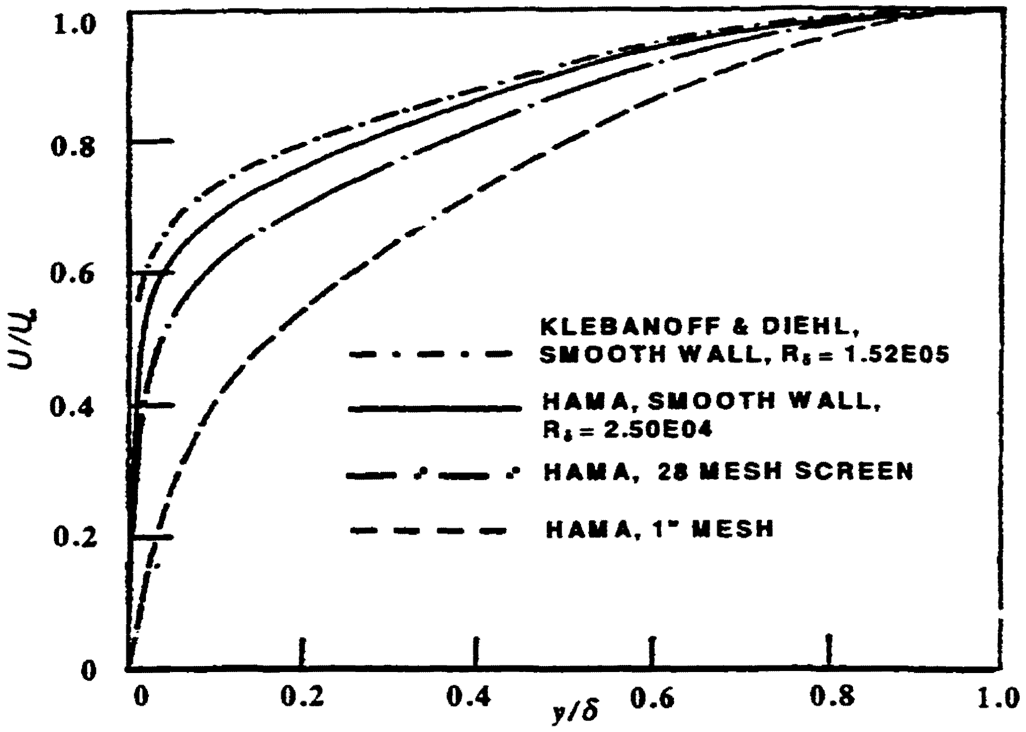

Figure 2.1.3 Turbulent boundary layer profiles at constant pressure on smooth and rough walls (Reproduced from Clauser, 1956)

Clauser (1956) used the friction velocity, u_τ, to nondimensionalize a family of turbulent boundary layer profiles. When (U_∞ - U)/u_τ was used as the ordinate, the profiles which originally depended on Reynolds number and surface roughness, collapsed to a single profile (Figure 2.1.4). In mathematical form, this can be expressed as:

$$\frac{U_\infty - U}{u_\tau} = g\left(\frac{y}{\delta}\right) \qquad (2.22)$$

and is called the velocity-defect law. For a turbulent boundary layer under zero pressure gradient, the velocity defect $(U_\infty - U)/u_\tau$ is solely a function of y/δ.

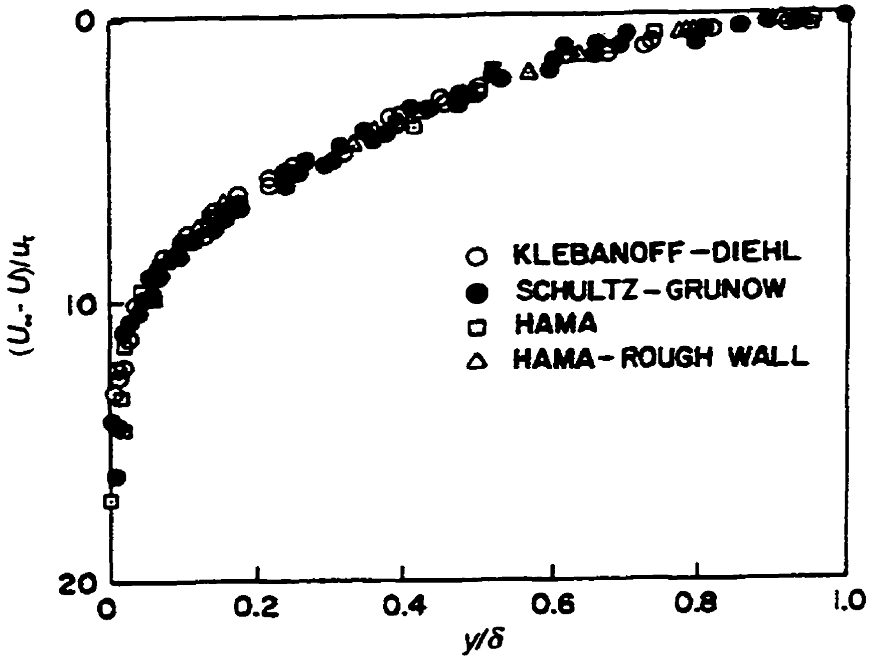

Figure 2.1.4 Universal plot of turbulent boundary layer profiles at zero pressure gradient. (Reproduced from Clauser, 1956)

There are two main regions in a turbulent boundary layer: the inner region and the outer region. The inner region occupies approximately 20% of the boundary layer thickness (δ) and consists of three sub-regions: the laminar sub-layer, buffer zone, and an overlap region. In the laminar sub-layer the viscous shear dominates, while in the overlap region both viscous and turbulent shear stresses are non-negligible. The outer region is much larger than the inner region, and occupies about 80% of the boundary layer thickness. Unlike in the inner region, only the turbulent shear is important in the outer region. A typical plot of the mean velocity distribution in a turbulent boundary layer under zero pressure gradient when normalized by inner variables (u_τ and ν) is shown in Figure 2.1.5.

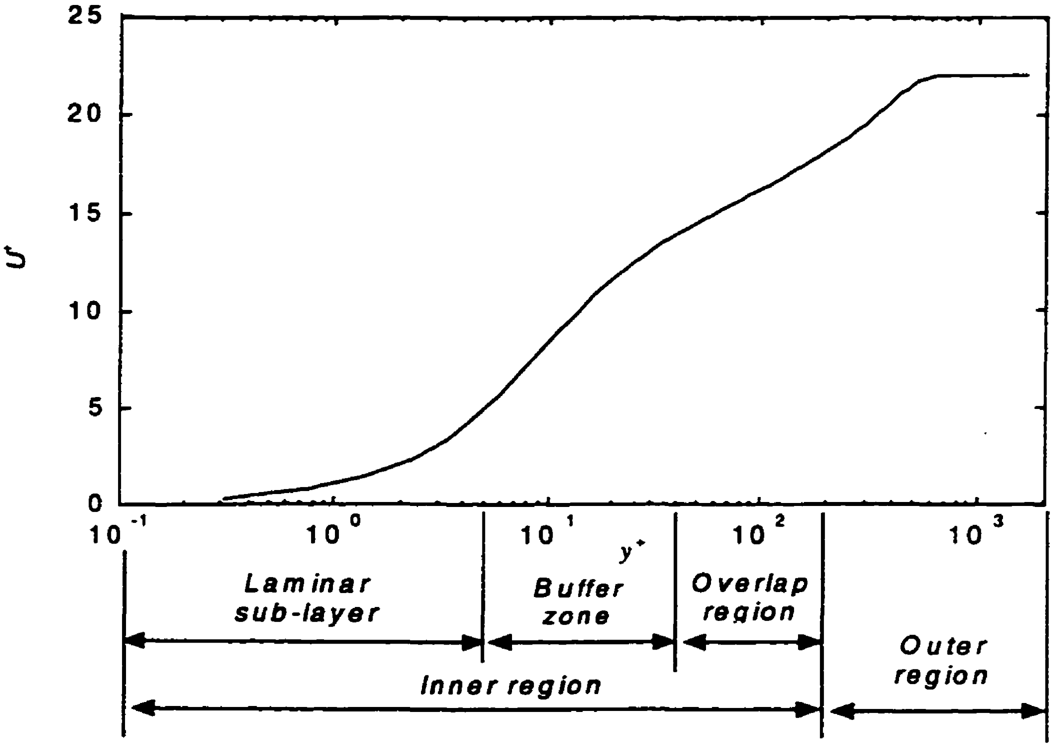

Figure 2.1.5 A typical plot of mean velocity distribution in a turbulent boundary layer under zero pressure gradient.

In the laminar sub-layer, ν / u_τ is the appropriate length scale, and the velocity can be expressed as:

$$\frac{U}{u_\tau} = h\left(\frac{yu_\tau}{\nu}\right) \tag{2.23}$$

In this layer,

$$\tau = \mu \frac{dU}{dy} \tag{2.24}$$

which can be integrated to yield

$$U^+ = y^+ \tag{2.25}$$

Eq. (2.25) is generally valid in the region $0 \le u_\tau y / \nu \le 3.0$, though it is commonly used in the range $0 \le u_\tau y/\nu \le 5.0$.

As the distance from the wall increases, the effect of viscosity decreases. In the transitional region, the viscous and Reynolds (turbulent) stresses are comparable. This transitional region is usually called the buffer region. In this region, von Karman suggested a logarithmic equation for the velocity profile:

$$\frac{U}{u_\tau} = 5.0 \ln\left(\frac{u_\tau y}{\nu}\right) - 3.05 \tag{2.26}$$

valid for $5.0 \le u_\tau y/\nu \le 70$ (Yuan, 1988).

The outermost part of the inner region is called the overlap region. In this region, both Eq. (2.22) and Eq. (2.23) must be satisfied. Combining Eq. (2.22) and Eq. (2.23), one can obtain

$$\frac{U}{u_\tau} = \frac{1}{\kappa} \ln\left(\frac{u_\tau y}{\nu}\right) + B \tag{2.27}$$

for the inner region, and

$$\frac{U - U_\infty}{u_\tau} = \frac{1}{\kappa} \ln\left(\frac{y}{\delta}\right) + E \tag{2.28}$$

for the outer region, respectively. For turbulent boundary layers over a smooth flat plate, κ, B, and E will have constant values. The constants κ and B are referred to as the Karman constant and the smooth wall constant, respectively, and are assummed independent of the Reynolds number. Eq. (2.27) is generally called the log-law, and describes the mean velocity profiles well in the overlap region, especially at high Reynolds number. In the region very close to the wall ($y^+ \le 30$), the log-law is not valid. As the Reynolds number increases, the log-law approximation is valid in a wider range of

y^+ (Figure 2.1.6). However, the log-law deviates from the data in the outer part of the boundary layer. The deviation of the velocity profile from the log-law in the outer region is described by the '*wake function*'. A brief discussion on the wake function in turbulent boundary layers over a smooth wall under zero pressure gradient is given in section 2.1.3.

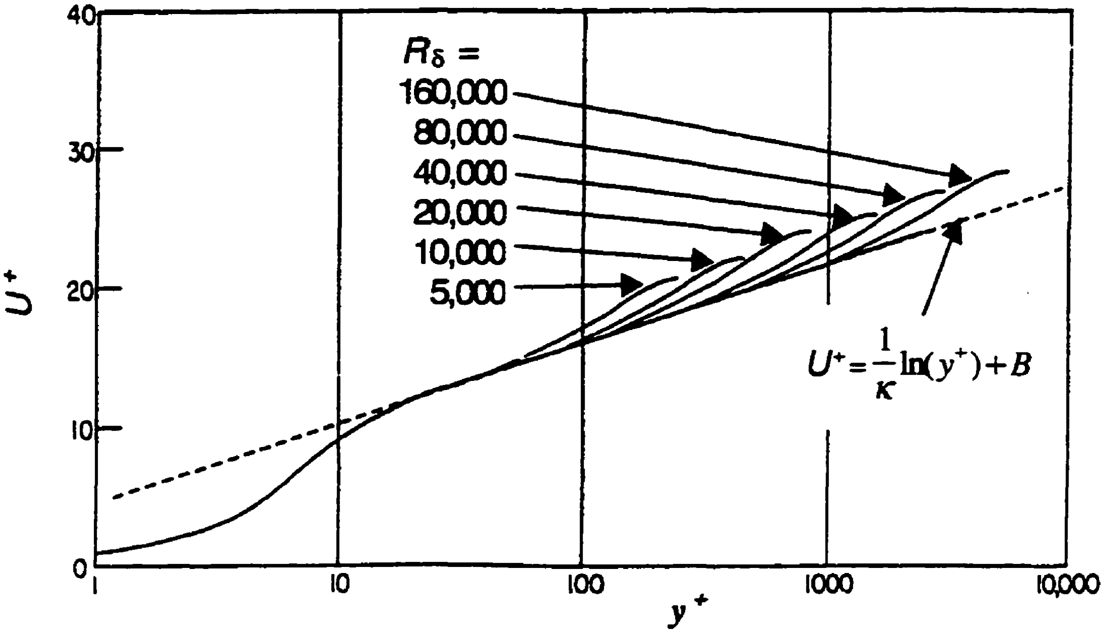

Figure 2.1.6 Dependence of validity of log-law approximation on the Reynolds numbers (Reproduced from Clauser, 1956)

In 1937, Millikan proposed a universal logarithmic equation for the overlap region:

$$\frac{U}{u_\tau} = \frac{1}{\kappa}\ln\left(\frac{u_\tau y}{\nu}\right) + 5.0 \qquad \textbf{(2.29)}$$

where $\kappa \approx 0.41$ (White, 1986).

Barenblatt and Prostokishin (1993), however, proposed an alternate power-law of the form

$$U^+ = C\,(y^+)^\alpha + D \qquad \textbf{(2.30)}$$

for the overlap region at low Reynolds numbers. Ching et al. (1995a) plotted mean velocity data as $(U^+)^{1/\alpha}$ versus y^+ (Figure 2.1.7), and determined that the power-law described the overlap region well for $R_\theta \leq 1300$. In this case, α and C are dependent on the boundary layer thickness Reynolds number, R_δ. Following Barenblatt (1993), α is given by

$$\alpha = \frac{3}{2\ln R_\delta} \tag{2.31}$$

and C is expressed as

$$C = \frac{1}{\sqrt{3}}\ln R_\delta + \frac{5}{2} \tag{2.32}$$

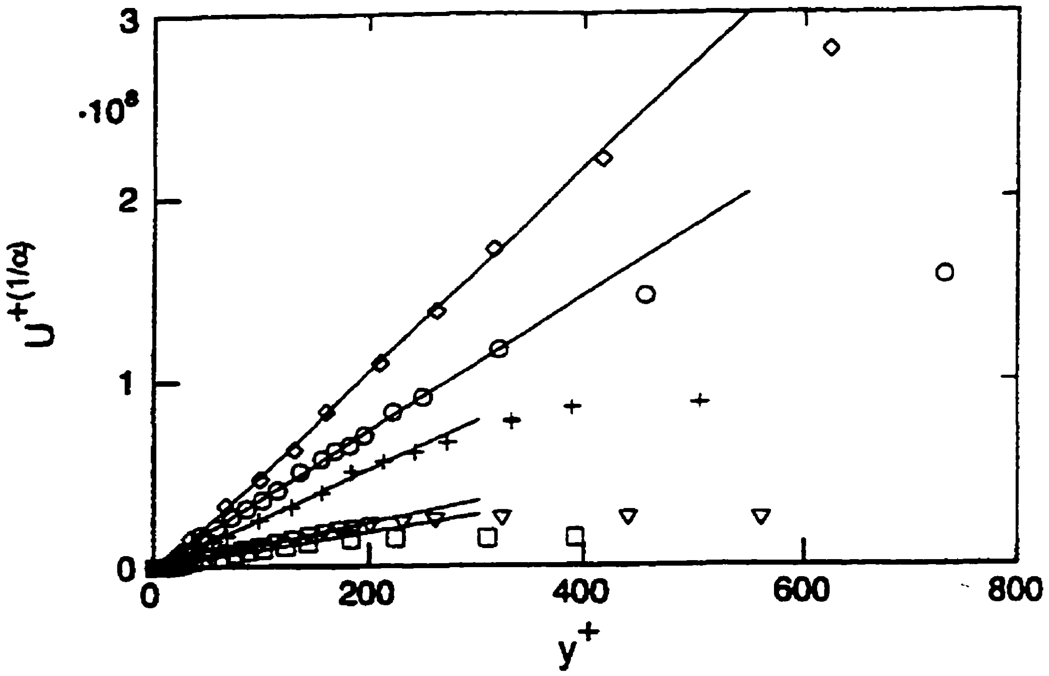

Figure 2.1.7. Mean velocity plotted in the form of a power law. ◇, R_θ = 1316; ○, 979; +, 765; ▽, 509; □, 400; ——, least squares straight line fit. (Reproduced from Ching et al., 1995)

As the Reynolds number decreases, the effect of viscosity is more significant. At low Reynolds numbers ($R_\theta \leq 1500$, say), there is no formal basis for the log-law to exist, and it can be argued that the power-law is more appropriate. A comparison of mean velocity data U^+ (Djenidi et al. 1997) with DNS data (Spalart, 1988) and the power-law distribution is given in Figure 2.1.8. It can be seen from this figure that the power-law closely describes the velocity profile, except in the region very close to the wall ($y^+ \leq 30$).

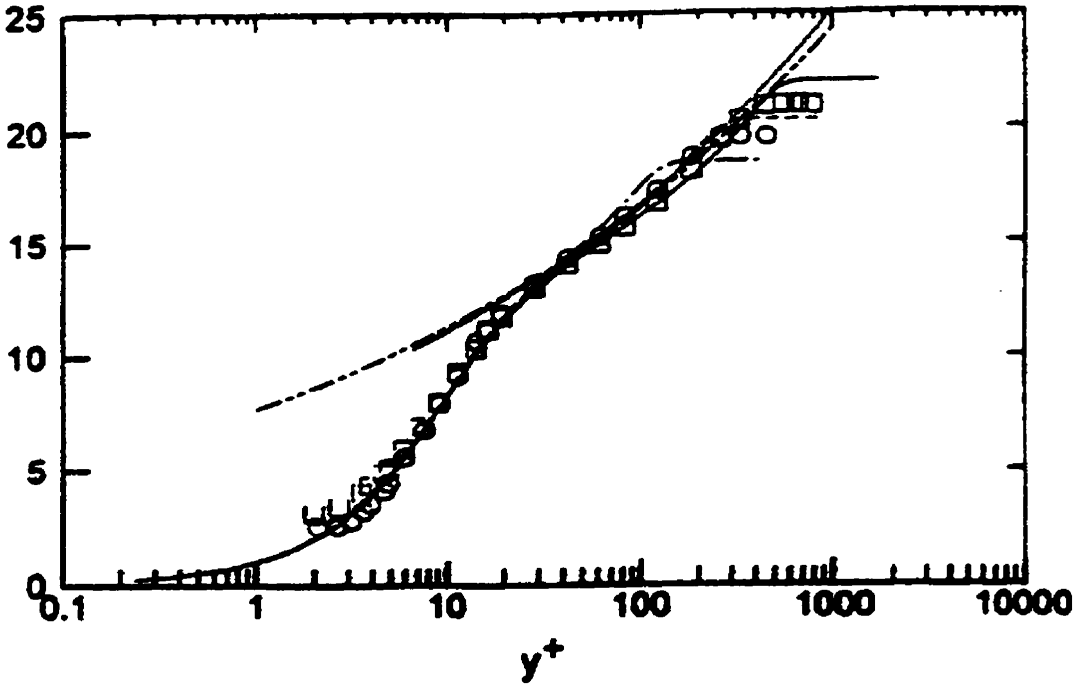

Figure 2.1.8 Comparison of experimental data, power-law fits, and DNS data. Experiment: ○, R_θ = 540; □, R_θ = 940; Power-law fit: — – – –—, R_θ = 940; – – –, R_θ = 540; DNS:— – —, R_θ = 300; ----, R_θ = 670; ——, R_θ = 1410 (Reproduced from Djenidi et al. 1997)

2.1.3 Wake Parameter, π

The wake parameter, π, was introduced by Coles (1956) to characterize the outer region of the mean velocity profile in a turbulent boundary layer. In the outer layer, the mean velocity profile deviates from the logarithmic law (Figure 2.1.6). This is called the "*wake*" region. Coles (1956) defined a '*wake*' function $W(y/\delta)$ such that $W(0) = 0$ and $W(1) = 2$, which leads to

$$W\left(\frac{y}{\delta}\right) \equiv 2\left[\frac{U^{+} - \left(\frac{1}{\kappa}\ln(y^{+}) + B\right)}{U_{\infty}^{+} - \left(\frac{1}{\kappa}\ln(\delta^{+}) + B\right)}\right] \qquad \textbf{(2.33)}$$

where $U^+ = U/u_\tau$, $y^+ = u_\tau y/\nu$, $U_\infty^+ = U_\infty / u_\tau$, and $\delta^+ = u_\tau \delta/\nu$. By adding the wake function to the logarithmic law, one obtains

$$U^{+} = \frac{1}{\kappa}\ln(y^{+}) + B + \frac{\pi}{\kappa}W\left(\frac{y}{\delta}\right) \qquad \textbf{(2.34)}$$

This is valid for both the overlap and the outer regions. The wake parameter(π) can then be expressed explicitly as

$$\pi = \frac{\kappa}{W(y/\delta)}\left(U^{+} - \frac{1}{\kappa}\ln(y^{+}) - B\right) \qquad \textbf{(2.35)}$$

At $y = \delta$,

$$\pi = \frac{\kappa}{2}\left(\frac{U_\infty}{u_\tau} - \frac{1}{\kappa}\ln(\frac{u_\tau \delta}{\nu}) - B\right) \qquad \textbf{(2.36)}$$

Eq. **(2.28)** can be expressed as

$$\frac{U_\infty}{u_\tau} = \frac{U}{u_\tau} - \frac{1}{\kappa}\ln(y/\delta) - E \qquad \textbf{(2.28a)}$$

Combining Eq. **(2.34)** and Eq. **(2.28a)** leads to

$$\pi = \frac{\kappa}{2}\left[\left\{\ \frac{U}{u_\tau} - \frac{1}{\kappa}\ln(y/\delta) - E\ \right\} - \frac{1}{\kappa}\ln(u_\tau \delta/\nu) - B\right]$$

or

$$\pi = \frac{\kappa}{2}\left[\frac{U}{u_\tau} - \frac{1}{\kappa}\ln y^{+} - B - E\right]$$

The first three terms in the bracket are zero, and hence

$$\pi = -\frac{\kappa E}{2} \tag{2.37}$$

The wake parameter (π) can be computed with either Eq. (2.36) or Eq. (2.37). If we use $\kappa = 0.41$ and $E = -2.5$ as suggested by Clauser (1956), then $\pi = 0.51$. The value of π proposed by Coles is 0.55. In an equilibrium boundary layer, π is constant (Clauser, 1954), and for a zero pressure gradient boundary layer has a value of 0.55, provided $R_\theta \geq 5000$ (Cebeci and Smith, 1974).

2.2 Surface Drag Reduction in a Turbulent Boundary Layer over a Smooth-Wall with Spanwise Square Grooves

The interaction between a transverse square groove and a turbulent boundary layer has been studied for some time. Roshko (1955) determined that if the pressure drag inside the cavity is much larger than the friction force on the free side of the vortex inside the cavity, momentum transport into and out of the cavity is very likely. He employed a rectangular cavity with depth to width ratio (d/w) ranging up to 2.5. The Reynolds number was $R_\delta = 3.75 \times 10^4$, and δ at a location $0.375w$ from the leading edge of the cavity is about $0.25w$, indicating that the cavity is much larger than the boundary layer thickness. His experimental results showed that the contribution of the prèssure drag to the total drag is very significant, while the friction drag on the main surface and the cavity wall is relatively small. The deflection of the boundary layer separation into the cavity was believed responsible for the formation of the high-pressure coefficient on the down stream edge of the cavity wall.

Haugen and Dhanak (1966) showed that a rectangular cavity had a significant effect on the drag and velocity profile in the cavity. The drag was mainly due to the difference between the integrated mean values of pressure coefficients on the upstream and downstream cavity walls. The mean velocity in the near-wall region is affected by the presence of the circulatory motion of fluid inside the cavity. This motion reduces the mean velocity gradient at $y = 0$ (plane flush with the main surface), and thus reduces local wall shear stress. They found a single stable vortex inside the cavity if the ratio d/w equals unity. When d/w is increased, the number of vortices inside the cavity is approximately of the order of the d/w ratio.

Elavarasan et al. (1996) observed the growth of an internal layer (δ_i) as a response of the boundary layer to the cavity. The mean velocity profile of the internal layer is linear when plotted as $U(y) = f(y^{1/2})$. The internal layer phenomenon was also observed by Antonia and Luxton (1971 and 1972), and Andreopoulus and Wood (1982). Antonia and Luxton (1971) studied the internal layer using the '*knee*' method and the '*merge*' method. They compared the internal layer growth from the '*merge*' method to those obtained theoretically by Elliot (1958) and Townsend (1965). The comparison was in good agreement, although the experimental values were smaller than the predicted values. Antonia and Luxton (1971) suggested that the internal layer turbulent structure is significantly affected by the roughness configuration. Andreopoulus and Wood noted that the internal layer merged with the boundary layer edge at about $x/\delta_0 = 13$, where δ_0 is the boundary layer thickness just upstream of the roughness. A sudden change in surface roughness, either smooth to rough or vice versa, is likely to produce an the internal layer.

Choi and Fujisawa (1993) reported a net drag reduction of about 1% for a turbulent boundary layer over a single transverse square cavity on a flat plate. The pressure drag coefficient, C_d, in the cavity was about 0.001, and was much smaller than that reported by Roshko (1955), Tani et al.,(1961), and Haugen and Dhanak (1966). In the latter studies, C_d was in the range 0.01 to 0.02. Choi and Fujisawa found that there was a small sudden decrease in C_f, just downstream of the cavity. This is reflected in an upwards shift of the mean velocity in the buffer and the wake regions immediately downstream of the cavity. The relaxation of C_f back to the smooth wall value occurs at about $100d$ downstream from the cavity trailing edge. The turbulence intensity above the cavity was found to be higher than that for a corresponding smooth wall. Choi and Fujisawa found that the wake parameter, π, was higher than those on a smooth wall for $x/d \leq 100$. On the other hand, π was lower than those on a smooth wall for $x/d > 100$.

Pearson et al. (1997) conducted a similar study to determine the response of a turbulent boundary layer downstream of a single square cavity. They investigated the interaction between the cavity groove and the boundary layer, and the relaxation of the turbulent boundary layer down stream of the cavity. They found a sharp rise in $C_f/C_{f,0}$ just downstream of the cavity, followed by an undershoot, and an oscillatory relaxation back to unity (Figure 2.2.1, C_f and $C_{f,0}$ are the local skin friction coefficients on the wall with a single cavity and on the smooth wall, respectively). Through flow visualization, they determined that there were out flows (ejections) from and inflows to the cavity. The flow visualization results were qualitatively similar to those of Ching et al. (1995b) and Elavarasan et al. (1996). Figures 2.2.2 and 2.2.3 show time sequences of an ejection and inflow from and to the cavity to the overlying layer, respectively.

Perry et al. (1969) showed that a turbulent boundary layer over a *d*-type roughness is self-preserving. Also, it was noted that a shift in the origin below the roughness crest was necessary to obtain the usual logarithmic velocity distribution. The shifting variable, *e*, is independent of *k* (the roughness element height, see Figure 1.1.1(b)), but is dependent on the boundary layer thickness, δ.

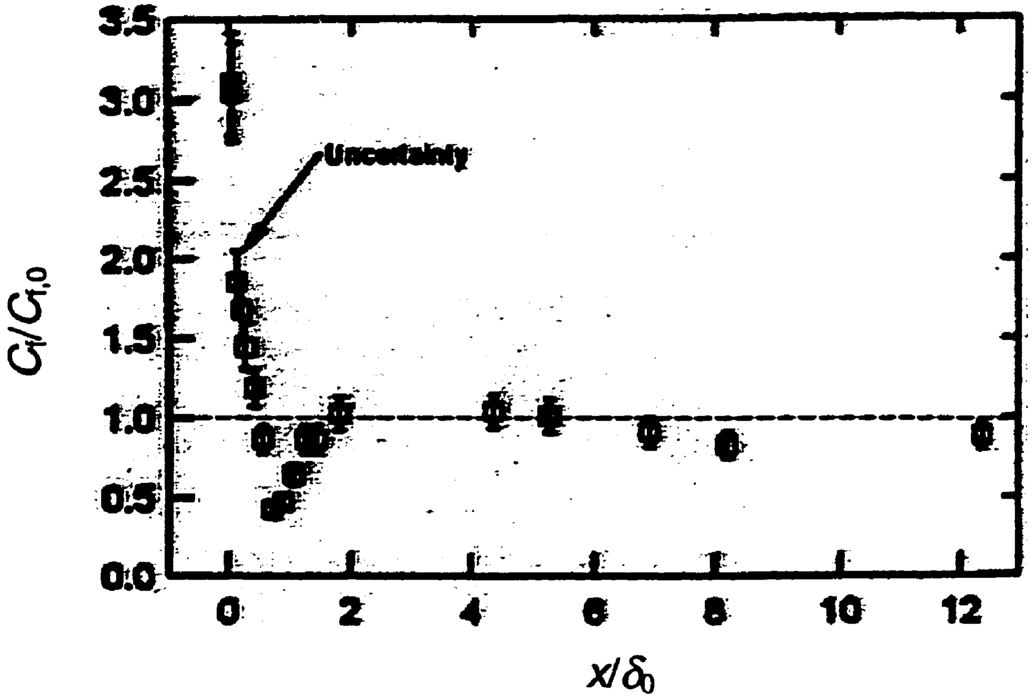

Figure 2.2.1 Skin friction development in the streamwise direction for a turbulent boundary layer, $R_\theta = 1320$ (Reproduced from Pearson et al, 1995)

While there have been many studies of turbulent boundary layers over a *d*-type rough wall (Perry et al., 1969; Wood & Antonia, 1975; Tani et al., 1987; Osaka and Mochizuki, 1988; Choi et al., 1989; Choi and Fujisawa 1993; Djenidi et al., 1994; Ching et al., 1995), there have been very few studies of sparse *d*-type roughness. Moreover, the level of interaction between the cavity flow and the overlying shear layer is not clearly understood. The existence of the cavity flows is believed to be responsible for the increase in momentum exchange between the cavity and the overlying shear layer. Using flow visualization, Djenidi et al. (1994) found that for a *d*-type rough wall, there are ejections from the cavity into the overlying shear layer. They speculated that the near-wall quasi streamwise vortices are responsible for these ejections, and also responsible for the increase in $\overline{uv}$. The relaxation process between two consecutive cavities is not clearly understood.

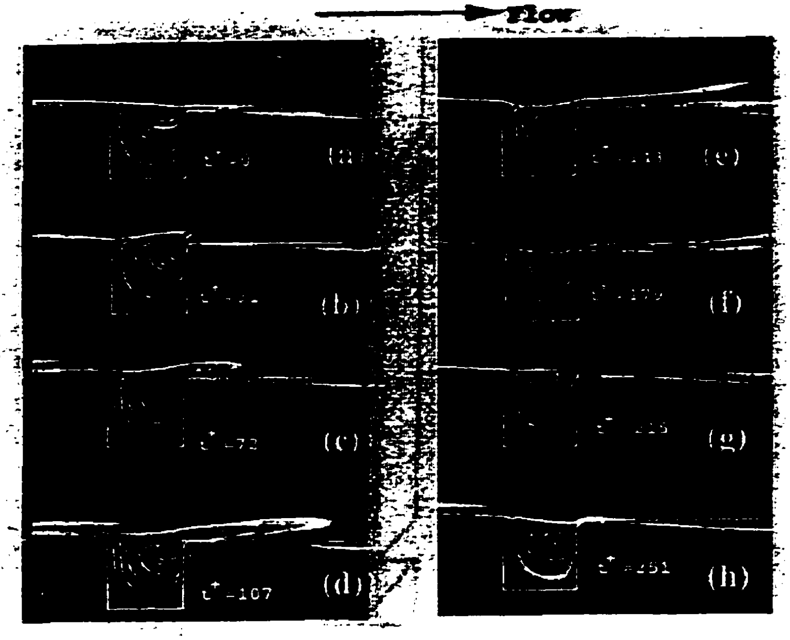

Figure 2.2.2 A time sequence of ejection (Reproduced from Ching et al. 1995)

Coustols and Savill (1991) observed that a sparse *d*-type roughness can produce net drag reduction of about 2-3%, at least at low Reynolds number ($R_x \sim 0.8 - 2.6 \times 10^6$, $R_d \equiv U_\infty d/\nu \approx O$ (5000)). The optimum spacing of the cavities has been conjectured to be close to $s/w = 20$. The existence of a single stable vortex in each cavity, and the beneficial modification of the near-wall turbulent structure between consecutive cavities are believed to be responsible for the surface drag reduction. The stable vortices inside the cavities act as 'stress relieving' that virtually reduce τ_w (Coustols and Savill, 1991). This result agrees with that obtained by Matsumoto (1994). Matsumoto investigated turbulent boundary layers over transverse square grooves with different values of s/w. He found that an increase in the wake parameter was related to a decrease in wall shear stress. In order to obtain a skin friction drag reduction, the spacing s/w was found to be a function of R_θ. For example, for $s/w = 10$, a drag reduction was obtained for $R_\theta < 3700$, whereas for $s/w = 30$ or 40, no drag reduction was obtained over the entire range of R_θ. When $s/w = 20$, a reduction in C_f was determined for $R_\theta < 5200$.

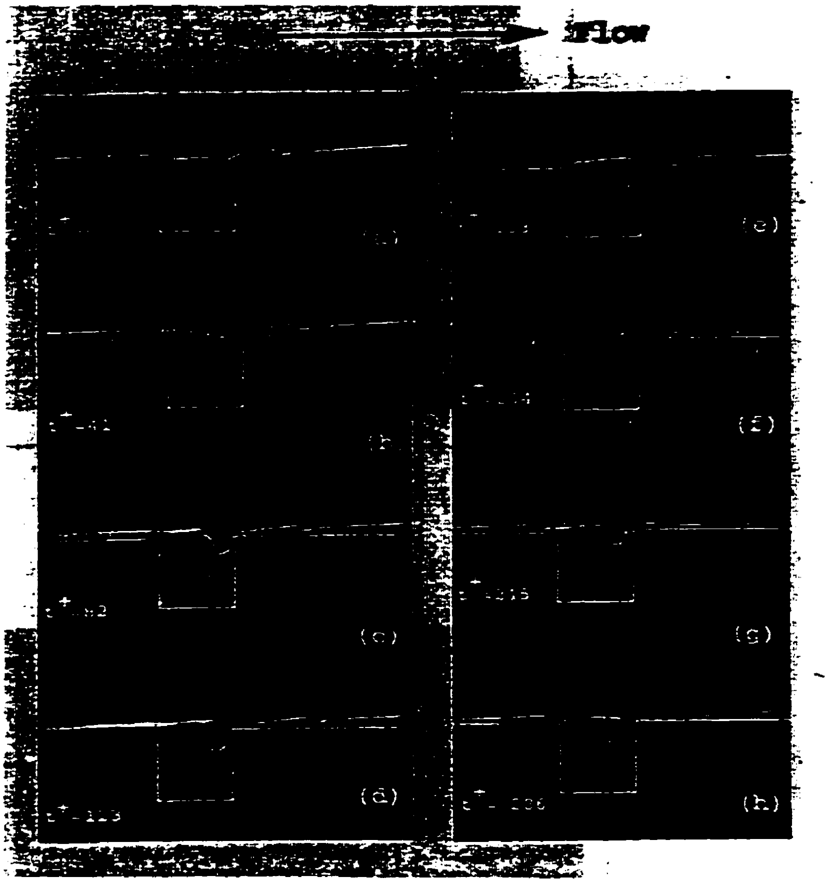

Figure 2.2.3 A time sequence of inflows (Reproduced from Ching et al. 1995)

While Choi and Fujisawa (1993), and Matsumoto (1994) found a reduction in drag for a sparse *d*-type roughness, Elavarasan et al., (1996) found an increase in friction drag of about 3.4% for a spacing $s/w = 20$. Although there was an increase in total friction drag, a local decrease in $C_f/C_{f,0}$ was observed immediately downstream of the cavity ($0.17 \lesssim x/\delta_0 \lesssim 0.5$, for $R_\theta = 1300$). This is similar to the observations of Pearson et al. The investigations of Elavarasan et al. (1996) and Pearson et al. (1995) showed an overshoot in $C_f/C_{f,0}$ just downstream of the cavity followed by an undershoot in $C_f/C_{f,0}$. The undershoot in $C_f/C_{f,0}$ in the latter two studies provided new insight for optimization of a sparse *d*-type roughness to obtain a reduction in surface drag.

From an engineering context, the sparse *d*-type surface is very attractive, since such a surface is easier to fabricate and maintain than riblets. In addition, such a surface can be combined with other potential drag reduction devices such as LEBUs (Bandyopadhyay, 1986), or longitudinal ribs within the cavities (Osaka and Mochizuki, 1991) to obtain larger drag reductions. The sparse *d*-type surface, when s/w is properly optimized, may result in larger drag reductions than those obtained by Coustols and Savill (1991) and Matsumoto (1994). Based on the results of Pearson et al., Ching and Parsons (1998) explained how the surface drag reduction can be enhanced by using a sparse *d*-type surface. By assuming the wall shear stress distribution between consecutive cavities is qualitatively similar to that of Pearson et al., Ching and Parsons proposed a distribution of τ_w on the sparse *d*-type surface as shown in Figure 2.2.4. They suggested that the total surface drag is a function of Reynolds number, s/w, and cavity size. If the area under the overshoot can be reduced, while the area under the undershoot is increased, the total surface drag could be decreased. The sharp increase in τ_w just downstream of the cavity could be reduced by cavity size and/or cavity shape optimization. The overshoot in τ_w could be eliminated if the next cavity is located just at the end of the undershoot.

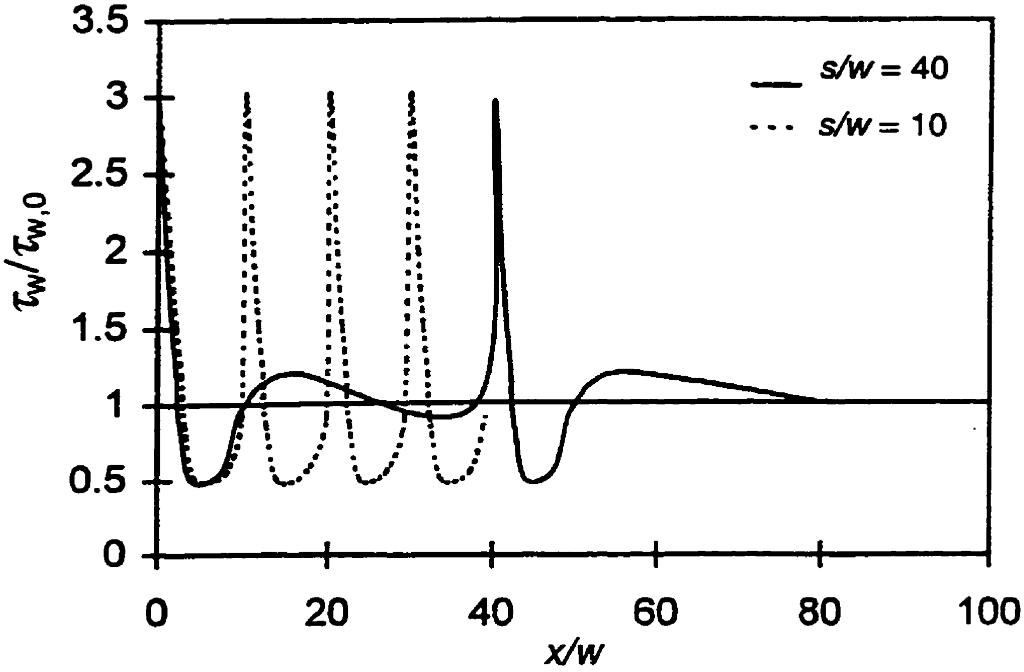

Figure 2.2.4 Schematic diagram of wall shear stress distribution for *s/w* = 40 and 10. (Reproduced from Ching and Parsons, 1998)

The current study is focused on the effect of a single transverse square groove (cavity) on a turbulent boundary layer. At present, the interaction between a cavity and the turbulent boundary layer is poorly understood, and the study should provide some information about the interaction between the surface and the boundary layer. If the effect of the cavity on the boundary layer is clearly understood, then modification to the surface geometry using sparse *d*-type roughness to reduce the skin friction drag may be possible. The experiments are performed at R_θ in the range 900–4030. At these R_θ, the spatial resolution of the hot-wire and Preston tube are adequate to obtain accurate results.

Chapter 3

Experimental Facility and Instrumentation

3.1 Wind Tunnel Configuration

The experiments were performed in an open circuit low speed wind tunnel at Memorial University of Newfoundland. The wind tunnel has a 1m x 1m test section and is over 20m long (Figure 3.1.1). The roof of the tunnel is adjusted to maintain a zero pressure gradient along the test section. Only the initial 5.5m length of the test section was used for this investigation.

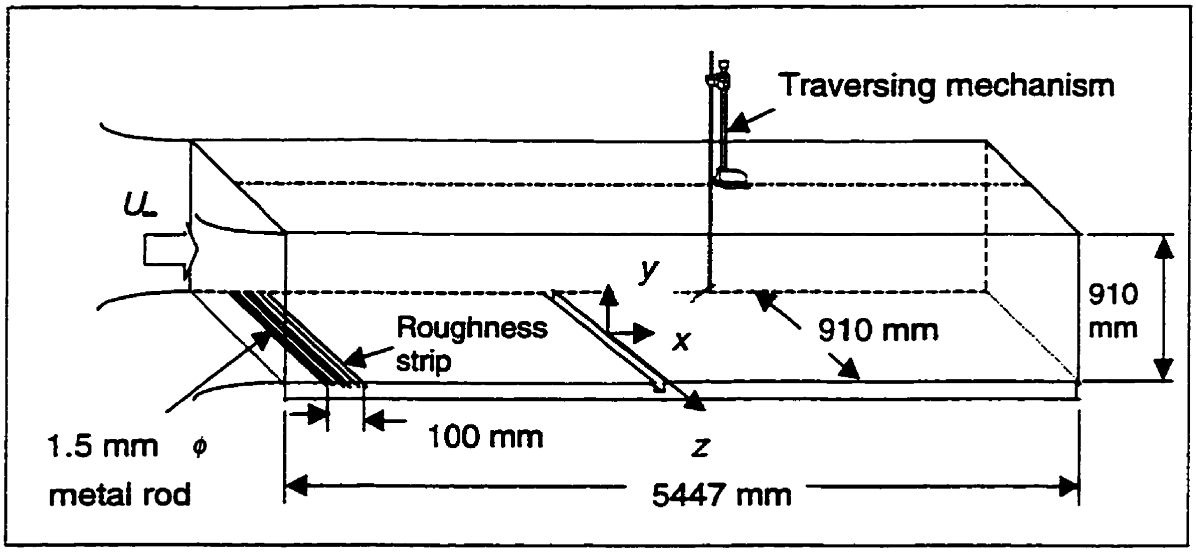

Figure 3.1.1 Wind tunnel test section configuration.

A centrifugal blower driven by a 19 kW motor is used in the wind tunnel. The air passes through a screened diffusor and a large settling chamber with three single-piece precision screens. The air is accelerated into the test section through a 5:1 contraction. The maximum free stream velocity in the test section is approximately 15 m/sec. The free stream turbulence intensity is less than 0.5% at all velocities. The velocity in the test section is changed using motorized variable angle inlet vanes on the blower.

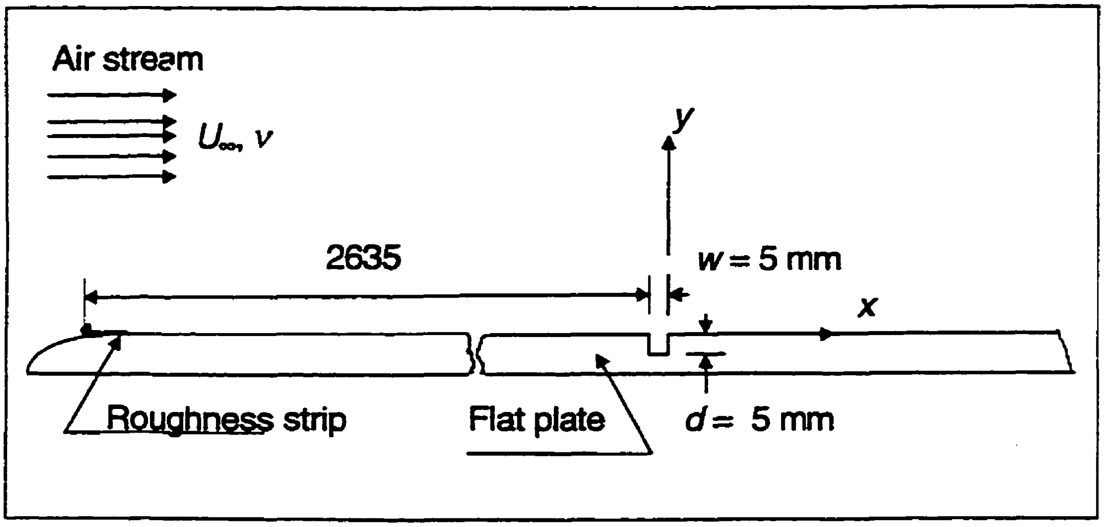

Figure 3.1.2 A schematic of test-plate showing a single transverse square cavity

Experiments were performed at two free stream velocities of 2 m/s and 5.5 m/s. At each free stream velocity, measurements were made on a smooth wall flat plate and a flat plate with a single transverse square cavity (Figure 3.1.2). The free stream velocities of 2 m/s and 5.5 m/s correspond to Reynolds numbers, based on the cavity width, of 645 and 1774, respectively. A roughness strip, consisting of a 100 mm wide sand paper (series 0811) and a 1.5 mm diameter cylindrical rod were used to trip the boundary layer at the leading edge of the plate. The flat plate is made of 25 mm thick acrylic and is mounted horizontally on the floor of the wind tunnel. After the initial measurements on the smooth wall, a transverse square cavity ($w/d = 1$, $w = 5$ mm) was cut on the plate at a distance of 2635 mm from the leading edge.

For the smooth wall, measurements were obtained at 8 streamwise locations. For the flat plate with the transverse square groove, measurements were obtained at seventeen streamwise locations for both Reynolds numbers. Three locations were upstream of the cavity, and fourteen locations downstream of the cavity.

The hot-wire probe used for the velocity measurements was connected to a specially designed traversing mechanism using a Mitutoyo height gauge. The mechanism is used to traverse the hot-wire in the wall-normal direction. The traverse is installed on rails mounted on the roof of the tunnel. This traverse has a maximum span of 18 inches and a minimum linear division of 0.001 in (0.01 mm).

3.2 Hot Wire Anemometers

3.2.1 General Description

Hot wire anemometers are widely used for velocity measurements and play an important role in experimental fluid dynamics. The hot wire sensor is usually made of tungsten or platinum, and the sensors can be miniaturized to obtain a high spatial resolution. They have a high degree of accuracy, a very good frequency response, and are cost effective and relatively easy to set up. The frequency response of hot wire anemometers can be as high as 1 MHz (Goldstein, 1983), while the sensor diameter is of order 1 to 10 μm. The repeatability of the measurements is excellent with a deviation on the order of a few percent. Moreover, the hot wire is relatively cheap compared to other measurement techniques like Laser Doppler Velocimetry (Goldstein, 1983). There are, however, several disadvantages of using hot wire anemometers. The sensors are very fragile, and it is very difficult to obtain measurements very close to a wall, especially if the wall material is conductive.

The hot wire anemometer works on the principle of conservation of energy. The sensor is maintained at a temperature greater than the flowing fluid, and the energy transfer from the sensor to the fluid is correlated to the flow velocity. It is very difficult to obtain an analytical correlation function, and in-situ calibrations must usually be performed.

If an electrical current, I, is supplied to the sensor wire, the energy balance for the sensor can be expressed as

$$I^2 R_w = h\,A\,(T_w - T_\infty) \tag{3.1}$$

where R_w is the wire resistance at the operating temperature, h is the convection heat transfer coefficient, A is the active wire surface area, T_w is the wire operating temperature, and T_∞ is the fluid temperature. The relation between the wire temperature and its resistance is

$$R_w = R_0[1+\alpha\,(T_w - T_\infty)] \tag{3.2}$$

where R_0 is the wire resistance at the reference temperature T_∞ (usually the air temperature), and α is the temperature coefficient of resistivity of the wire. The wire temperature can then be expressed as

$$(T_w - T_\infty) = (R_w - R_0)/(\alpha R_0) \tag{3.3}$$

Combining Eq. (3.1) and (3.3), one obtains

$$I^2 R_w = h\,A\,(R_w - R_0)/(\alpha R_0) \tag{3.4}$$

In Eq. (3.4), both h and I are functions of the fluid velocity magnitude, $|\vec{S}|$.

This can be expressed in a convenient form (Bruun, 1995) as

$$I^2R_w/(R_w - R_0) = A + B\left|\bar{S}\right|^n \tag{3.5}$$

Eq. (3.5) is referred to as King's Law, and the constants A, B, and n need to be determined by a suitable calibration procedure.

Hot wires can be operated in two different modes. The first method is called Constant-Current Anemometry (CCA), while the second method is called Constant-Temperature Anemometry (CTA). In the CCA mode, the electrical current to the wire is kept constant, while the wire temperature varies. In the second method, the wire temperature (and thereby its resistance) is kept constant, while the electrical current which flows through the wire varies. The basic configurations of the two operation modes are shown in Figure 3.2.1 and 3.2.2.

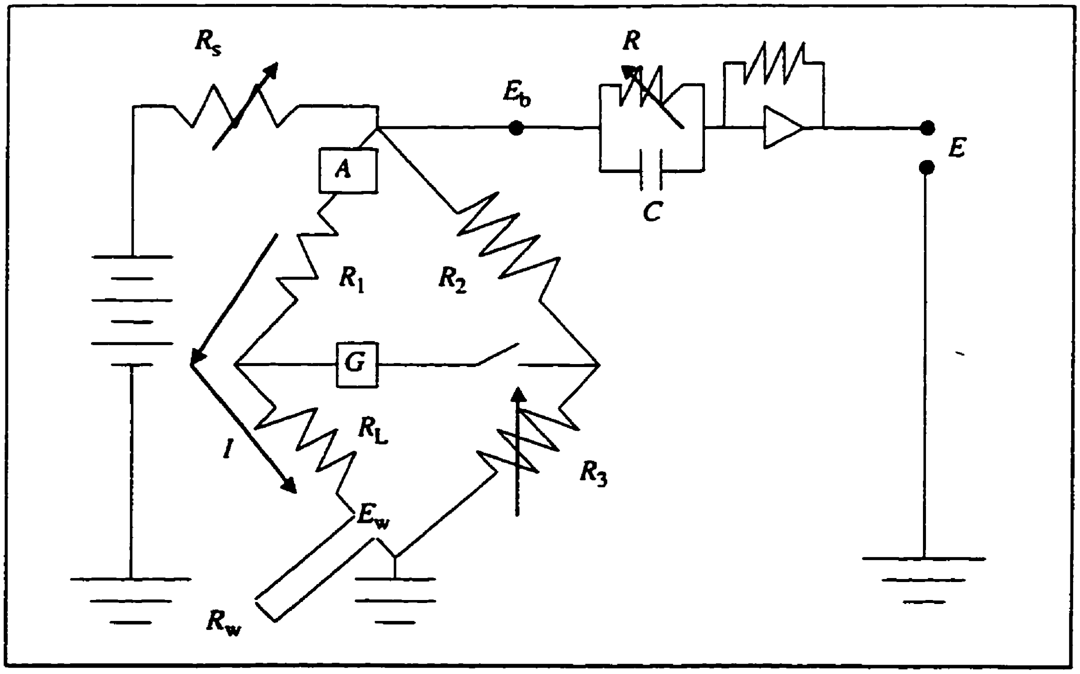

Figure 3.2.1 A typical CCA circuit incorporating a Wheatstone bridge and an R-C compensation circuit. (Reproduced from Bruun, 1995)

3.2.2 Constant Temperature Anemometry.

In the present investigation, Constant Temperature Anemometry was used to measure velocity. Both Single-normal (SN) wire and X-wire were used to measure the velocity fluctuations. While the X-wire can be used to measure velocity fluctuations in two orthogonal directions, the SN wire can be used only for a single velocity component. The wires were operated at an overheat ratio of 1.5.

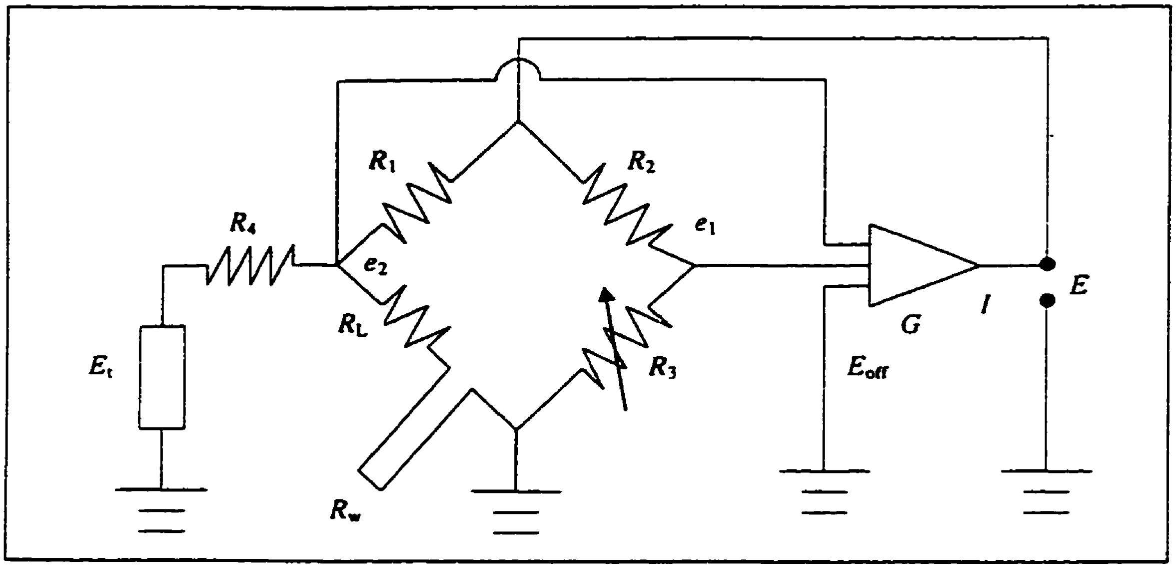

Figure 3.2.2 A typical CTA circuit containing a Wheatstone bridge, a feedback amplifier, and electronic-testing subcircuit. (Reproduced from Bruun, 1995).

A DANTEC 55P05 boundary layer type probe was used for the boundary layer measurements. The sensor is a 5 μm diameter Platinum-plated tungsten (Pt-plated tungsten) wire with an effective (active) length of 1.25 mm (Figure 3.2.3). The ends of the wire are copper and gold plated to a diameter of approximately 30 μm.

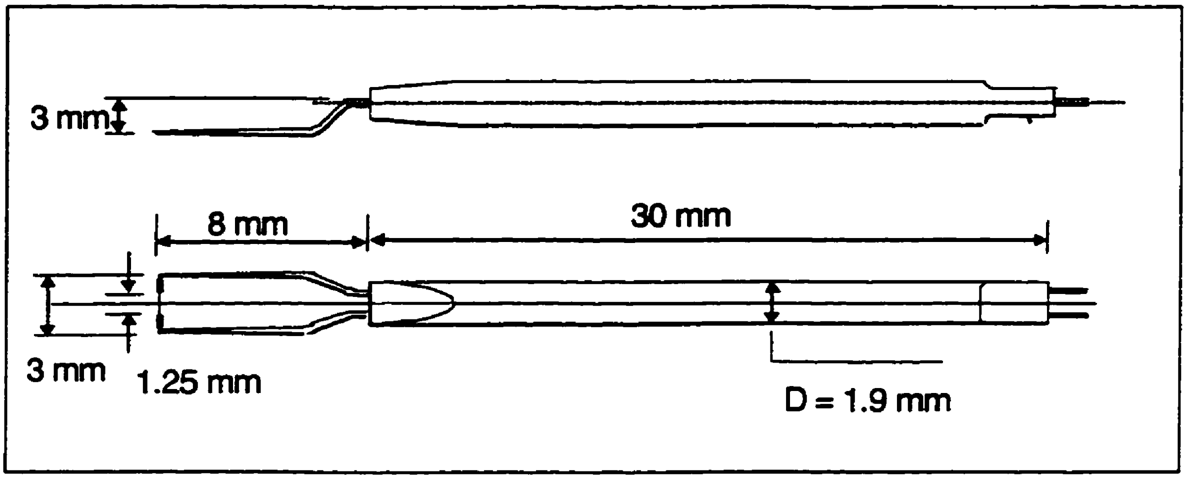

Figure 3.2.3 Basic dimension of DANTEC 55P05 boundary layer type SN-wire

The ratio of the effective length to diameter, *l/d*, is an important parameter and is usually about 200 (Ligrani and Bradshaw, 1987). If this ratio is too large, the spatial resolution is poor. On the other hand, if the ratio is too small, then heat loss from the wire to its prongs can produce a significant effect on the measurements. For the wire used in the present investigation, the ratio *l/d* is 250; hence, the spatial resolution is acceptable, and the heat loss effect to the prongs is negligible.

The velocity measurements were made using a DANTEC 55M01 standard bridge. The hot wire signals were digitized using a 16 channel 12 bit Keithley 570 System Analog to Digital (A/D) converter, interfaced to a 486 DX-AT personal computer. For the hot-wire calibrations, the velocity was measured using a Pitot-static tube connected to a differential pressure transducer (Furness type FCO34) with a range 0.00 - 0.10 inches water.

An HP 5420b digital spectrum analyzer and an oscilloscope were used to monitor the hot-wire signals on-line. The analyzer consists of three parts: a 54470B type digital filter, a 54410A type analog to digital (A/D) converter, and a display unit. The A/D converter can handle an analog input signal up to 25.6 kHz in frequency and ± 10 VDC peak in amplitude.

3.3 Preston Tube

A Preston tube was used to measure the wall shear stress at the higher freestream velocity of 5.5 m/s. The tube has an outside diameter of 1.55 mm, and was placed on the test surface, parallel to the free-stream velocity (Figure 3.3.1). Static pressure was obtained using the static pressure tap (hole) of a Pitot-static tube located 40 mm above the wall. The opening of the Preston tube was located at the same streamwise location of the static pressure tap. The Preston tube was attached to the stem of the Pitot-static tube. The differential pressure ($\Delta p = p_H - p_L$), was measured using a Furness model FCO34 differential pressure transducer.

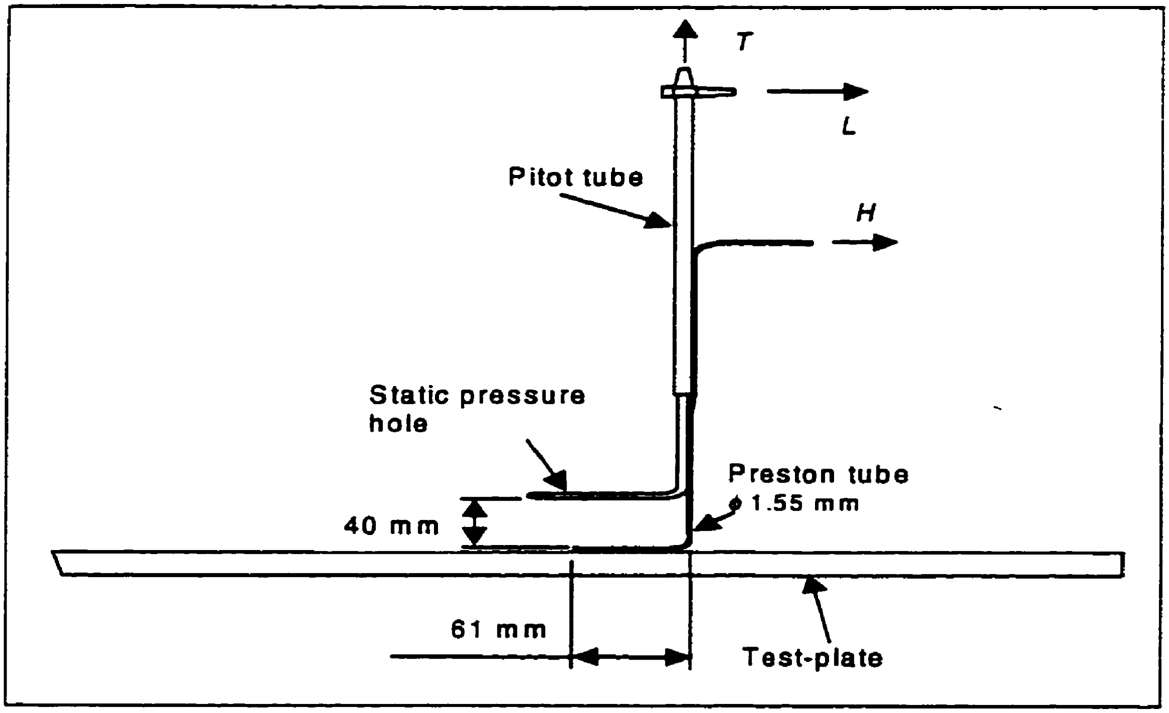

Figure 3.3.1 Preston tube arrangement. *H* is total pressure from Preston tube, *L* is static pressure from static hole of Pitot-static tube, and *T* is stagnation pressure from Pitot-static tube.

3.4 Data Acquisition

A schematic of the data acquisition system is shown in Figure 3.4.1. The sensor measures the physical variable and the output is usually an analog signal. The signal passes through a signal conditioning unit (SCU), which converts it to a form that can be read by an A/D converter. For example, the output voltage from SCU must match the input voltage range of the A/D converter. The purpose of the A/D converter is to convert the analog output from the signal conditioning unit into a digital format which can be read by a personal computer. Since the A/D converter used has a 12 bit resolution and an input voltage range of 0.0 - 5.0 VDC, the maximum resolution of this unit is 0.00122 Volts (1.22 millivolts).

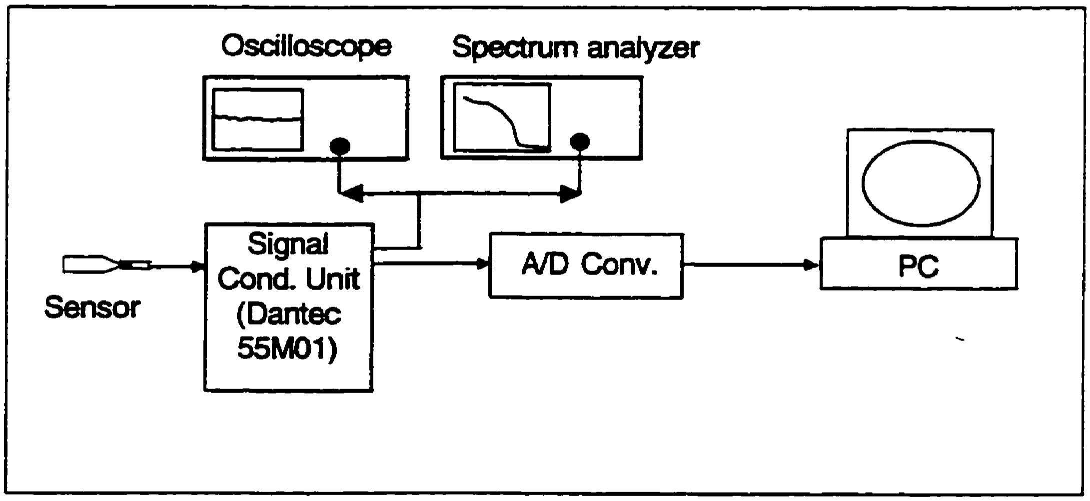

Figure 3.4.1 Data Acquisition System

3.5 Determination of Probe Distance from the Wall

Accurate determination of the hot-wire distance from the wall is very important for proper data reduction. To determine the distance of the wire-sensor from the wall, a reflection method was used. A theodolite with a minimum vertical angle division of 30 secs (= 1.45 x 10^{-4} rad.) was used to measure the angle between the sensor and its reflection on the wall. The accuracy of this method also depends on the distance between the theodolite and the sensor. Due to space constraints, the maximum distance between the theodolite and the sensor is about 2.5 m. Figure 3.5.1 shows a schematic diagram of the theodolite setup to determine the probe distance from the wall.

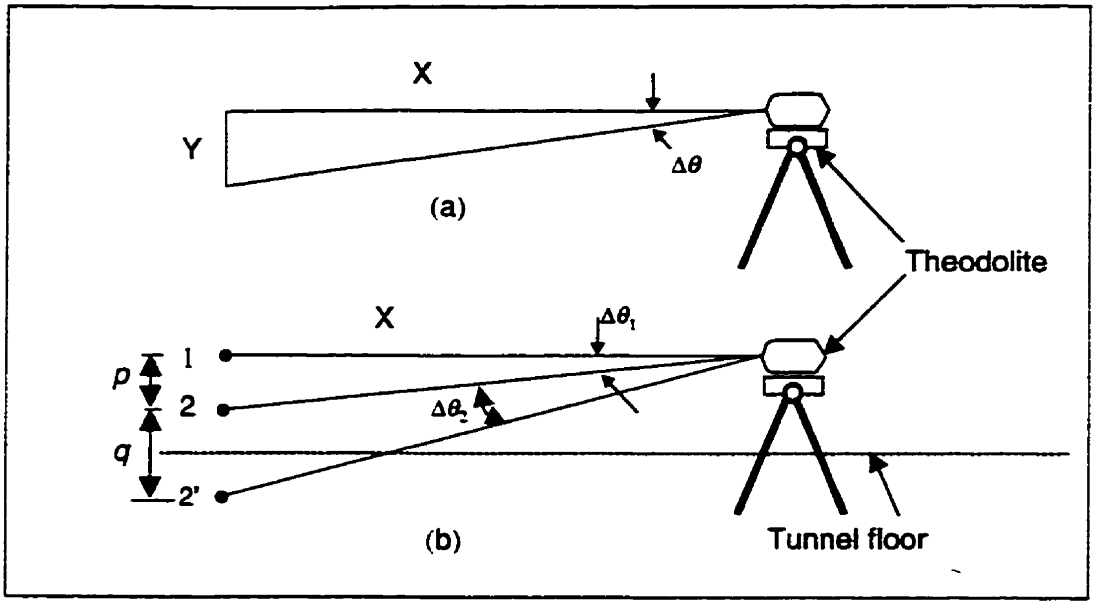

Figure 3.5.1 Determination of the Hot-wire Distance from the Wall

There are two main steps in this method. In the first step, the probe is brought close to the wall (approximately 2 mm from the wall). The orientation of the probe is adjusted so that the sensor is parallel to the wall. At this location, the theodolite vertical reading is set to zero. The probe is then moved 1 mm closer to the wall, and the angle subtended by the original and new sensor location at the theodolite is measured. From the angle measurement ($\Delta\theta_1$), the distance (X) of the theodolite to the probe can be determined. In the second step, the theodolite is focused on the reflection of the probe on the wall. The angle ($\Delta\theta_2$) subtended by the sensor and its reflection is measured. From this, one can determine the distance between the probe and its reflection (distance between points 2 and 2' in Figure 3.5.1).

$$Y = X \tan(\Delta\theta) \tag{3.6}$$

For small $\Delta\theta$,

$$Y = X\Delta\theta \tag{3.7}$$

And hence

$$q = X\Delta\theta_2 \tag{3.8}$$

The probe distance from the wall is then ($q/2$).

The accuracy of the measurement depends on the accuracy of the theodolite and the distance of the theodolite from the probe. Assuming a distance of 1 m, the accuracy can be estimated as:

$$Y_{min} = X\Delta\theta_{min} \tag{3.9}$$

where $\Delta\theta_{min} = 30$ secs $= 1.45 \times 10^{-4}$ rad.

Hence, the minimum linear vertical reading (Y_{min}) is then

$$\begin{aligned} Y_{min} &= 1 \text{ m} \times 1.45 \times 10^{-4} \text{ rad} \\ &= 1.45 \times 10^{-4} \text{ m} \\ &\approx 0.15 \text{ mm} \end{aligned}$$

This value is also the minimum q-value, and, therefore, the minimum distance of the sensor from the wall that can be measured with the theodolite is ≈ 0.075 mm.

Chapter 4

Data Reduction Procedures

4.1 Hot Wire Calibrations

Proper hot-wire calibrations are important for accurate velocity measurements using hot-wire anemometry. The calibrations are performed both before and after the measurements to ensure that the results obtained are valid. A Pitot-static tube located alongside the hot-wire sensor was used for the calibrations. For the calibration, the sensor and the Pitot-static tube are located in the central part of wind tunnel test section (Figure 4.1.1).

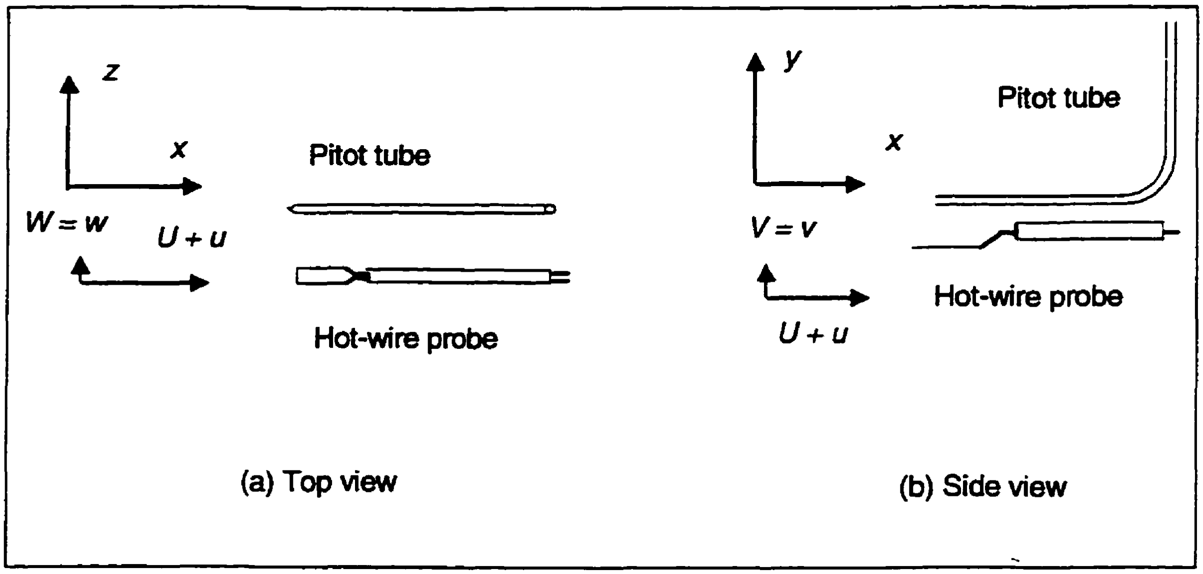

(a) Top view (b) Side view

Figure 4.1.1 Hot-wire probe and Pitot-static tube arrangement in the wind tunnel for calibration purposes

4.1.1 Calibration of a Single-normal (SN) Hot-wire

The calibration procedure of a SN-wire is as follows. The velocity is measured using a Pitot-static tube connected to a differential pressure transducer (FC034). The differential pressure transducer has a full scale reading of 0.100 inches water with a corresponding analog output of 0.0 to 5.0 VDC. The full scale reading corresponds to an air velocity of approximately 6.20 m/s. The analog output of the pressure transducer and output of the hot-wire anemometer are directly sampled into a personal computer using an A/D converter. A schematic diagram of the instrumentation for the hot-wire calibration is shown in Figure 4.1.2.

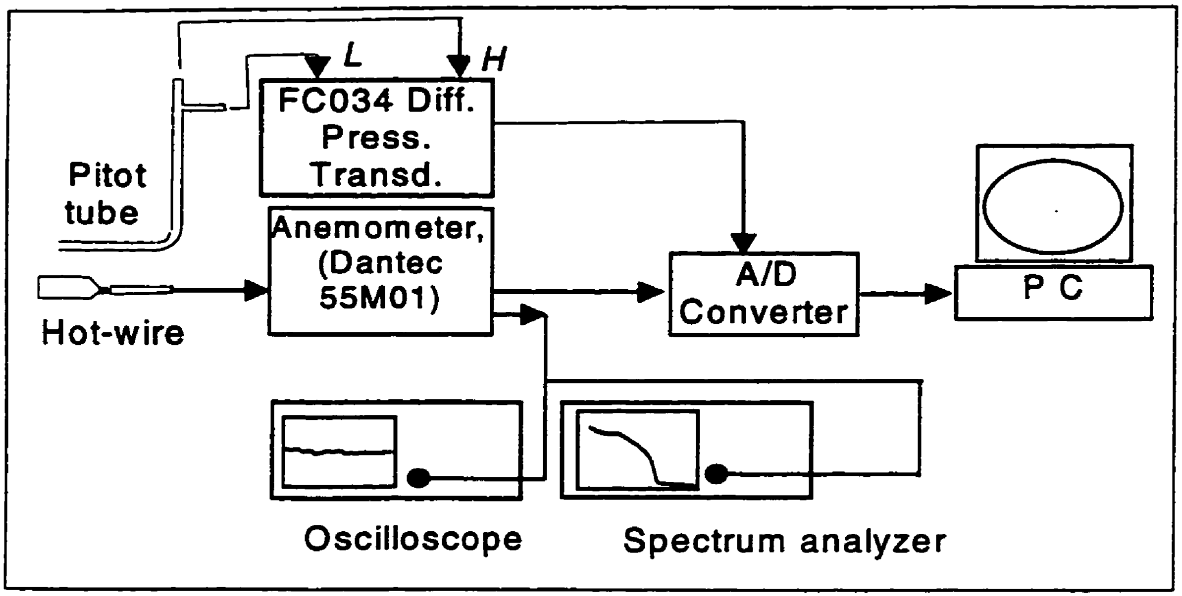

Figure 4.1.2 Block diagram for hot-wire calibration purposes. *L* is low-pressure and *H* is high-pressure outputs from the Pitot- static tube.

The output of the hot-wire anemometer is also connected to a spectrum analyzer and an oscilloscope to check the signal-to-noise ratio. The measurements are taken only if there is no significant noise in the signal.

Typically a set of 20 – 30 calibration points are required to obtain an accurate calibration curve (Bruun, 1995). However, Bruun (1988) showed that an accurate calibration curve can be obtained with as few as 10 data points. The calibration points must be selected to cover the entire velocity range of interest. To obtain a statistically stationary value at each point, data was sampled at a frequency of 20 Hz for 50 seconds. The data was time averaged to obtain mean values for each point. For each calibration curve, a minimum of ten data points are used.

A third order polynomial is employed for the functional relationship between the hot-wire signal (Volts) and the velocity, U. This can be expressed as

$$U(E) = a + bE + cE^2 + dE^3 \tag{4.1}$$

where U is obtained from the Pitot-static tube, while E is the hot-wire output. The constants $\boldsymbol{a}$, $\boldsymbol{b}$, $\boldsymbol{c}$, and $\boldsymbol{d}$ are obtained by a least-squares curve fit to the data. A typical calibration curve for a single-normal hot-wire is shown in Figure 4.1.3.

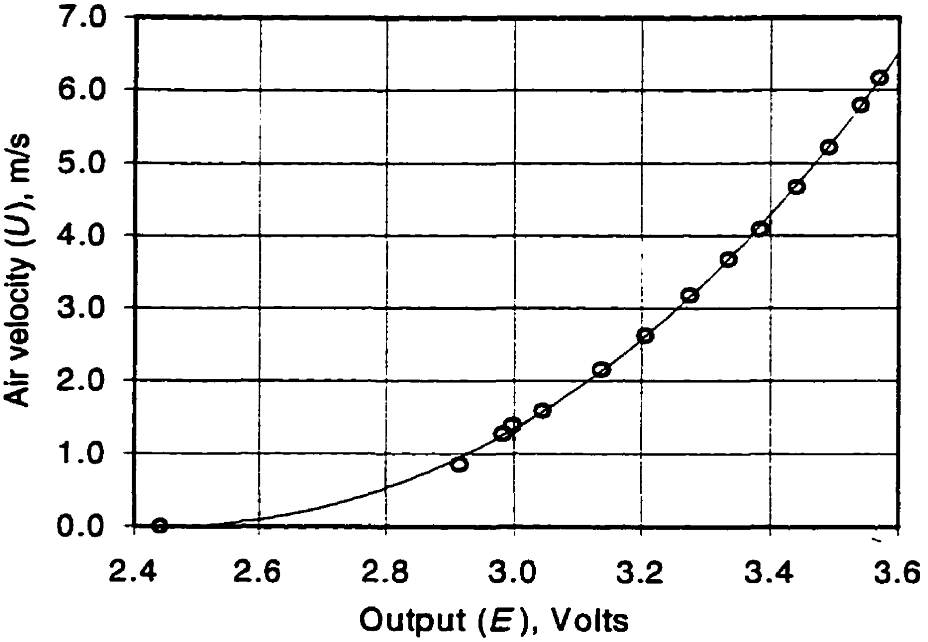

Figure 4.1.3 Typical calibration curve of SN-wire. Symbols: o, data; ——, third order polynomial fit.

For the single-normal hot-wire, velocity can be obtained directly from the anemometer output using the calibration curve. The data reduction is performed using

MATLAB® and the corresponding mean, fluctuating, and rms- values are simultaneously calculated (a program listing is attached in Appendix A).

4.1.2 Calibration of an X-Wire

The calibration procedure for an X-wire is more involved than that of a SN-wire. An X-wire consists of two independent inclined wires, usually at right angles to each other. Each sensor (wire) is connected to an anemometer unit, and the output from the two anemometers are recorded simultaneously along with the output from the Pitot-static tube.

The calibration procedure of an X-wire consists of two steps. First, a velocity (*U*)-voltage (*E*) calibration curve of the two wires in the un-yawed position is obtained, similar to that for a SN-wire. Typical *U-E* calibration curves for the two sensors of an X-wire is shown in Figure 4.1.4.

The instantaneous velocity $\vec{S}$ can be resolved into its components (by assuming that the z-component of $\vec{S}$ is very small compared to the two other components) as

$$\tilde{S}(t) = \tilde{u}(t)\ \hat{i} + \tilde{v}(t)\ \hat{j} \tag{4.2}$$

where

$$\tilde{u}(t) = \left|\tilde{S}(t)\right| \cos\beta(t) \tag{4.3}$$

and

$$\tilde{v}(t) = \left|\tilde{S}(t)\right| \sin\beta(t) \tag{4.4}$$

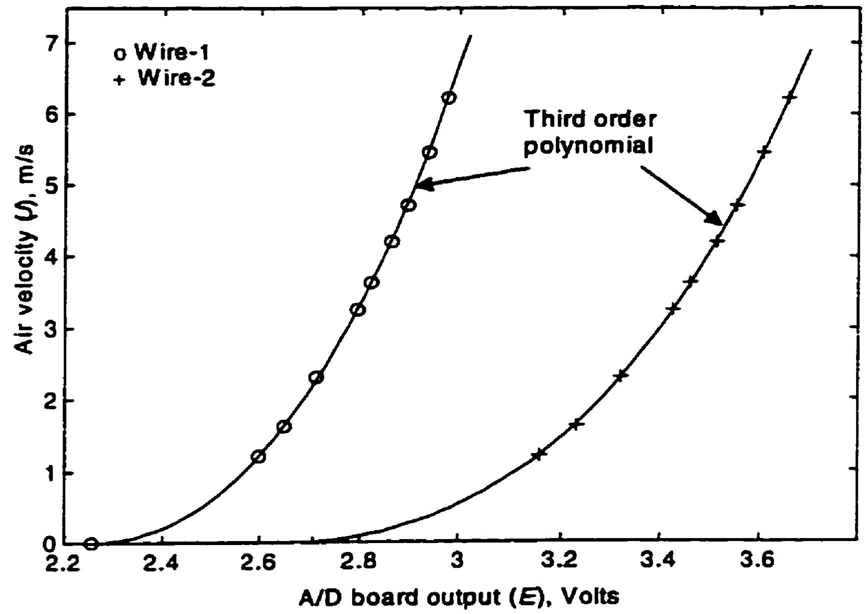

Figure 4.1.4 Typical calibration curves of an X-wire.

Secondly, a yaw-calibration is performed separately for each wire. Consider a configuration of the X-wire as shown in Figure 4.1.5 and 4.1.6. The $\tilde{u}(t)$ and $\tilde{v}(t)$ components can be calculated if the instantaneous angle β, and the velocity magnitude $|\vec{S}|$ can be determined. The concepts of effective angle and effective cooling of an inclined wire are used to estimate β and $|\vec{S}|$. These concepts were first introduced by Bradshaw (1971).

Assuming the velocity component perpendicular to the plane of the X-wire is small, the effective cooling velocity of the wire, V_{eff}, is expressed as

$$V_{\mathrm{eff}} = |\vec{S}|\, f(\theta) \tag{4.5}$$

Using a cosine cooling law (Bradshaw; 1971), Eq. (4.5) has the form

$$V_{\mathrm{eff}} = |\vec{S}| \cos(\theta_{\mathrm{eff}}) \tag{4.6}$$

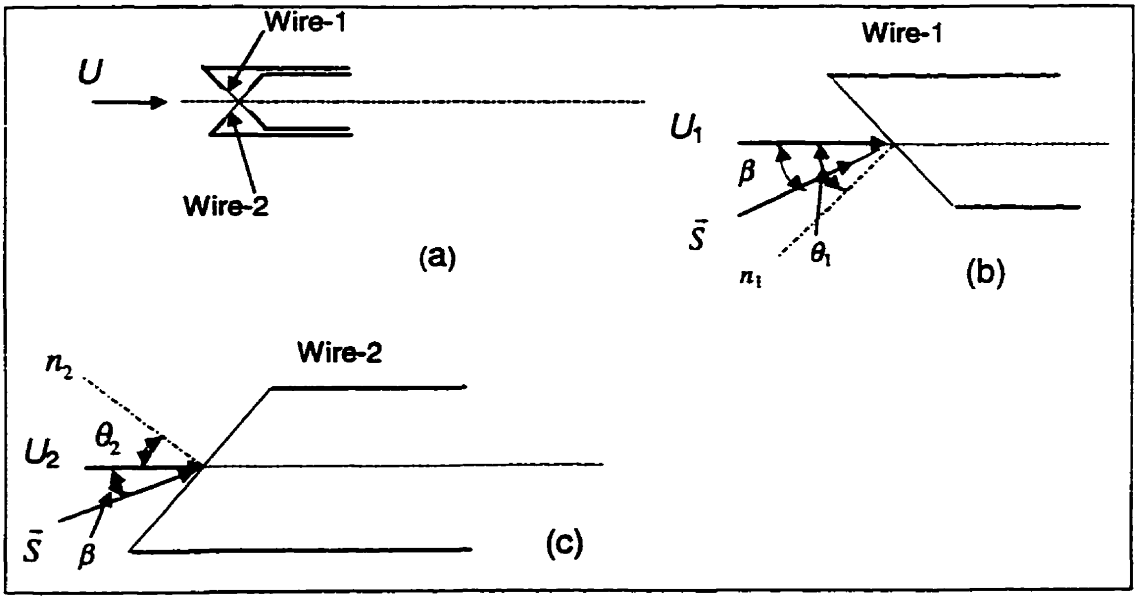

Figure 4.1.5 Wires of an X-wire. $\bar{S}$ is the instantaneous velocity vector that makes an angle of β with the main flow direction.

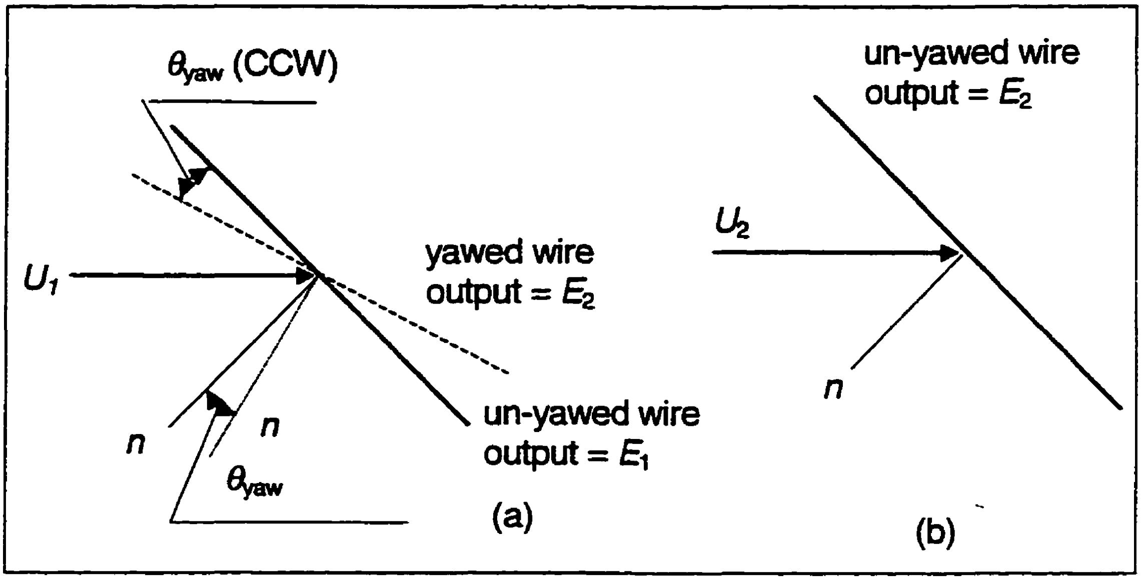

Figure 4.1.6 Yawed and un-yawed wire with their output voltage

Now, suppose the inclined hot wire (the solid line in Figure 4.1.6) is placed in a free stream velocity U_1, and the corresponding anemometer output voltage is E_1. When the wire is yawed by an angle θ_{yaw} in a counter clock wise direction, as shown by a dashed line, let the output voltage of the anemometer be E_2. The voltage E_2 corresponds to a velocity of U_2 if the wire was in the un-yawed position (from the appropriate calibration curve, see Figure 4.1.4). Since the anemometer output of the wire is the same when the wire is in the yawed position with velocity U_1, and the wire in the un-yawed position with velocity U_2, we can formulate

$$U_2 \cos(\theta_{eff}) = U_1 \cos(\theta_{eff} + \theta_{yaw}) \tag{4.7}$$

The effective angle, θ_{eff}, can then be expressed as

$$\theta_{eff} = \tan^{-1}\left[\frac{\cos(\theta_{yaw}) - \frac{U_2}{U_1}}{\sin(\theta_{yaw})}\right] \tag{4.8}$$

$U_2 \cos(\theta_{eff})$ in Eq. (4.7) is called *the effective cooling velocity* at an effective angle θ_{eff}. U_l and U_2 are obtained from the velocity-output voltage calibration, and for a given θ_{yaw}, the effective angle can be calculated. A complete yaw calibration was performed by yawing the wire from –30° to +30° in step of 5°. At each yaw position, θ_{eff} was calculated and an average value of the effective angle can be determined. A typical variation of θ_{eff} with θ_{yaw} is shown in Figure 4.1.7.

4.2 Determination of Streamwise and Wall-normal Velocity Components with an X-Wire

By using an X-wire, the streamwise and wall-normal velocity components ($\tilde{u}(t)$ and $\tilde{v}(t)$, respectively) can be determined. The $\tilde{u}(t)$ and $\tilde{v}(t)$ can be expressed in terms of the mean values U and V, and the fluctuating components $u(t)$ and $v(t)$ as

$$\tilde{u}(t) = U + u(t) \tag{4.9}$$

and

$$\tilde{v}(t) = V + v(t) \tag{4.10}$$

respectively.

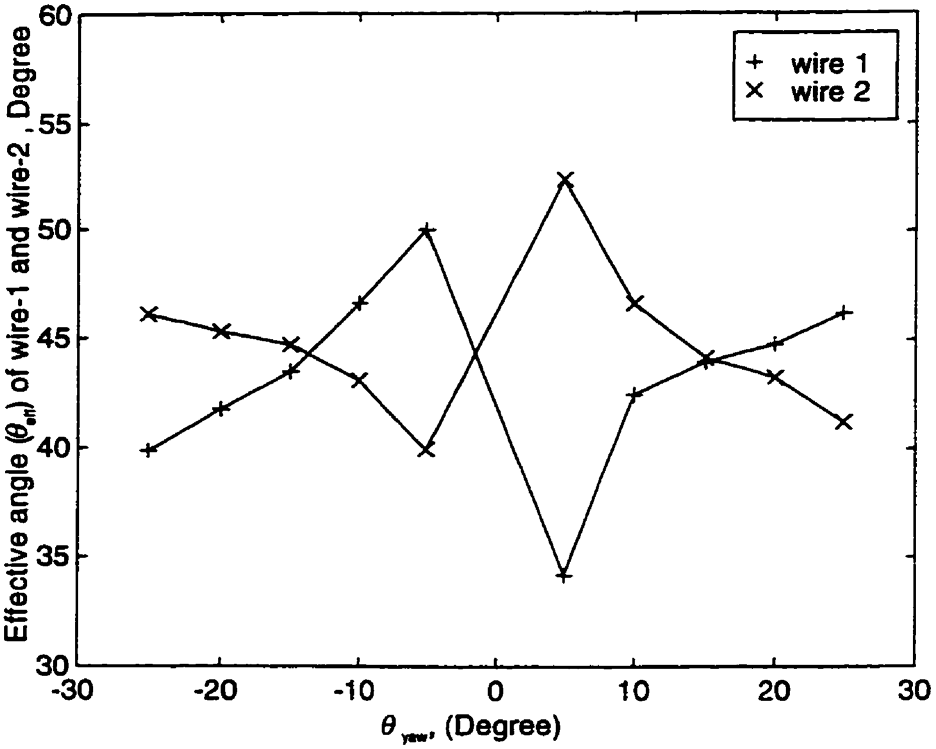

Figure 4.1.7 A typical plot of θ_{eff} as a function of θ_{yaw}. Average of $\theta_{eff,1}$ and $\theta_{eff,2}$ are 43.4^{O} and 44.7^{O}, respectively.

With reference to Figure 4.1.5, the cosine law states that

$$U_1 \cos(\theta_1) = S \cos(\theta_1 - \beta) \tag{4.11}$$

and

$$U_2 \cos(\theta_2) = S \cos(\theta_2 + \beta) \tag{4.12}$$

where θ_1 and θ_2 are the effective angles of wire-1 and wire-2, respectively. Since θ_1 and θ_2 are known, and U_1 and U_2 can be obtained from the calibration curve, the instantaneous velocity magnitude (S) and velocity vector angle (β), can be obtained by simultaneously solving Eq. (4.11) and (4.12) (Bruun et al., 1990a and b; Browne et al. 1989):

$$\beta = \tan^{-1}\left\{ \frac{\left[\frac{U_1}{U_2} - 1 \right]}{\tan(\theta_1) + \frac{U_1}{U_2}\tan(\theta_2)} \right\} \tag{4.13}$$

and

$$S = \frac{U_1 \cos\theta_1}{\cos(\theta_1 - \beta)} \tag{4.14a}$$

or

$$S = \frac{U_2 \cos\theta_2}{\cos(\theta_2 + \beta)} \tag{4.14b}$$

Once S and β are determined, $\tilde{u}(t)$ and $\tilde{v}(t)$ can be calculated with Eq. (4.3) and (4.4), respectively. The data reduction was performed using MATLAB®, and a program listing is attached in Appendix A.

4.3 Mean and Fluctuating Velocities

Typical streamwise and wall-normal velocity traces obtained from an X-wire are shown in Figure 4.3.1 and 4.3.2. The mean velocities in the *x*- and *y*-direction can be obtained as

$$U = \lim_{n\to\infty}(1/n)\sum_{i=1}^{n}\tilde{u}_i \tag{4.15}$$

and

$$V = \lim_{n\to\infty}(1/n)\sum_{i=1}^{n}\tilde{v}_i \tag{4.16}$$

The fluctuating components of the velocity in the streamwise and wall-normal directions (see Figure 4.3.3 and 4.3.4) can be obtained by subtracting the mean values:

$$u(t) = \tilde{u}(t) - U \tag{4.17}$$

$$v(t) = \tilde{v}(t) - V \tag{4.18}$$

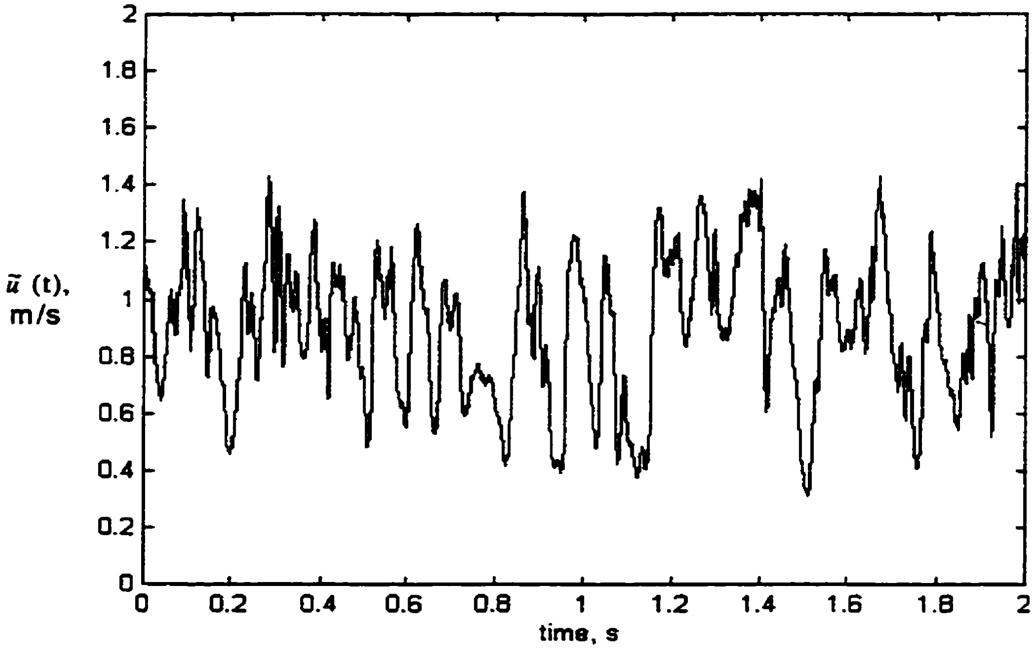

Figure 4.3.1 Streamwise velocity trace at y/δ = 0.0233, U_∞ = 2.10 m/s. Data is for the smooth- wall and obtained using an X-wire. U = 0.87 m/s.

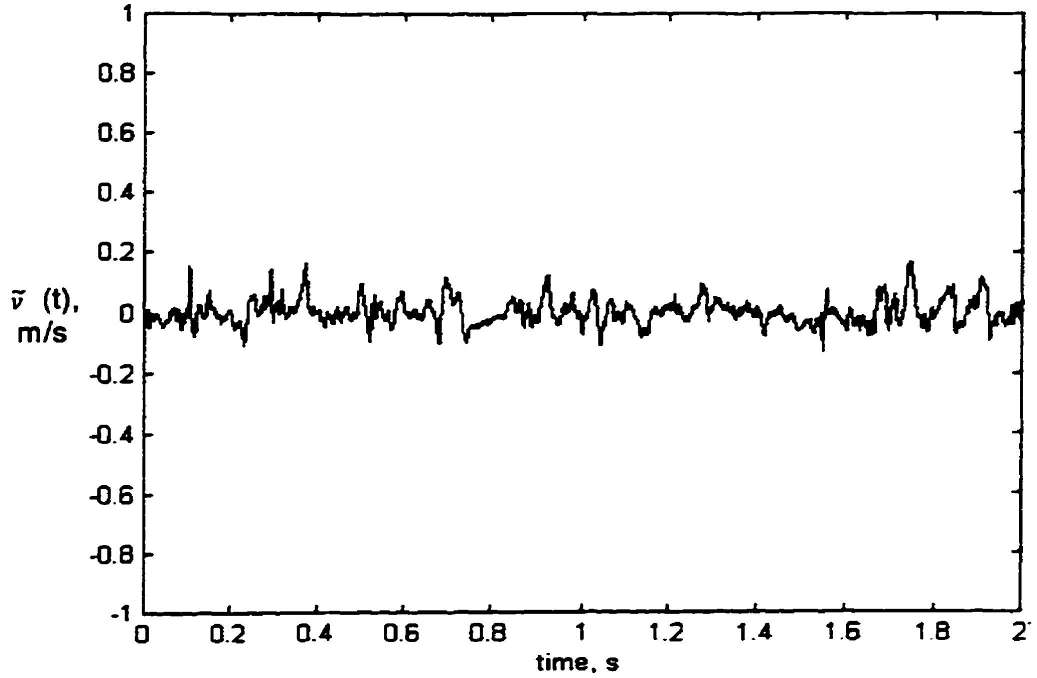

Figure 4.3.2 Velocity trace in the wall-normal direction at $y/\delta = 0.0233$. $U_\infty = 2.10$ m/s, $V = 0.0075$ m/s.

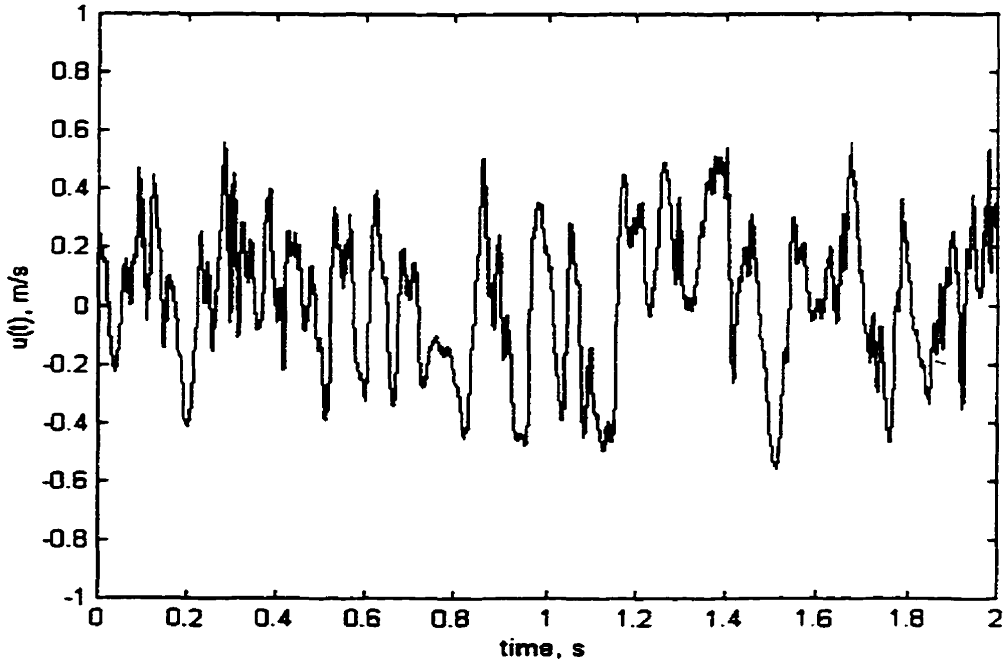

Figure 4.3.3 Streamwise velocity fluctuation. $U_\infty = 2.10$ m/s. Data is for the smooth-wall and obtained using an X-wire.

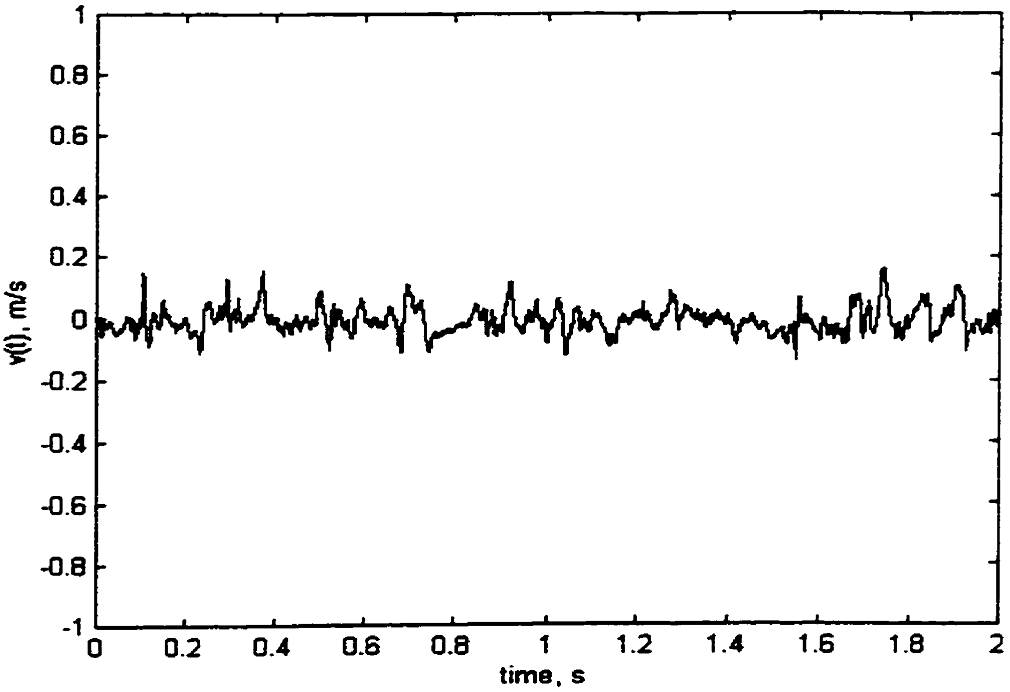

Figure 4.3.4 Wall-normal velocity fluctuation at $y/\delta = 0.0233$. $U_\infty = 2.10$ m/s. Data is for the smooth wall and obtained using an X-wire.

4.4 Wall Shear Stress

An accurate estimation of the wall shear stress is necessary to predict the skin friction drag associated with boundary layers. As mentioned in section 1.3, the wall shear stress was estimated in four different ways: from a power law approximation of the velocity profile, Clauser chart method, gradient of mean velocity profile at the wall, and from Preston tube measurements. The relation between the wall shear stress (τ_w), and the friction velocity (u_τ) can be expressed as

$$\tau_w = \rho\,(u_\tau)^2 \qquad (4.19)$$

Following Barenblatt's arguments of incomplete similarity (Eq. (2.30)), Ching et al. (1995a) showed that u_τ can be expressed as:

$$u_\tau = U_\infty \left\{ \frac{1}{\exp(3/2\alpha)} \left(\frac{\exp(3/2\alpha)}{C} \right)^{1/(1+\alpha)} \right\} \tag{4.20}$$

where α and C are calculated with Eq. (2.31) and (2.32), respectively. Djenidi et al. (1997) showed that u_τ determined from Eq. (4.20) was within $\pm 0.57\%$ to that obtained from Preston tube measurements for R_θ = 940. The power law approximation is compared with the present data for R_θ = 1042 and DNS data (Figure 4.4.1). There is good agreement between the experimental data and the power-law in the region $30 \lesssim y^+ \lesssim 500$. The mean velocity data (normalized by u_τ obtained from the power law approximation) are also in good agreement with the DNS data down to $y^+ \approx 3$. At $y^+ \lesssim 3$, the heat conduction from the sensor to the wall becomes significant, and results in an increase in the anemometer output voltage. This is reflected as a spurious increase in velocity as the wall is approached. The power law approximation provides a reliable estimate of u_τ, especially at low Reynolds numbers.

The Clauser chart method (log-law method) assumes a universal mean velocity profile in the overlap region. The Clauser chart is only appropriate if the Reynolds number is sufficiently high ($R_\theta \gtrsim 1500$) for a log law region to exist. At low R_θ, the existence of the log region is questionable (Ching et al., 1995a). Clauser (1956) suggested the following relationship for U/U_∞,

$$\frac{U}{U_\infty} = \frac{u_\tau}{U_\infty} g\left[\left(\frac{u_\tau}{U_\infty} \right) \left(\frac{U_\infty y}{\nu} \right) \right] \tag{4.21}$$

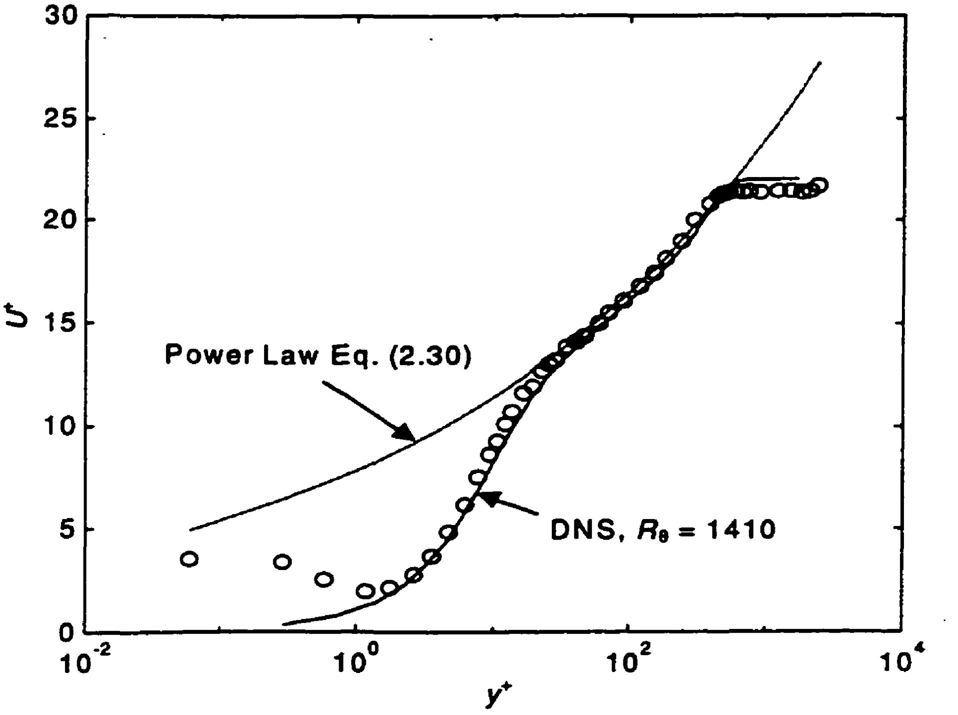

Figure 4.4.1 Mean velocity distribution. Symbols: ○, recent data at R_θ = 1042; — · — · —, Power law approximation at R_θ = 1042; and ——, DNS at R_θ = 1410.

The friction velocity was determined by plotting U/U_∞ versus $U_\infty y/\nu$ on semilog axes. A typical plot of the Clauser chart for the present smooth-wall data at R_θ = 2470 is shown in Figure 4.4.2. The friction velocity is determined by obtaining a best fit to the data, and the most appropriate value for u_τ in this case is 0.2268 m/s (C_f = 0.003379). The straight lines on Figure 4.4.2 are of the form

$$\frac{U}{U_\infty} = \frac{u_\tau}{U_\infty}\left[\frac{1}{\kappa}\ln\left(\frac{U_\infty y}{\nu}\frac{u_\tau}{U_\infty}\right)+B\right] \qquad \textbf{(4.22)}$$

Eq. (4.22) can be expressed as

$$\frac{U}{u_\tau} = \frac{1}{\kappa}\ln\left(\frac{u_\tau y}{\nu}\right)+B \qquad \textbf{(4.23)}$$

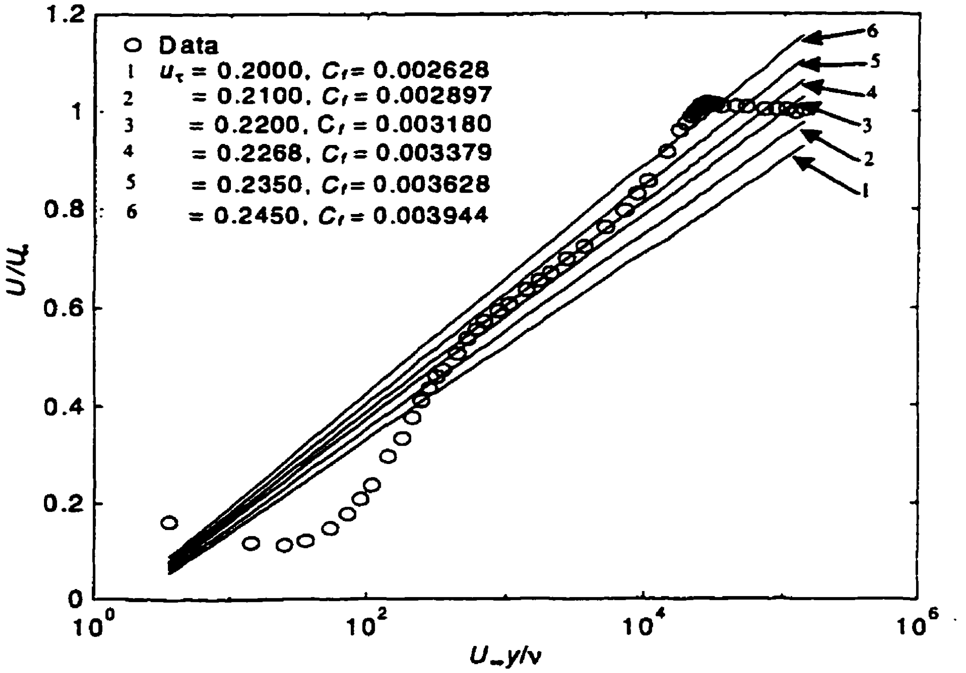

Figure 4.4.2 Typical Clauser chart for determination of u_τ. Friction velocity (u_τ) is in m/s.

In the current study, the most appropriate values of κ and B are 0.41 and 5.0, respectively, at $R_\theta = 1000$. On the other hand, at the higher Reynolds numbers ($R_\theta = 3000$), κ and B are 0.44 and 6.13, respectively. The latter values of κ and B are similar to those obtained by Zagarola and Smits (1997) for turbulent pipe flow ($\kappa = 0.436$ and $B = 6.13$). The constants κ and B are obtained from the best fit to the experimental data, and there is no formal basis to obtain unique values for κ and B.

The data of Figure 4.4.2 is re-plotted according to Eq. (4.23) using u_τ obtained from the best fit (Figure 4.4.3). The data indicate that the log-law describes the velocity well in the region $20 \leq y^+ \leq 300$ in this case. At low R_θ, the use of the log-law to estimate wall shear stress is tenuous, since the log-region at low R_θ is very narrow, or even non existent (Spalart,1988; Ching et al.,1995a).

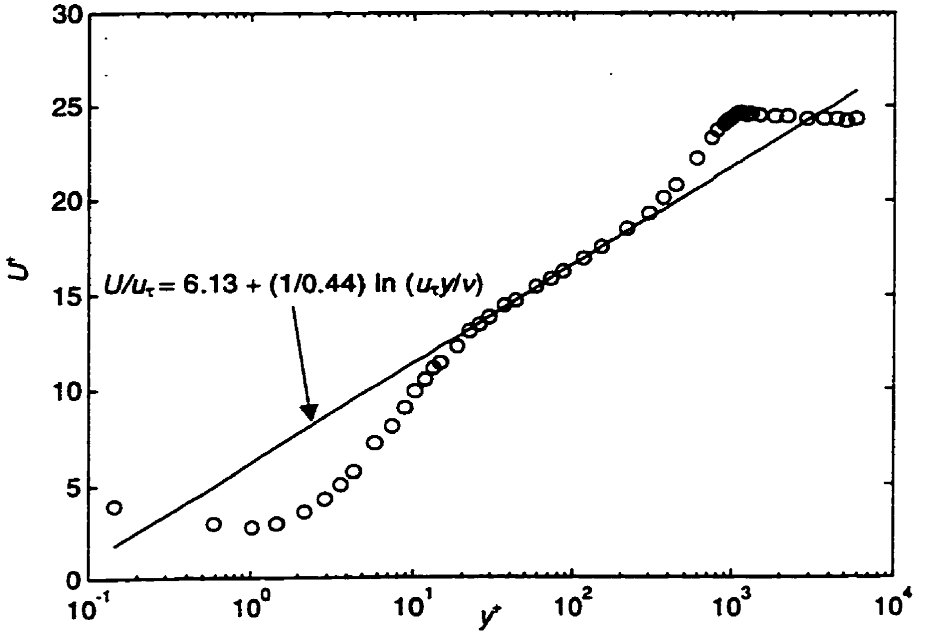

Figure 4.4.3 Clauser chart method for determining u_τ presented in a U^+ - y^+ plane. ○ - smooth wall data at $R_\theta = 2470$.

The wall shear stress can also be calculated from the mean velocity gradient at the wall.

$$\tau_w = \mu \frac{\partial U}{\partial y} \Big|_{y=0} \tag{4.24}$$

This method needs accurate data very close to the wall i.e. $y^+ \lesssim 3.0$. Due to the effect of heat conduction from the wire to the wall, measurements in this region are very difficult with hot-wire anemometry. However, at the lower R_θ, at least four to five data points can be obtained in the range $1 \leq y^+ \leq 3$ using a single-normal hot-wire. Djenidi and Antonia (1993), using LDA, showed that u_τ can be determined using this method to an accuracy of order ± 3% at low Reynolds numbers ($R_\theta \leq 1320$).

There are two steps to determine τ_w based on this method. First, the velocity data is plotted and a least squares straight line is obtained for the data close to the wall as shown in Figure 4.4.4. From this, a first approximation for u_τ can be calculated. From the calculated u_τ, the U and y values are converted into normalized values, U^+ and y^+, respectively, and a new linear fit is applied to the data in the region $y^+ \leq 3$ (Figure 4.4.5). The new value of u_τ is considered valid only if the new linear fit describes the data well in the region $y^+ \leq 3$.

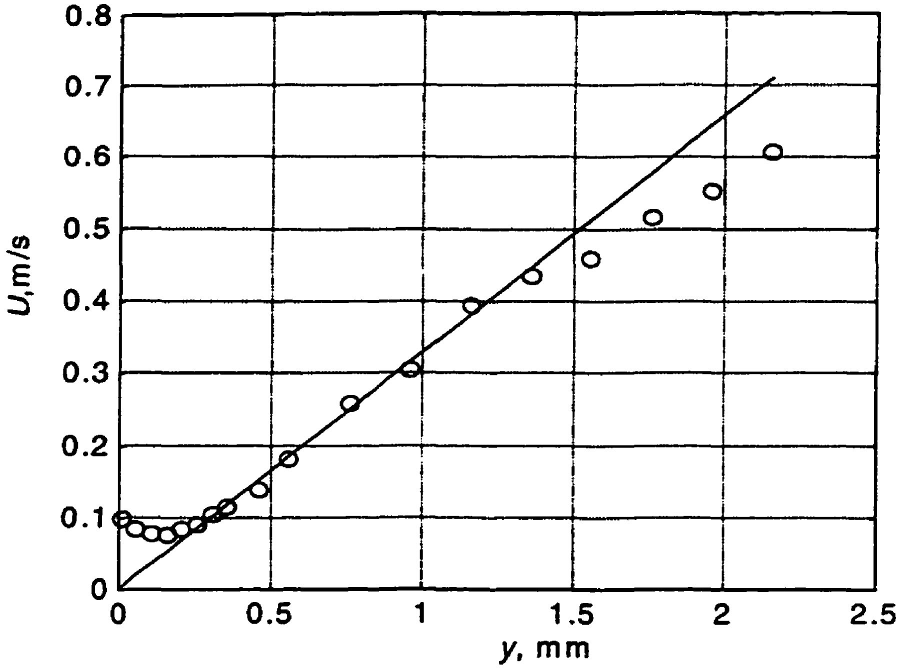

Figure 4.4.4 Mean velocity in the near-wall region. o, current data, U_∞ = 1.40 m/s.

A fourth method to determine the wall shear stress is by using a Preston tube. This method was introduced by Preston (1954), who suggested a non-dimensional relationship as follows:

$$\frac{\overline{\Delta p}}{\rho}\frac{d^2}{\nu^2} = F\left[\frac{d^2\overline{\tau_w}}{\rho\nu^2}\right] \quad (4.25)$$

where Δp is the pressure difference between the total pressure at the wall (which is sensed by the Preston tube) and the static pressure (which is sensed by the Pitot-static tube).

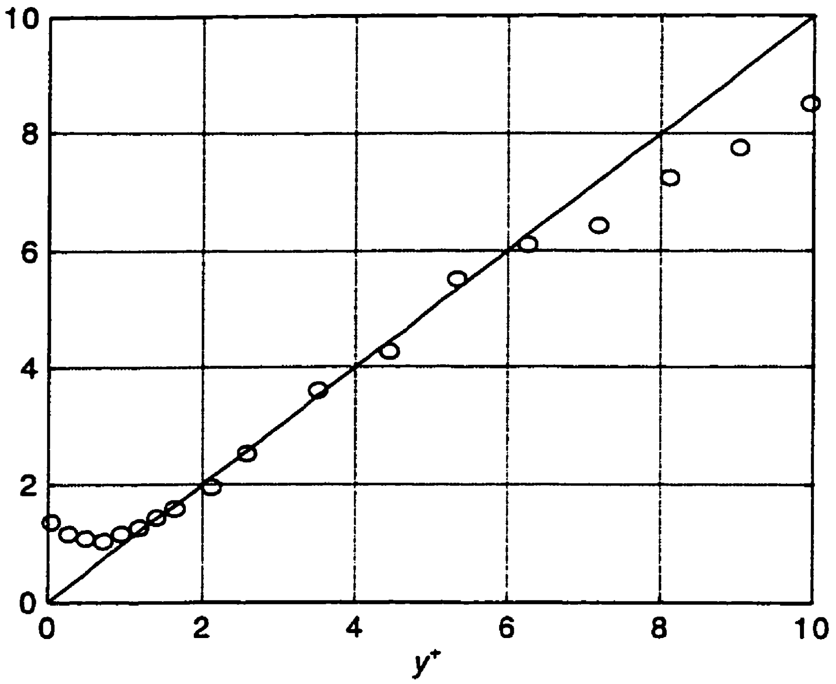

Figure 4.4.5 Normalized mean velocity in the near-wall region. o, current data, U_∞ = 1.40 m/s; —, $U^+ = y^+$.

The relationship F in Eq. (4.25) was proposed by Patel et.al. (1965). This equation is valid in three Reynolds number ranges:

A) $y^* = 0.50x^* + 0.037$, **(4.26a)**
$y^* < 1.5$, and $u_\tau d/2\nu < 5.6$

B) $y^* = 0.8287 - 0.1381x^* + 0.1437x^{*2} - 0.0060x^{*3}$, **(4.26b)**
$1.5 < y^* < 3.5$ and $5.6 < u_\tau d/2\nu < 55$

C) $x^* = y^* + 2\log_{10}(1.95\,y^* + 4.10)$ **(4.26c)**
$3.5 < y^* < 5.3$ and $55 < u_\tau d/2\nu < 800$

where $x^* = \log_{10}\left(\frac{\Delta p d^2}{4\rho\nu^2}\right)$ and $y^* = \log_{10}\left(\frac{\tau_w d^2}{4\rho\nu^2}\right)$, respectively.

Bechert (1995), proposed a general Preston tube calibration formula

$$\tau^+ = [28.44(\Delta p^+)^2 + 6.61.10^{-6}(\Delta p^+)^{3.5}]^{1/4} \quad \textbf{(4.27)}$$

where τ^+ and Δp^+ are defined as $\tau_w d^2/(\rho\nu^2)$ and $\Delta p d^2/(\rho\nu^2)$, respectively. This formula is in excellent agreement with data obtained by Head and Ram (1971). A comparison of u_τ calculated using the calibrations of Patel and Bechert are presented in Table IV.1, and the corresponding graphical presentation is shown in Figure 4.4.6. The maximum difference in u_τ obtained from the two calibrations is about 2%. Bechert's formula is much simpler to use and, therefore, is used here whenever a Preston tube calibration formula is needed.

4.5 Turbulent Kinetic Energy Dissipation Rate (ε)

The rate of turbulent kinetic energy dissipation can be calculated with Eq. **(2.9)** by assuming isotropic turbulence.

$$\varepsilon = 15\nu\overline{(\partial u/\partial x)^2} \quad \textbf{(2.9)}$$

Using Taylor's frozen hypothesis, $\partial u/\partial x$ can be calculated from $\partial u/\partial t$. The trace of $\partial u/\partial t$ can be deduced from the streamwise velocity trace by using a finite difference scheme.

Table IV.1 Comparison of u_τ and C_f based on Patel's and Bechert's calibration formulas for various Δp^+.

Δp^+	u_τ (m/s)		C_f (x 100)	
	Patel (Eq. 4.26)	Bechert (Eq.4.27)	Patel (Based on Eq. (4.26))	Bechert (Based on Eq. (4.27))
35029.35	0.2377	0.2334	0.308763	0.297667
35322.82	0.2384	0.2341	0.310611	0.299478
36637.60	0.2416	0.2373	0.318856	0.307574
37514.67	0.2436	0.2393	0.324324	0.312962
39122.09	0.2473	0.2431	0.334282	0.322807
39505.28	0.2482	0.2439	0.336644	0.325149
40010.06	0.2494	0.2451	0.339749	0.328231
40238.97	0.2499	0.2456	0.341155	0.329628
40326.18	0.2501	0.2458	0.341690	0.330160
40559.28	0.2506	0.2463	0.343119	0.331581
40863.66	0.2513	0.2470	0.344983	0.333436
41410.36	0.2525	0.2483	0.348324	0.336764
41547.04	0.2528	0.2486	0.349158	0.337596
41770.08	0.2533	0.2491	0.350518	0.338952
42446.75	0.2548	0.2506	0.354635	0.343064
42461.01	0.2548	0.2506	0.354722	0.343151
43319.64	0.2567	0.2525	0.359928	0.348360

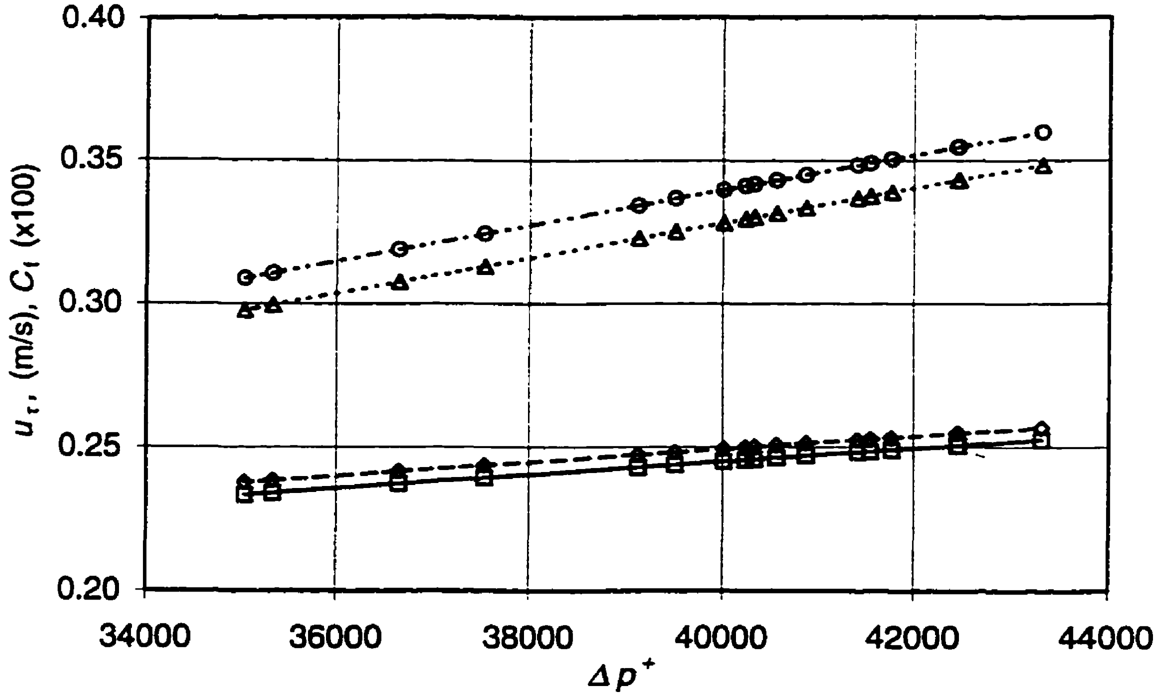

Figure 4.4.6 Comparison of u_τ and C_f based on Bechert's and Patel's calibration formulas for various Δp^+. Symbols: □, u_τ (Eq. 4.27); ◇, u_τ (Eq. 4.26); Δ, C_f (based on Eq. 4.27); ○, C_f (based on Eq. 4.26). Lines are plotted only for convenience.

Consider a fluctuating velocity trace shown in Figure 4.5.1. This trace is taken at $y/\delta = 0.0274$, at $R_\theta = 830$. Figure 4.5.2 and 4.5.3 show the corresponding $\partial u/\partial t$ and $\partial u/\partial x$ traces of the velocity trace. For the trace shown, the corresponding values of U and $\overline{(\partial u/\partial x)^2}$ are 0.67 m/s and 732.5 $\sec^{-2}$, respectively. If the kinematic viscosity of air is 1.55 x 10^{-5} m^2/s, then the rate of turbulent kinetic energy dissipation, ε, is 0.1703 m^2/s^3. Once the rate of turbulent kinetic energy dissipation is determined, the Kolmogorov length, time, velocity, and frequency scales can be calculated with Eq. (2.11), (2.12), (2.14), and (2.13), respectively. The numerical values obtained from those equations for the data shown in Figure 4.5.1 are 0.38 mm, 9.5 msec., 0.0403 m/s, and 277.3 Hz, for the Kolmogorov length, time, velocity, and frequency scales, respectively.

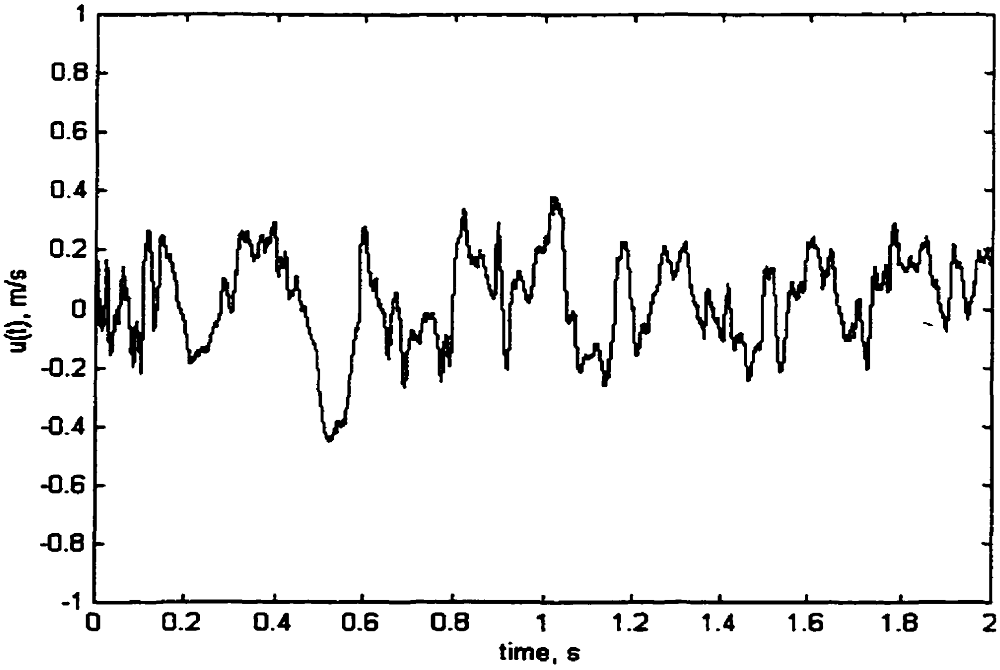

Figure 4.5.1 Streamwise velocity fluctuation. $U_\infty = 1.40$ m/s, $y/\delta = 0.0274$, $\delta = 95$ mm. Data is for the smooth-wall and is obtained using a SN-wire.

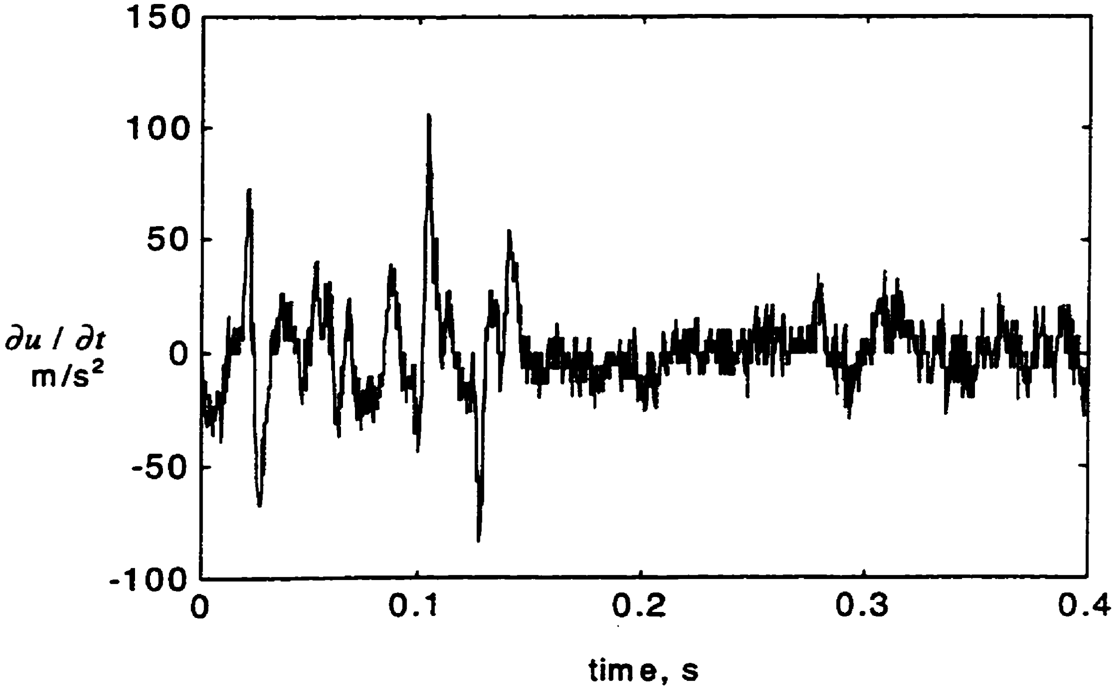

Figure 4.5.2 Temporal derivative of streamwise velocity fluctuation shown in Figure 4.5.1. Only the first one-fifth points are included for clarity.

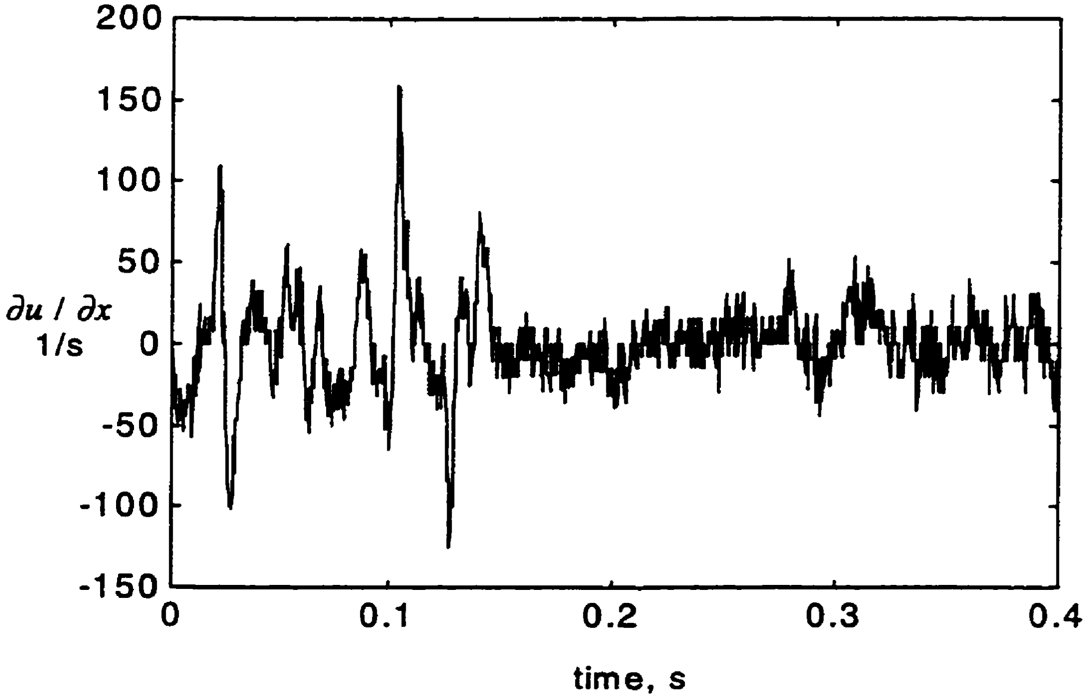

Figure 4.5.3 Spatial derivative of streamwise velocity fluctuation shown in Figure 4.5.1. Only the first one-fifth points are included for clarity.

Chapter 5

Experimental Results and Discussion

The development of a turbulent boundary layer downstream of a transverse square cavity has been investigated. Experiments were performed at freestream velocities of 2.0 m/s and 5.5 m/s, corresponding to R_θ in the range 900 to 1680 at the lower velocity, and 2450 to 4030 at the higher velocity. The experimental conditions and flow parameters are presented on Table V.1. At both freestream conditions, the pressure variation along the test section is negligibly small, ($[(p - p_0)/0.5\rho(U_\infty)^2] < 4\%$), where p_0 is the reference static pressure at $x/w = 1$ (Figure 5.1). Results are presented for the development of the wall shear stress, mean velocity profile, and streamwise turbulence intensity profile. The wake parameter and power spectra are also analyzed. The rate of turbulent kinetic energy dissipation and growth of the internal layer downstream of the cavity are also presented. The results for the grooved-wall (the smooth-wall with a single transverse square cavity) are compared with corresponding experimental results over a smooth wall, and the smooth wall DNS data of Spalart (1988). At the lower R_θ range, u_τ is deduced from a power-law approximation for the mean velocity profile, while at the higher R_θ range, it is deduced from the Clauser-chart method and from Preston tube measurements.

5.1 Friction Velocity (u_τ)

An accurate estimate of τ_w (or u_τ) is important to predict the skin friction drag associated with boundary layers. Four methods were employed to estimate wall shear stress: gradient of the mean velocity at the wall, Preston tube measurements, a power law approximation of the mean velocity profile, and Clauser-chart method.

Table V.1 Experimental conditions and flow parameters

	R_w	
	645	1774
U_∞ (m/s)	2.0	5.5
R_θ	900 - 1680	2450 - 4030
d/δ_1	0.066	0.072
d/w	1.0	1.0

Note: δ_1 is the boundary layer thickness at $x/w = 1$.

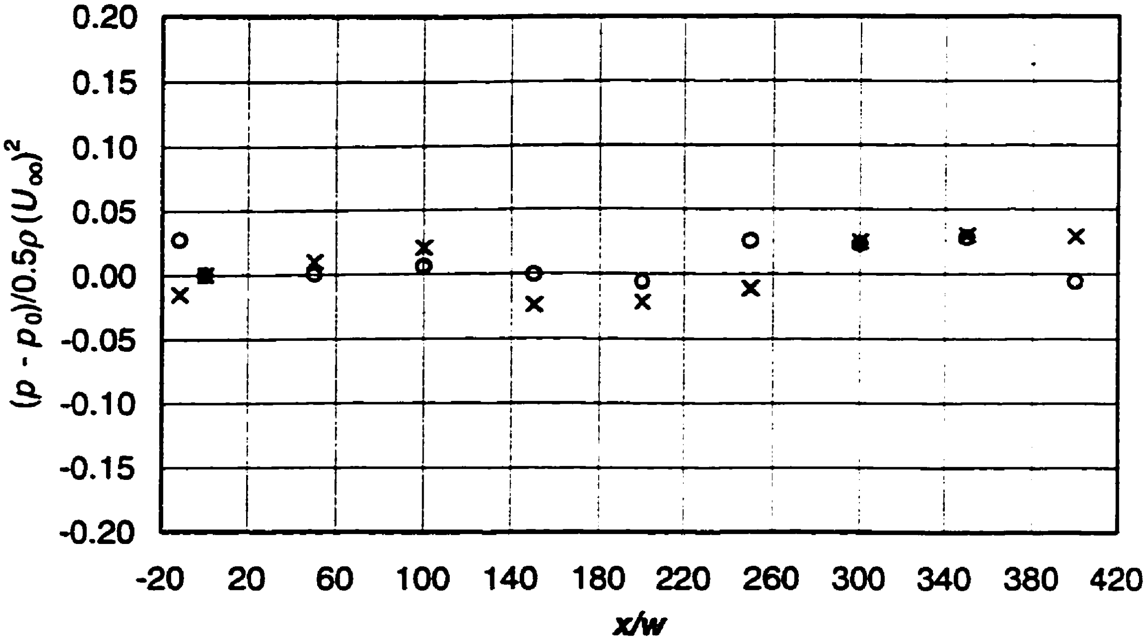

Figure 5.1 Static pressure distribution along the centerline of the test section. Symbols: o, $U_\infty \approx 6$ m/s; x, $U_\infty \approx 3$ m/s.

The wall shear stress can be estimated from the mean velocity gradient in the near wall region, however, there are several difficulties associated with this method. First, the use of hot-wires to measure velocity very close to the wall results in the wall-conduction problem. In the region very close to the wall ($y^+ \leq 3$), where the mean velocity profile is linear, heat transfer from the wire to the wall produces a significant error to the anemometer output. Secondly, relatively thick boundary layers are necessary to obtain the required spatial resolution to obtain accurate results from this method. Though this method was attempted in the the current study, the results for τ_w were not satisfactory because of these two problems.

At the higher R_w, τ_w was also estimated using a Preston tube. This method was not feasible at the lower Reynolds number because the differential pressure transducer available was out of range. For this R_w, the dynamic pressure ratio ($\equiv 0.5\ \rho U^2/0.5\rho U_\infty^2$) near the wall is of the same order as the minimum reading of the differential pressure transducer. The results from the Preston-tube measurements and Clauser-chart method at $R_w = 1774$ are within ± 4% (Figure 5.1.1). For $x/w \lesssim 30$, ($R_\theta \lesssim 2760$), the Clauser-chart gives a lower C_f than that obtained from the Preston tube. On the other hand, for $x/w \gtrsim 30$ ($R_\theta \gtrsim 2760$), the Clauser-chart gives a higher C_f than that obtained from the Preston tube. The reason for this is not clear at this point. The u_τ estimated from the Clauser-chart method is used as the normalizing parameter for the higher R_θ results.

The smooth-wall U^+ profiles at the lower R_θ are compared with the power-law distributions (only two profiles are shown for clarity) in Figure 5.1.2. There is a good collapse of the profiles, and the power-law is in good agreement with the experimental data in the outer region. In this figure, U^+ and y^+ are normalized using u_τ deduced from the power-law. The present results support the incomplete similarity hypothesis of Barenblatt (1993), which states that at low Reynolds numbers, the friction velocity can be deduced from the power-law distribution in the overlap region. In the inner region ($y^+ \lesssim 30$), the power law distribution is not valid, and cannot be used to describe the mean velocity profiles. The experimental data are also in good agreement with DNS data, and the small differences in the outer region could be attributed to the difference in Reynolds numbers.

At low Reynolds numbers, the Clauser chart method to estimate u_τ may not be appropriate. Both DNS (Spalart, 1988) and experimental (Ching et. al, 1995a) data indicate that the log region is very narrow at low R_θ. This can be shown by plotting y^+dU^+/dy^+ versus log y^+ (Spalart, 1988; Ching et al.1995a). The log region is represented by a valley (local minimum) of constant value on such a plot. At low R_θ, this valley is very narrow or even non-existent (Spalart, 1988), and the use of the log-law (Clauser-chart method) to estimate u_τ can be erroneous. Nevertheless, the log-law of the form

$$U^+ = (1/0.41)\, ln\, (y^+) + 5.0 \tag{5.1}$$

is shown in Figure 5.1.2. The log-law fits the data well only in the range $30 \le y^+ \le 100$.

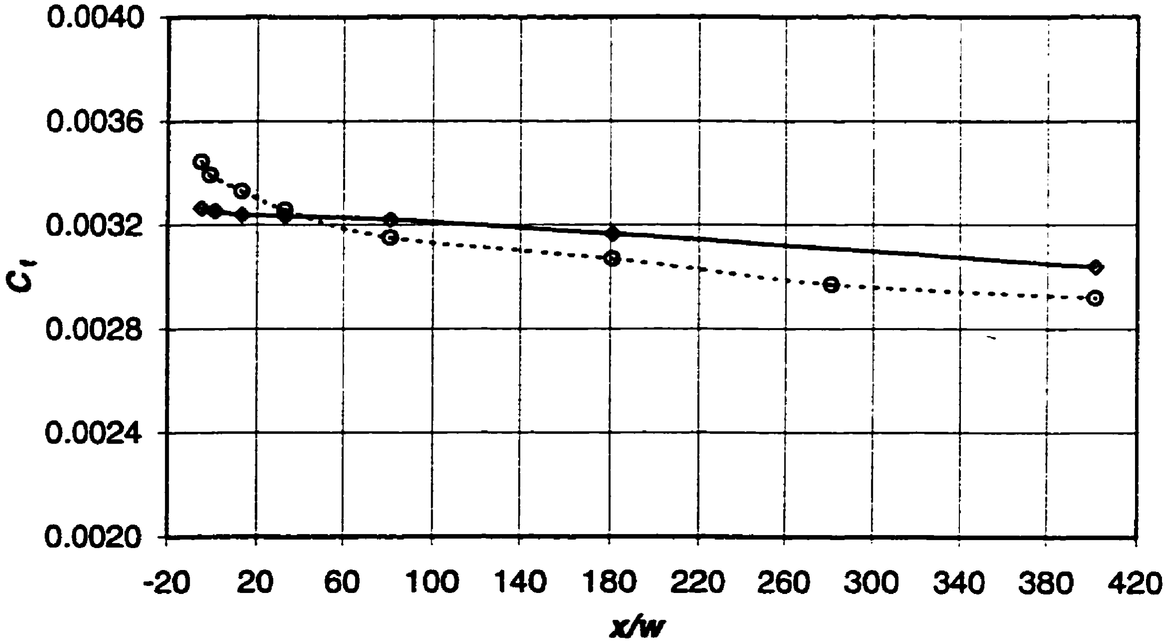

Fig. 5.1.1 Skin friction coefficient distribution estimated from two methods: Preston-tube measurements (o), and Clauser-chart method (◇). Lines are shown only for convenience.

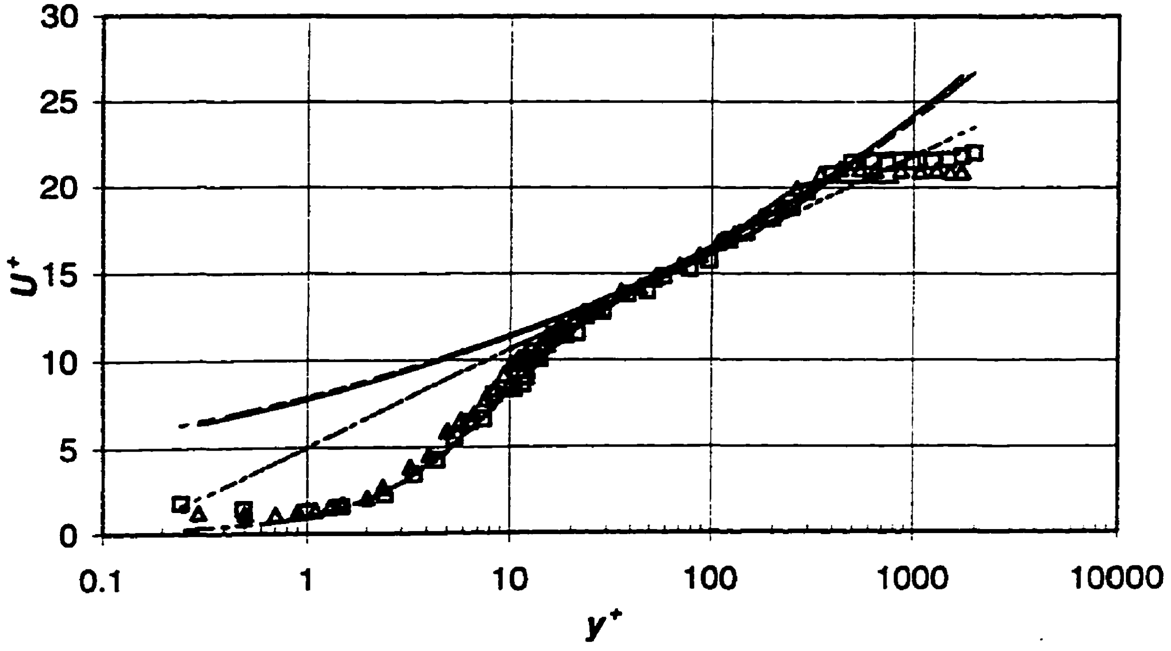

Figure 5.1.2 Power-law and log-law fits to mean velocity profiles in the overlap region for a smooth-wall boundary layer.

Experiment : △, $R_\theta = 830$; □, $R_\theta = 1250$.
Power-law fit : ——, $R_\theta = 830$; - - -, $R_\theta = 1250$.
Log-law fit : ...., $R_\theta = 830$; 1250.
DNS (Spalart, 1988) : - - —— -, $R_\theta = 670$; -——-——-, $R_\theta = 1410$

U^+ profiles are compared with the power-law and the log-law at R_w = 1774 in Figure 5.1.3. Only two profiles are shown in the figure for clarity. There is a good collapse of the profiles in the region $y^+ \leq 1000$. Unlike in the case for the lower R_w, the power-law fit, especially in the wake region, is poor. In this Reynolds number range (R_θ > 2000), it is difficult to obtain a good fit to the experimental data using a power-law approximation. The power-law fits the data well only in the range $30 \leq y^+ \leq 300$. This is in agreement with the pipe flow data of Zagarola et al. (1997), in which the power-law fit the data well only in the range $50 \leq y^+ \leq 500$.

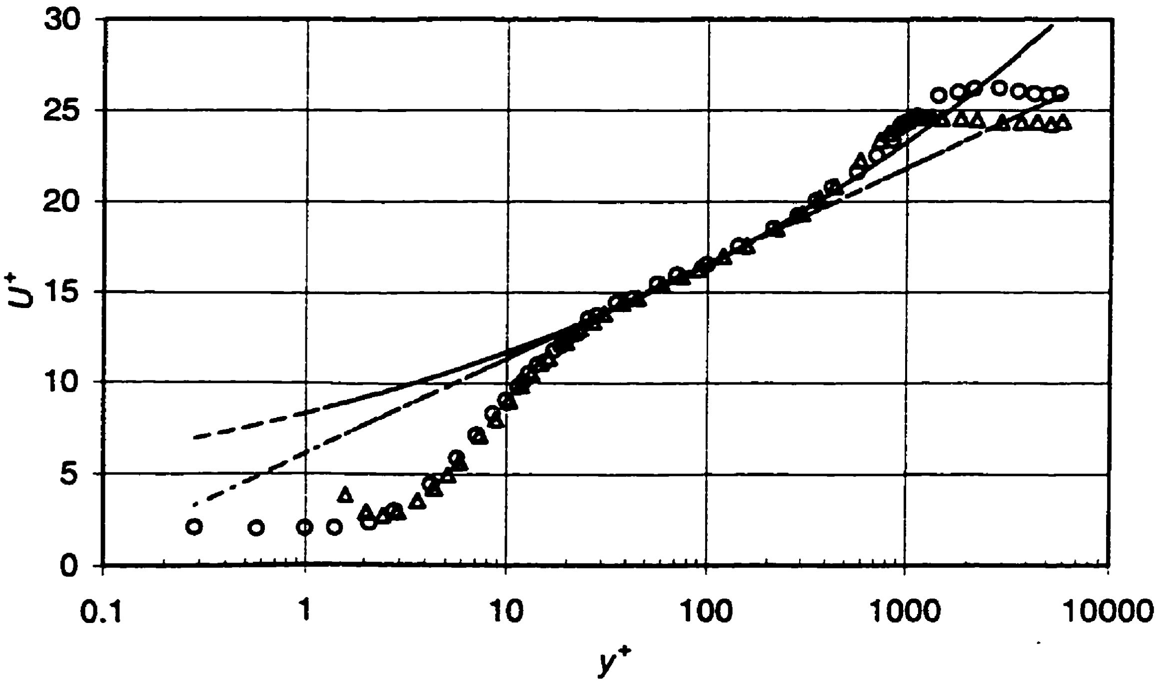

Figure 5.1.3 Power-law and log-law fits to mean velocity profiles in the overlap region for a smooth-wall boundary layer.

Experiment : Δ, $R_\theta = 2450$; ○, $R_\theta = 4230$.
Power-law fit : ——, $R_\theta = 2450$; — — — — —, $R_\theta = 4230$;
Log-law : - - - -, $R_\theta = 2450$; - - —— - - ——, $R_\theta = 4230$;

The log-law in this instance (Figure 5.1.3) describes the mean velocity profiles well in the region $30 \le y^+ \le 300$. The log-law fit is similar to that of Zagarola et al. (1997), who suggested values of 0.436 and 6.13 for the Karman constant and the intercept, respectively. In the current investigation, values of 0.44 and 6.13 were obtained for a log-law expression of the form

$$U^+ = (1/0.44)\, ln\, (y^+) + 6.13 \qquad \textbf{(5.2)}$$

The deviation of the mean velocity at the outer edge of the boundary layer from the log-law can be expressed in terms of the law of the wake (Coles, 1956).

In the present study, at the lower Reynolds number ($R_\theta \leq 2000$, or $R_w = 645$), the power law method is used to estimate u_τ. On the other hand, at the higher Reynolds number ($R_\theta \geq 2500$, or $R_w = 1774$), the friction velocity is estimated using the Clauser-chart method. The results of u_τ from these two methods are used to normalize the mean velocity and turbulence intensity profiles for the low and high Reynolds numbers, respectively.

5.2 Skin Friction Coefficient (C_f)

The streamwise distributions of the skin friction coefficient at $R_w = 645$ and 1774 are presented in Figures 5.2.1 and 5.2.2, respectively. Results are shown for both the grooved and smooth wall. The effect of the cavity on C_f is much more pronounced at the higher R_w. At the lower R_w, there is a small decrease in C_f in the vicinity of the groove ($\approx$ 1.3%), where the groove location is at $x/w = 0$. The relaxation of C_f back to the smooth-wall value ($C_{f,0}$) appears to be complete at $x/w \approx 280$. The relaxation is preceded by an increase in C_f in the region $60 \lesssim x/w \lesssim 260$, however, the difference between C_f and $C_{f,0}$ is about 1%, and is within the experimental uncertainty.

At the higher R_w, a small sharp rise in C_f immediately downstream of the cavity is discernible. The sharp rise in C_f can be attributed to the local intense favorable pressure gradient that emanates from the downstream edge of the cavity (Pearson et al., 1997). The sharp rise is followed by a decrease in C_f below the smooth-wall value in the range $30 \lesssim x/w \lesssim 110$. The decrease in C_f is then followed by an oscillatory relaxation back to $C_{f,0}$. At $x/w \gtrsim 180$, C_f is essentially the same as $C_{f,0}$. These results are similar to the results of Pearson et al.(1997) and Elavarasan et al. (1996), however, the sharp rise in C_f of the current study is not as intense as in the study of Pearson et al. This difference may be attributed to the difference in d/δ_1 in the two studies. In the current study, $d/\delta_1 = 0.072$ at $R_w = 1774$, while in the study of Pearson et al., $d/\delta_1 = 0.17$ at $R_w = 2000$.

The C_f distribution estimated from Preston tube measurements is shown in Figure 5.2.3. The results are at a higher Reynolds number ($R_w = 1935$). The overshoot and undershoot in C_f of the previous plot is also present in this case. However, it occurs over a much smaller streamwise distance. This is probably due to the higher R_w of the Preston tube measurements. It is very likely that the relaxation after the perturbation occurs faster at higher Reynolds number. At the higher R_w, the turbulent energy content is much higher than that at the lower R_w, and therefore the relaxation is likely to occur more quickly. For clarity, the C_f in the vicinity of the groove is shown using a larger scale for the abscissa in Figure 5.2.4.

Figure 5.2.5 and 5.2.6 show the distribution of $C_f/C_{f,0}$ as a function of x/w at $R_w =$ 645 and 1774, respectively. These figures highlight the oscillatory behaviour of $C_f/C_{f,0}$ around the groove, especially at the higher R_w. An estimate of the drag can be obtained by integrating C_f along the streamwise direction. At $R_w = 645$, the groove results in an increase in friction drag of about 1.0% over the smooth-wall value. At the higher Reynolds number, the drag on the grooved-wall is almost the same as that on the smooth-wall. This is because the increase in C_f immediately downstream of the groove is offset by the decrease in the range $40 \leq x/w \leq 100$.

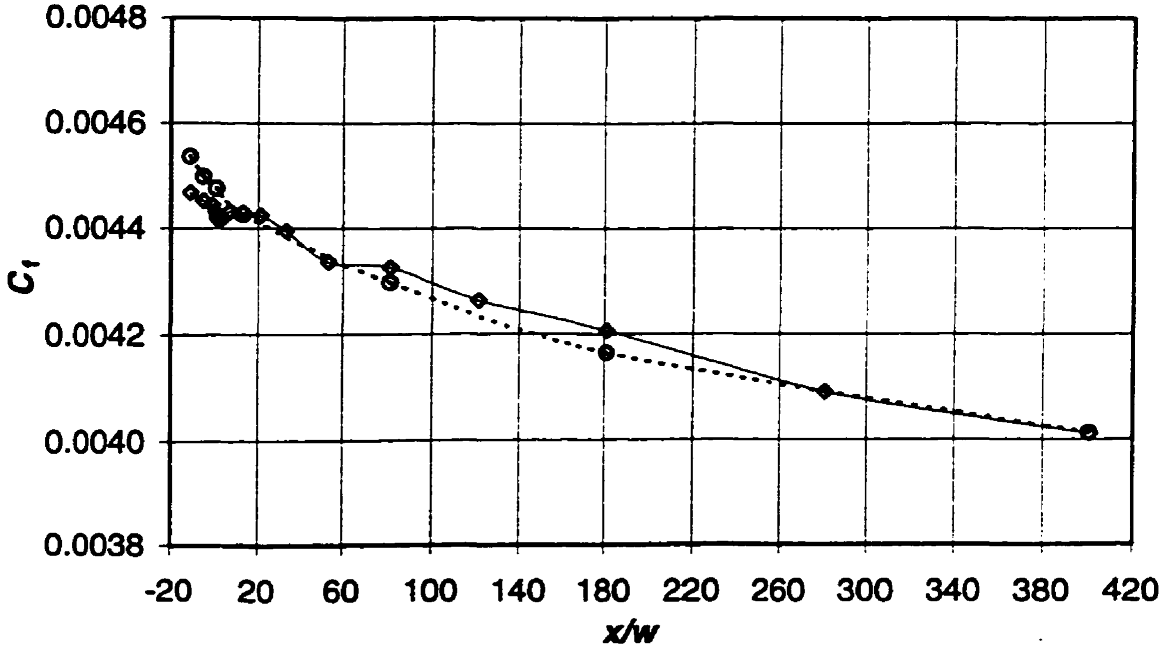

Figure 5.2.1 Development of skin friction coefficient in the streamwise direction at $R_w = 645$. Symbols: ○, smooth-wall; ◇, grooved-wall. The lines are plotted only for convenience.

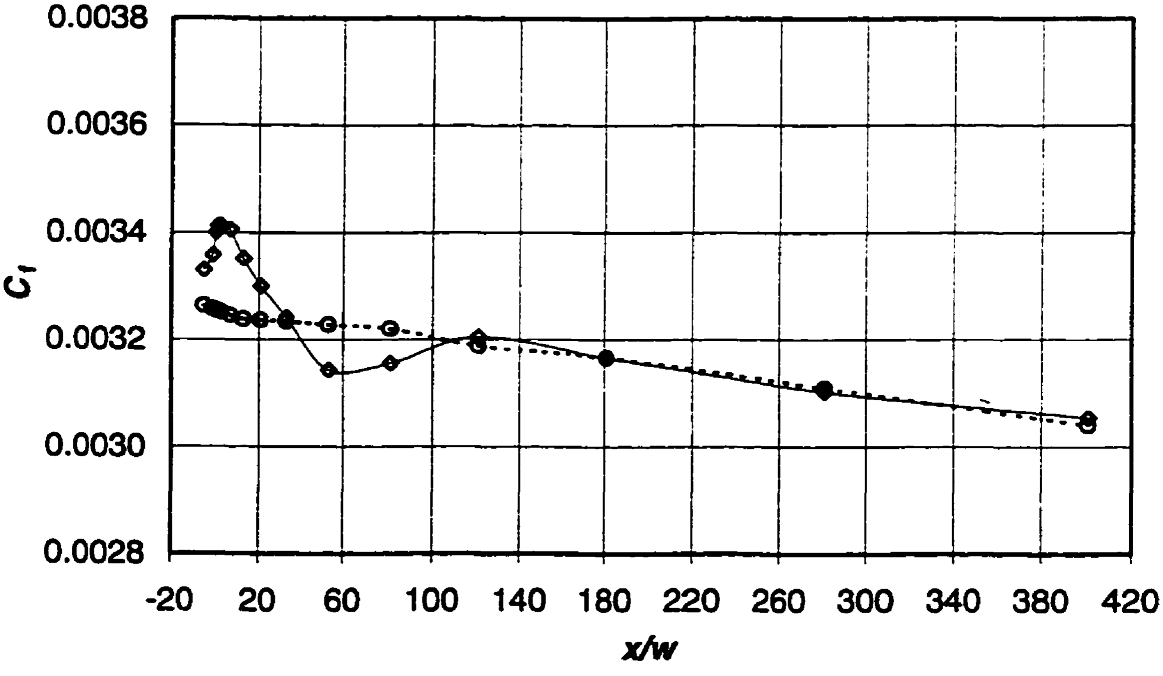

Figure 5.2.2 Development of skin friction coefficient in the streamwise direction at $R_w = 1774$. Symbols: ○, smooth-wall; ◇, grooved-wall. The lines are plotted only for convenience.

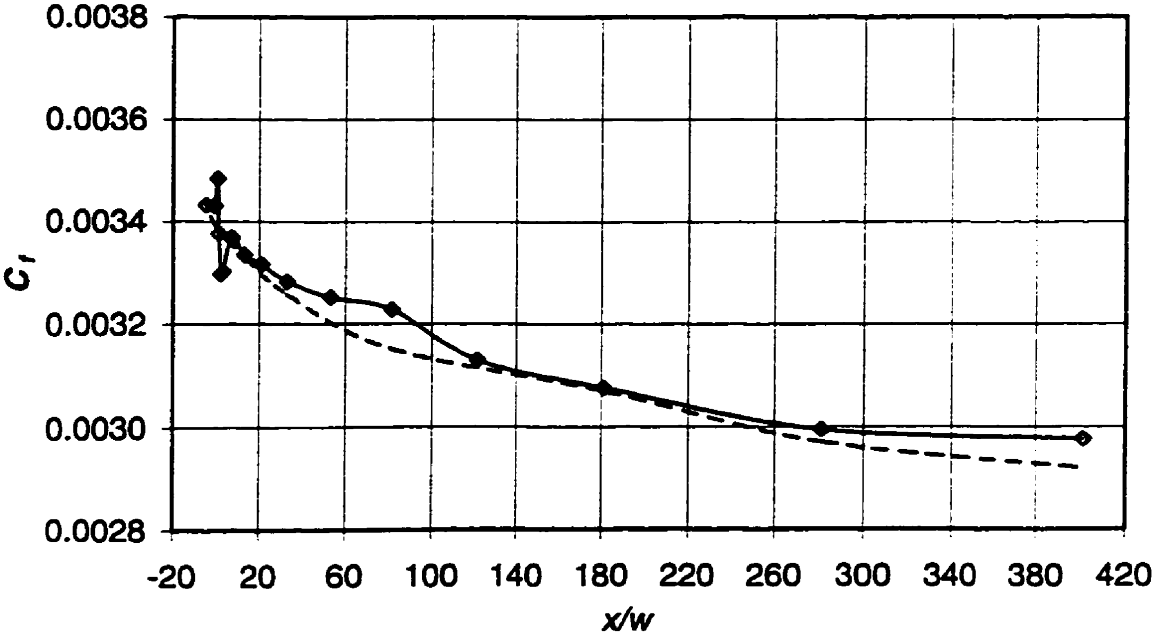

Figure 5.2.3 Development of skin friction coefficient in the streamwise direction obtained from Preston tube measurement at R_w = 1935. Symbols: - - - - -, smooth-wall; ◇, grooved-wall. Line is plotted only for convenience.

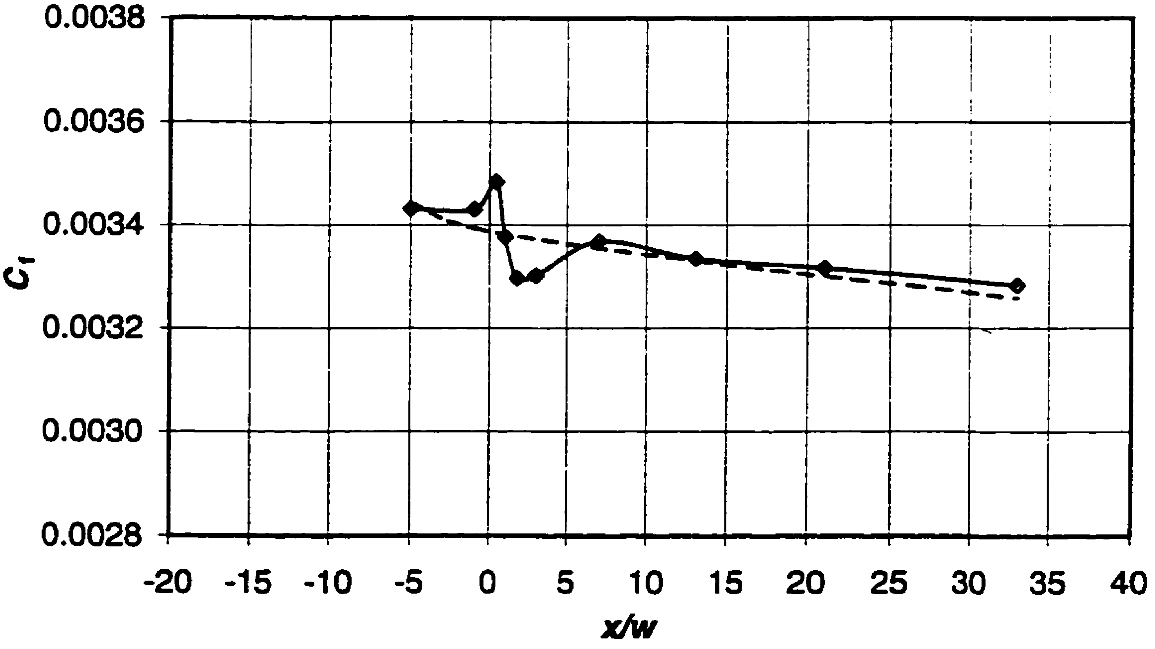

Figure 5.2.4 Development of skin friction coefficient in the streamwise direction as shown in Figure 5.2.3, but it is plotted in a different x-scale.

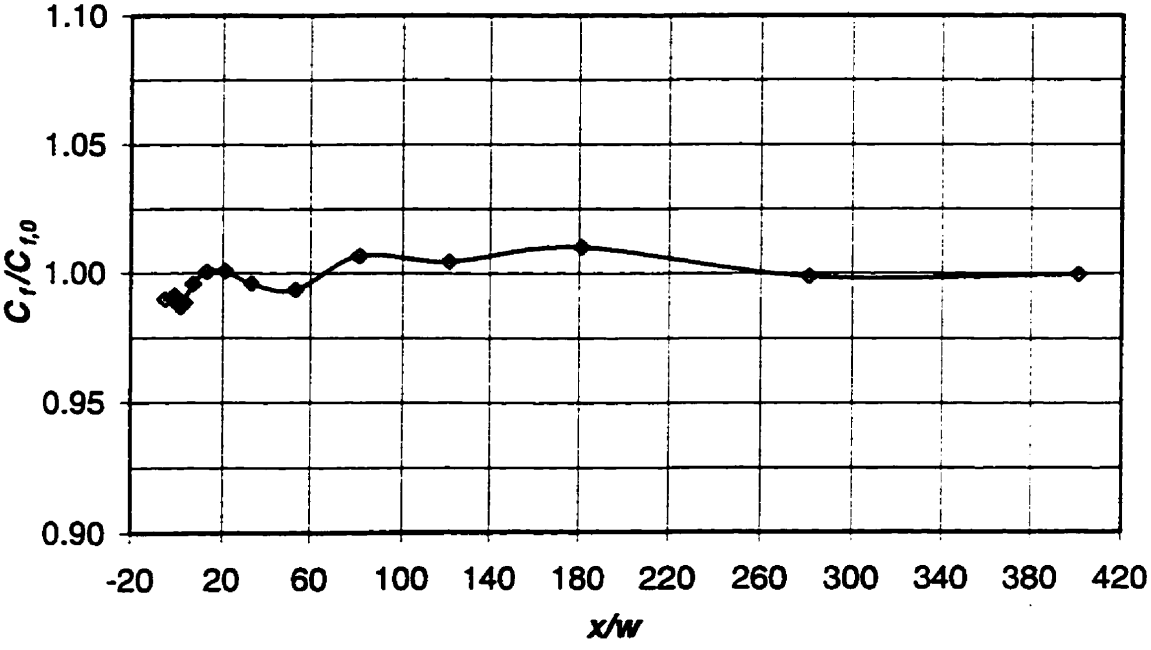

Figure 5.2.5 Development of $C_f/C_{f,0}$ in the streamwise direction at R_w = 645. The line is plotted only for convenience.

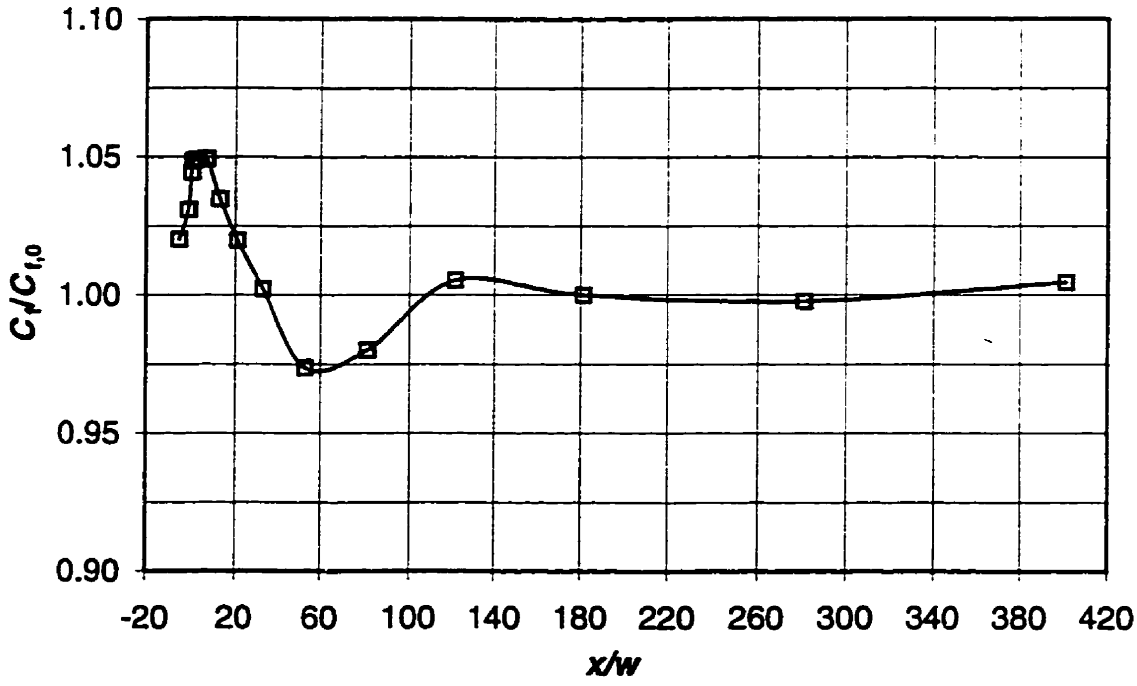

Figure 5.2.6 Development of $C_f/C_{f,0}$ in the streamwise direction at R_w = 1774. The line is plotted only for convenience.

It is difficult to make any conclusions on the drag since the changes are very small ($\lesssim$ 1%), and well within the experimental uncertainty. Nevertheless, the results provide some insight into the behaviour of C_f due to a transverse square cavity. There is a local reduction in C_f at both R_ws in the immediate vicinity of the cavity. The magnitude of this reduction is significantly affected by the Reynolds number. It is also obvious that d/δ_1 plays an important role in the relaxation of C_f downstream of the cavity. These results indicate that if a number of transverse square cavities are spaced optimally in the streamwise direction, a reduction in total skin friction drag may be possible. Ching and Parsons (1998) showed that the total surface drag is a function of Reynolds number, s/w, and cavity size. To obtain a total surface drag reduction, the area under the overshoot must be reduced, and the area under the undershoot increased. They suggested that the next cavity should be located at the end of the undershoot to eliminate the increase due to the oscillatory relaxation of C_f. For the current study, $s/w = 100$ at $R_w = 1774$ according to their argument. This is much higher than the values obtained by Pearson et al. (1997) and Elavarasan et al. (1996), however, it must be noted that d/δ_1 in this case is much lower than in the latter two studies.

5.3 Mean Velocity Profiles

5.3.1 Smooth-Wall Results

The wall normalized mean velocity profiles over the smooth-wall at $R_w = 645$ are presented in Figure 5.3.1. The velocity is normalized using u_τ obtained from the power-law method. The experimental profiles ($830 \leq R_\theta \leq 1950$) are in good agreement with the DNS data. Very close to the wall, the experimental data deviates from the DNS data due to the wall conduction effect, and uncertainty of the spatial location of the probe (Djenidi et al. 1997). In the wake region, a small deviation of the experimental data from the DNS data is discernible due to the difference in the Reynolds number.

The U^+ profiles at the higher Reynolds number ($R_w = 1774$) are presented in Figure 5.3.2. In this case, the velocity is normalized using u_τ obtained from the Clauser-chart method. The profiles agree well with the DNS profile ($R_\theta = 1410$) up to $y^+ \leq 500$. For $y^+ \geq 500$, the deviation of the experimental data from the DNS data is due to the difference in Reynolds number, since the experimental profiles are at $R_\theta \approx 3000$, while the DNS profile is at $R_\theta = 1410$.

5.3.2 Grooved-Wall Results

The U^+ profiles on the grooved-wall at $R_w = 645$ are presented in Figure 5.3.3. To allow a better comparison, the profiles in the vicinity of the cavity (groove), are shown superimposed in Figure 5.3.5. There is a good collapse of the profiles, and the data is in good agreement with the DNS profile. The effect of the cavity is not discernible in the inner and overlap regions. A small deviation from the DNS profile in the wake region is discernible, and this is due to the difference in R_θ. At $R_w = 645$, the effect of the cavity on the mean velocity is not significant. The ratio d/δ_1 is likely to play an important role on the effect of the cavity on the turbulent boundary layer (Haugen and Dhanak, 1966). For the present study, d/δ_1 is approximately 0.072, and is probably too small for it to have any significant effect on the mean velocity. Pearson et al. (1997), Elavarasan et al (1996) and Choi and Fujisawa (1993) had $d/\delta_1 = 0.17$, 0.125 and 0.4, respectively. In those three studies, there was a significant effect of the cavity on the mean velocity.

The U^+ profiles for the grooved-wall at $R_w = 1774$ show no significant difference from the profiles on the smooth-wall (Figure 5.3.4). Similar to the smooth-wall profiles, there is good agreement with the DNS data. The differences in the outer region are due to the different Reynolds numbers.

The U^+ profiles over the grooved-wall in the vicinity of the cavity at $R_w = 1774$ are shown superimposed in Figure 5.3.6. There is a small influence of the cavity on the mean velocity in the overlap region. However, there is, in general, good collapse of the profiles in the range $y^+ \leq 1000$.

5.3.3 Comparison between Smooth- and Grooved-Wall U^+ Profiles

Due to the very small changes in C_f compared to the smooth-wall, the mean velocity profiles for the grooved-wall are, in general, similar to the smooth wall profiles, however, small deviations in the profiles can be discerned. For example, there is a slight upward shift of the mean velocity profile from the smooth-wall profile (Figure 5.3.7) at $x/w = 1$. A change in the wall shear stress will result in a shift of the U^+ profile. An upward shift of the profile indicates a reduction in τ_w, while a downward shift indicates an increase in τ_w. For the present grooved-wall, the maximum deviation of the wall shear stress from the smooth-wall value is less than 1% at $R_w = 645$ (Figure 5.2.5), and hence the shift would be very small.

The U^+ profiles for the smooth- and grooved-wall at x/w locations corresponding to the maximum and minimum $C_f/C_{f,0}$ at $R_w = 1774$ are compared in Figures 5.3.8 and 5.3.9, respectively. Despite the change in u_τ for the grooved-wall, the U^+ profiles are indistinguishable.

The above results are different from the results of Pearson et al. (1997), and Elavarasan et al. (1996). In those two studies, there was a significant shift in the U^+ profiles due to the presence of the cavity. The reason for the difference is likely to be due to the large difference in the magnitude of the overshoot and undershoot in C_f. In the current study, the maximum in $C_f/C_{f,0}$ is about 1.05, while the minimum is about 0.975. On the other hand, the maximum in $C_f/C_{f,0}$ obtained by Pearson et al. and Elavarasan et al. are about 3.0, and 1.5, respectively. The minimum in $C_f/C_{f,0}$ in the latter two studies are about 0.5. This illustrates the significant effect of d/δ_1 on $C_f/C_{f,0}$.

At the higher R_w of the present study, d/δ_1 is about 0.072. This groove size is probably too small to significantly affect the boundary layer. In order to significantly affect the boundary layer, it can be conjectured that d/δ_1 must be larger than 0.1. In the studies of Pearson et al. and Elavarasan et al., $d/\delta_1 = 0.17$, and 0.125, respectively.

To ensure that the effect of the groove on the mean velocity is insignificant, the mean velocity is compared using outer variable (U_∞ and δ) normalization (Figure 5.3.10). The smooth- and grooved-wall profiles are shown at the x/w location where $C_f/C_{f,0}$ is a maximum. The profiles collapse over the entire y/δ range, and implies that mean velocity is undisturbed by the presence of the groove.

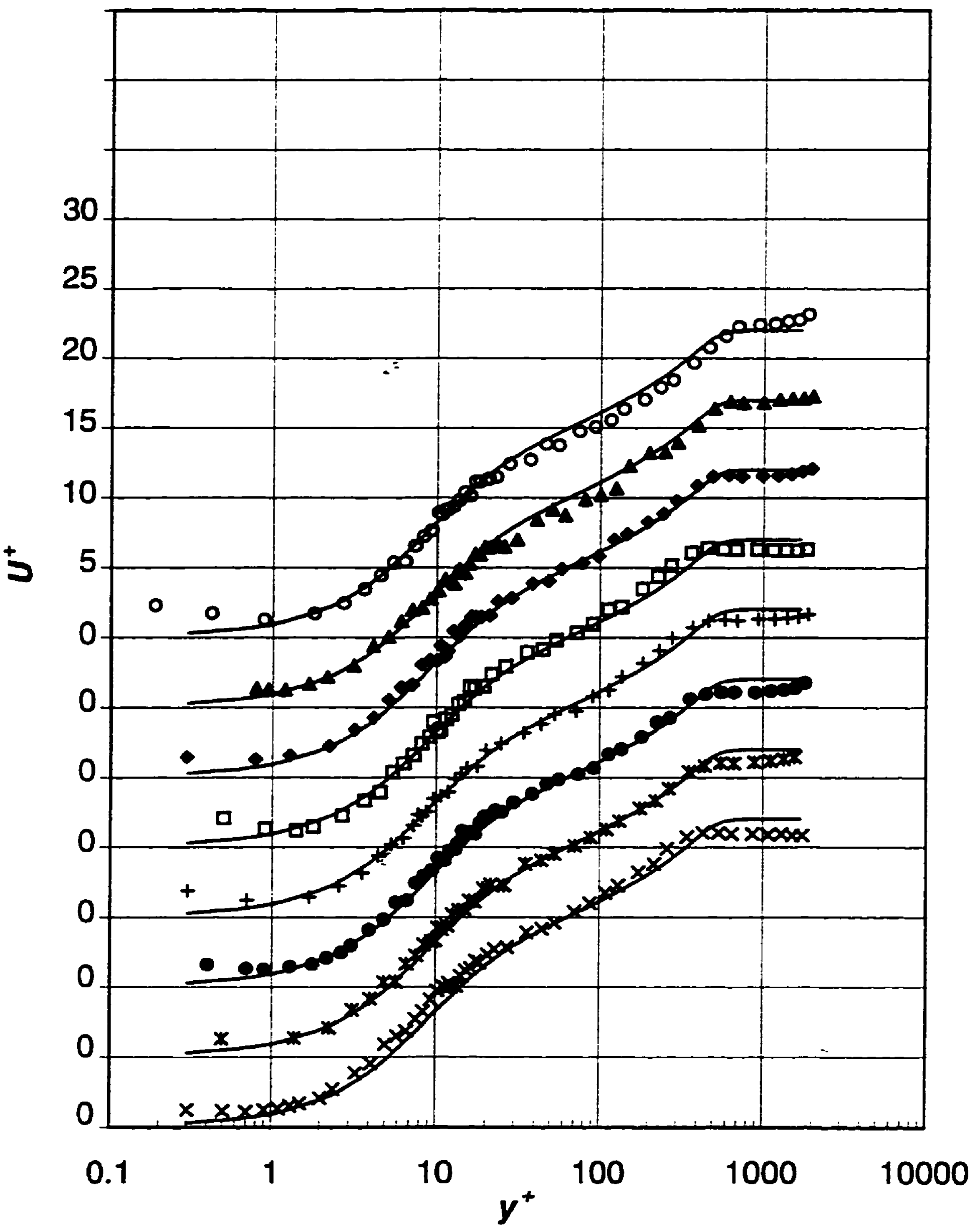

Figure 5.3.1 Mean velocity profiles over a smooth-wall at $R_w = 645$. Symbols: ×, $x/w = -11$; ✱, = -5; ●, = 1; +, = 13; □, = 33; ◆, = 81; ▲, = 181; ○, = 401; —, DNS, $R_\theta = 1410$.

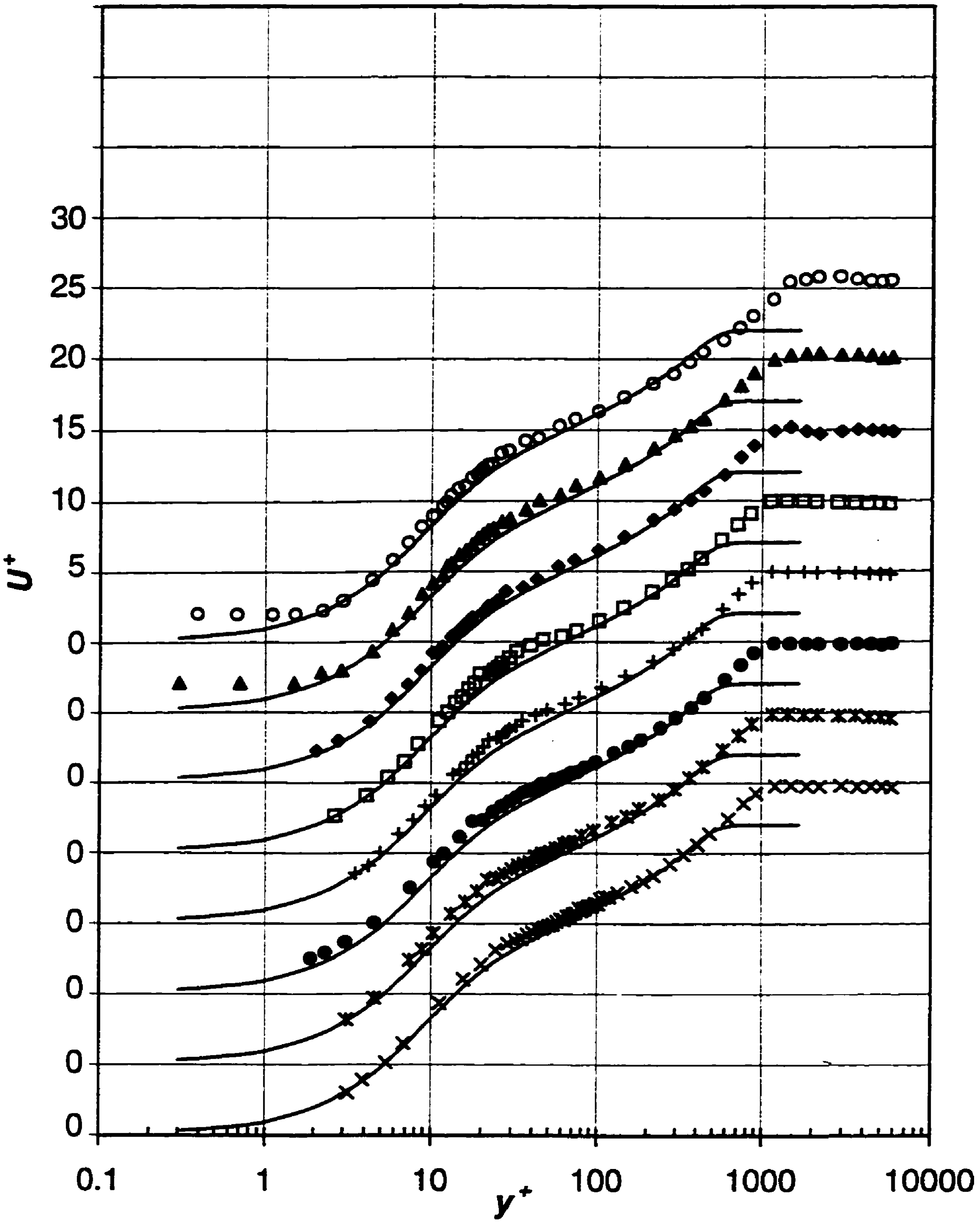

Figure 5.3.2 Mean velocity profiles over a smooth-wall at $R_w = 1774$. Symbols: ×, $x/w = -11$; ✱, = -5; •, = 1; +, = 13; □, = 33; ♦, = 81; ▲, = 181; ○, = 401; —, DNS, $R_\theta = 1410$.

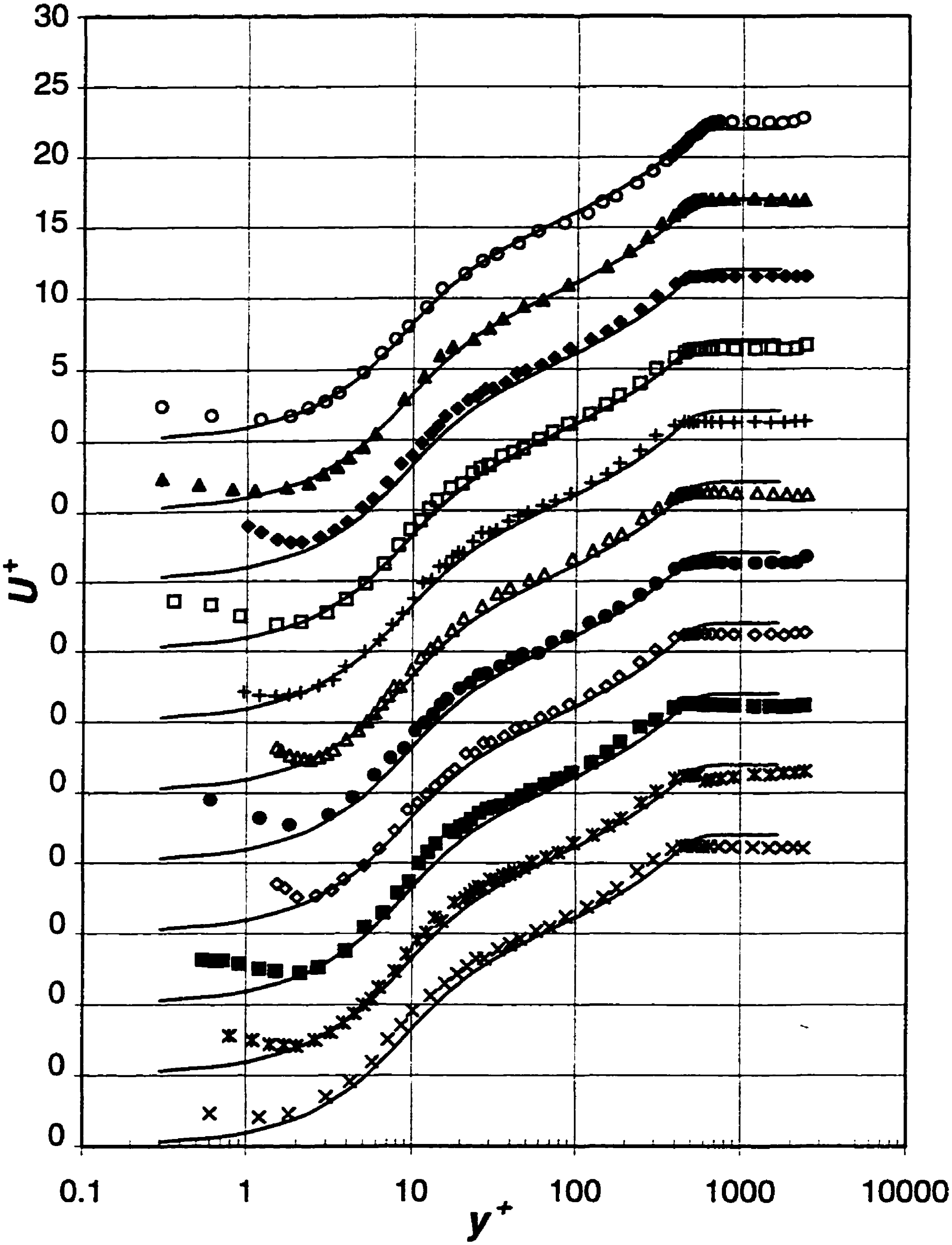

Figure 5.3.3 Mean velocity profiles over a grooved-wall at R_τ = 645. Symbols: ×, x/w = -11; ✶, = -5; ■, = -1; ◇, = 0.4; ●, = 1; △, = 1.8; +, = 13; □, = 33; ◆, = 81; ▲, = 181; ○, = 401; ——, DNS, R_θ= 1410.

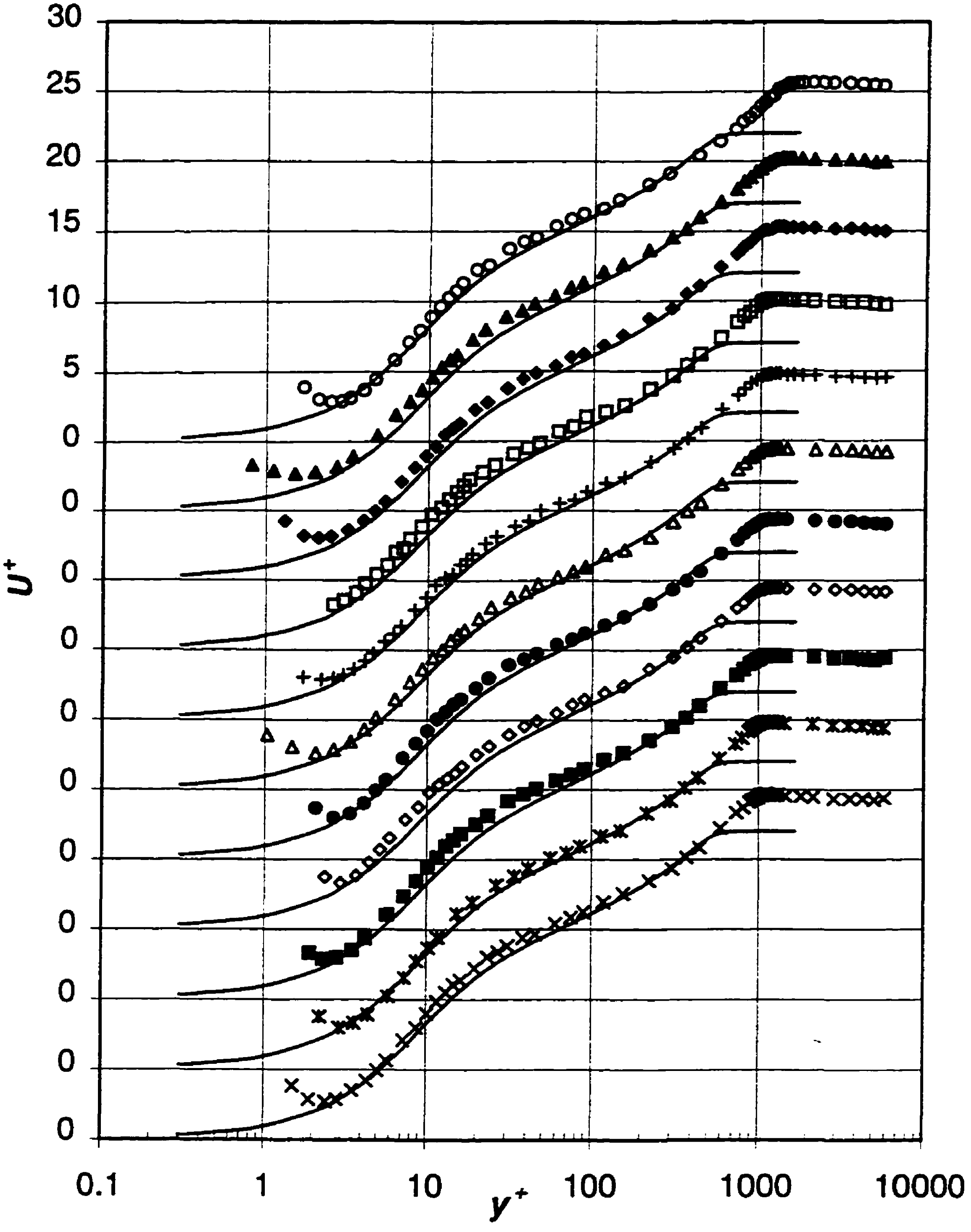

Figure 5.3.4 Mean velocity profiles over a grooved-wall at R_w = 1774. Symbols: ×, x/w = -11; *, = -5; ■, = -1; ◇, = 0.4; •, = 1; △, = 1.8; +, = 13; □, = 33; ♦, = 81; ▲, = 181; ○, = 401; —, DNS, R_θ= 1410.

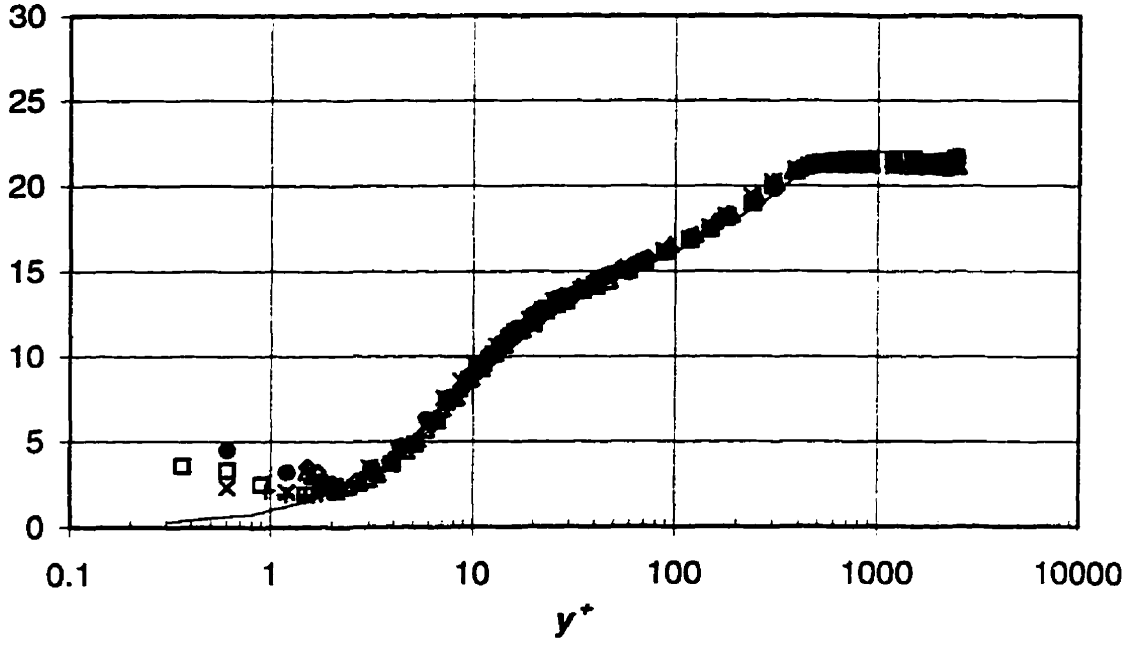

Figure 5.3.5 Mean velocity profiles over a grooved-wall at R_w = 645. Symbols: ×, x/w = -11; ◇, = 0.4; ●, = 1; △, = 1.8; +, = 13; □, = 33; ——, DNS, R_θ= 1410.

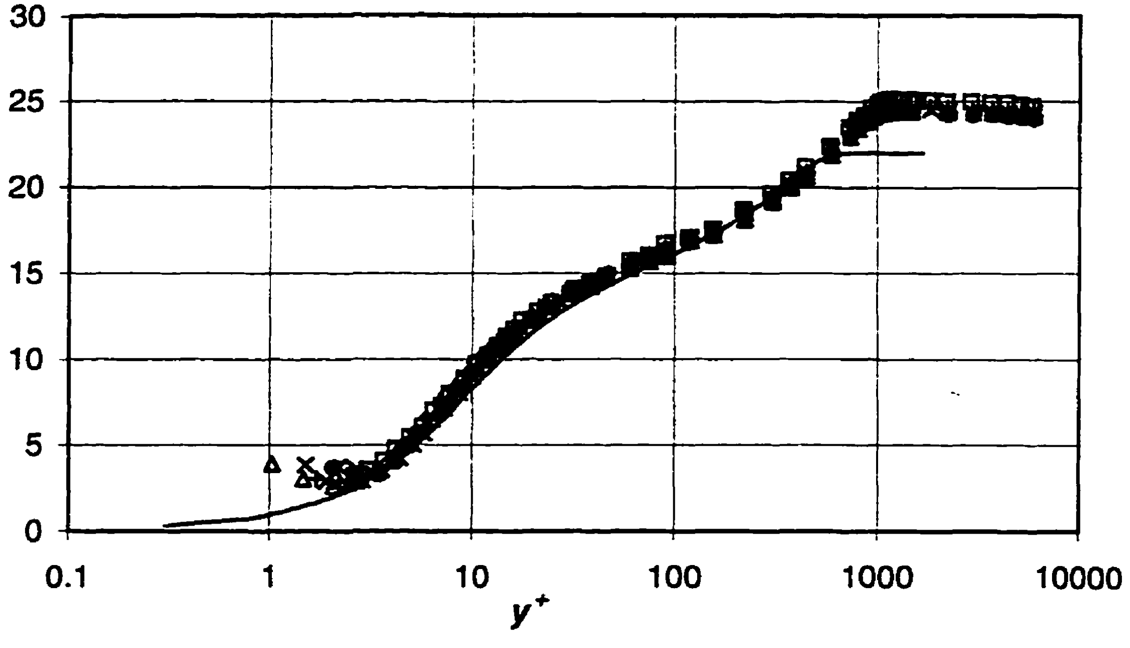

Figure 5.3.6 Mean velocity profiles over a grooved-wall at R_w = 1774. Symbols: ×, x/w = -11; ◇, = 0.4; ●, = 1; △, = 1.8; +, = 13; □, = 33; ——, DNS, R_θ= 1410.

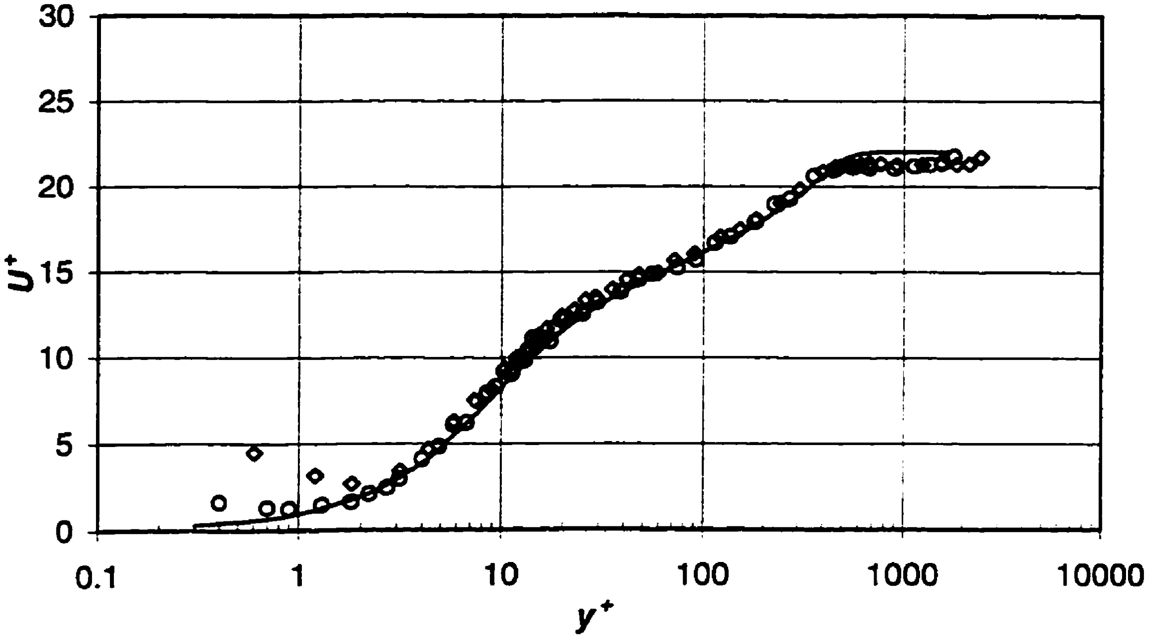

Figure 5.3.7 Mean velocity profiles at $x/w = 1$ on the smooth- and grooved-wall at $R_w = 645$. Symbols: ○, smooth-wall; ◇, grooved-wall; —, DNS, R_θ= 1410.

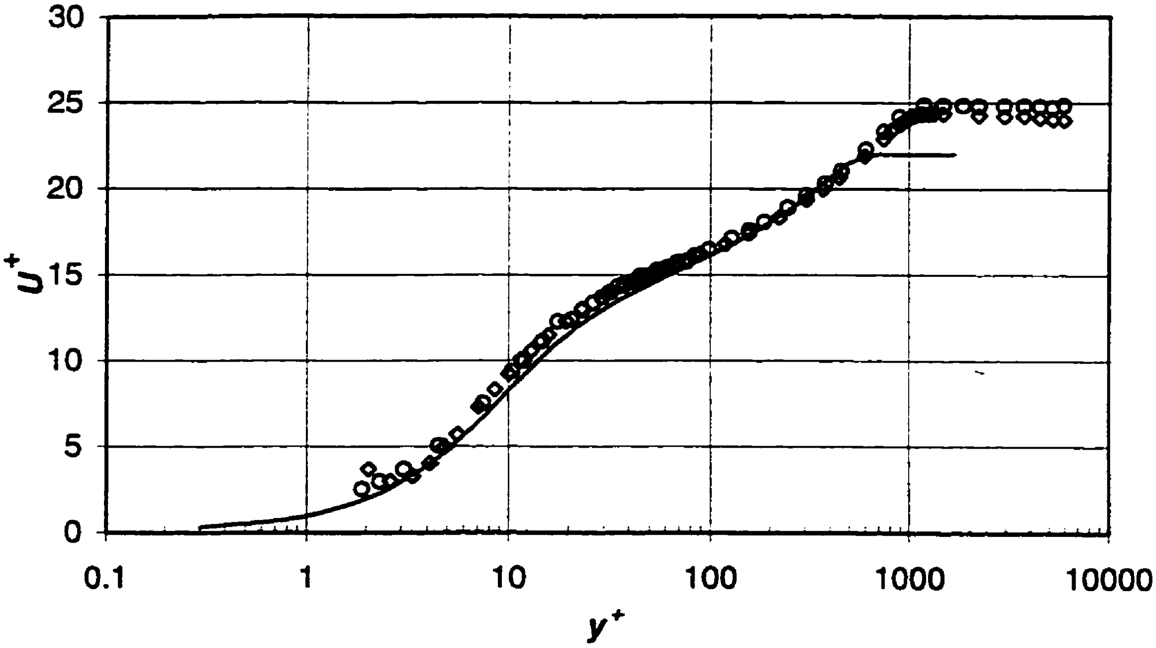

Figure 5.3.8 Mean velocity profiles at $x/w = 1$ on the smooth- and grooved-wall at $R_w = 1774$. Symbols: ○, smooth-wall; ◇, grooved-wall; —, DNS, R_θ= 1410.

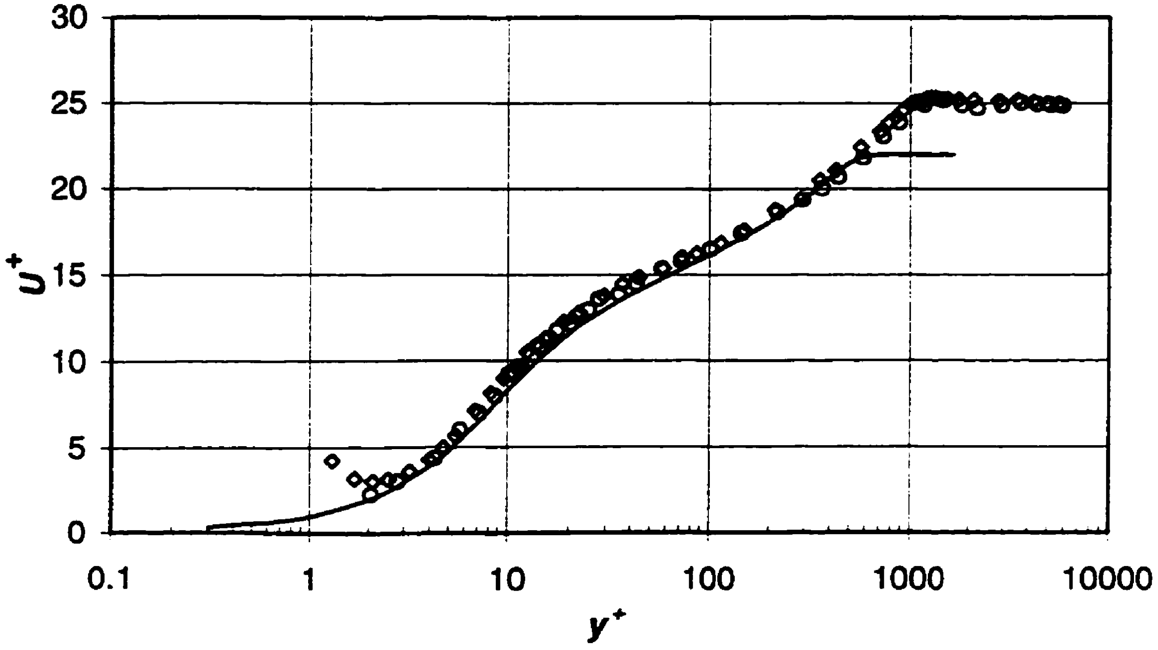

Figure 5.3.9 Mean velocity profiles at x/w = 81 on the smooth- and grooved-wall at R_w = 1774. Symbols: ○, smooth-wall; ◇, grooved-wall; —, DNS, R_θ= 1410.

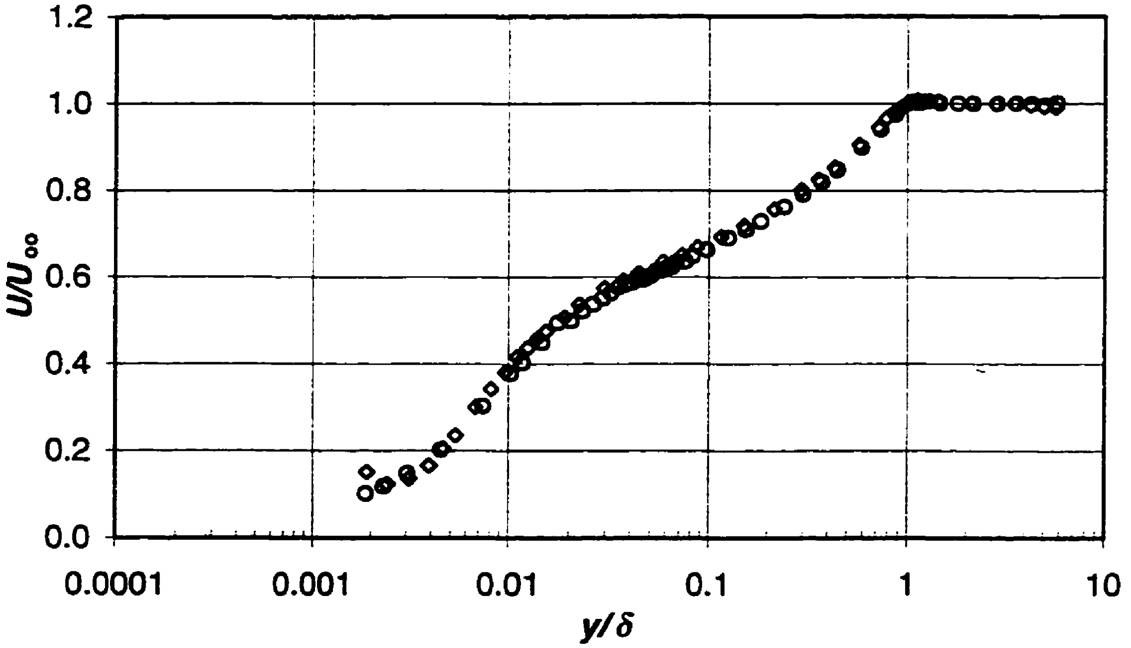

Figure 5.3.10 Mean velocity profiles at x/w = 1 on the smooth- and grooved-wall at R_w = 1774, normalized using outer variables. Symbols: ○, smooth-wall; ◇, grooved-wall.

5.4 Streamwise Turbulence Intensities

5.4.1 Smooth-Wall Results

The u^+ profiles along the streamwise direction for the smooth-wall at $R_w = 645$ are shown in Figure 5.4.1. Although there is some experimental scatter in the data, the u^+ profiles are similar to the DNS profile. At upstream locations ($x/w \approx -5$), R_θ is about 1000, and the difference in R_θ between the experimental and DNS data ($R_\theta = 1410$) is reflected in the region $y^+ \gtrsim 20$. At larger streamwise distances from the groove, the agreement between the experimental and DNS data is better, since R_θ at these locations is higher. In the region close to the wall ($y^+ \lesssim 3$), the uncertainty of probe distance from the wall is highlighted because of the log scale used for the abscissa. The peak value of u^+ (u^+_{max}) occurs at $y^+ \approx 13$, and $u^+_{max} \approx 2.7$, which is in agreement with the DNS data.

The similarity of the streamwise u^+ profiles on the smooth-wall can be seen better by plotting them superimposed (Figure 5.4.2). The corresponding smooth-wall DNS data (Spalart, 1988) are also shown for comparison. Only the outer region ($y^+ \gtrsim 30$) is affected by the Reynolds number.

The u^+ profiles at $R_w = 1774$ for the smooth-wall are shown in Figure 5.4.3. Similar to the low R_w case, the peak value of u^+ occurs at $y^+ \approx 13$. There is good agreement between the experimental and DNS data, and there is far less scatter in the data compared to the profiles at the lower R_w. $u^+_{max} = 2.7$ for all profiles, and is in good agreement with DNS data.

For a better comparison, a few u^+ profiles are shown superimposed in Figure 5.4.4. There is a good collapse of the profile throughout the layer. The rightward shift of

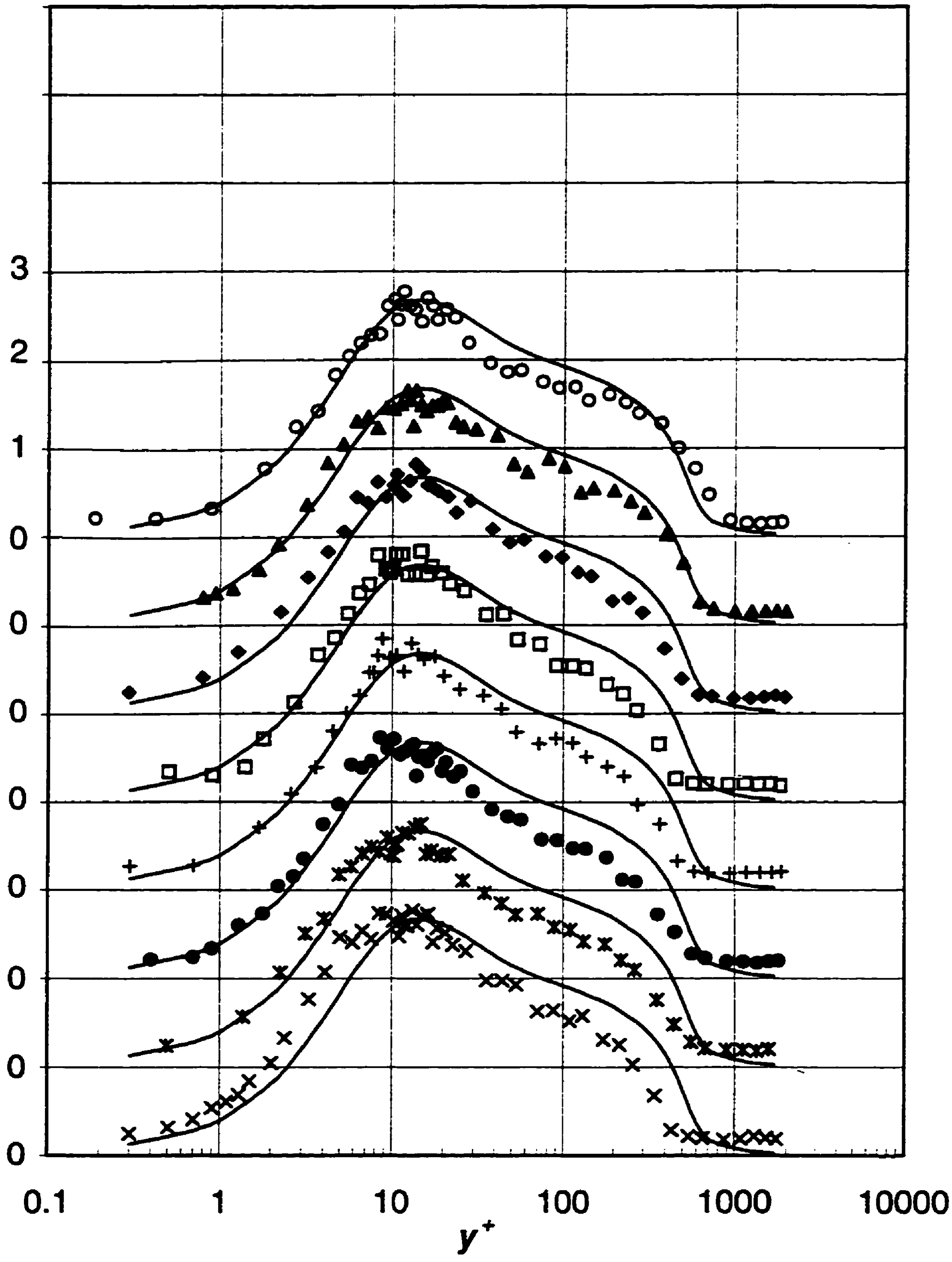

Figure 5.4.1 Streamwise turbulence intensity profiles over a smooth-wall at R_w = 645. Symbols: ×, x/w = -11; ∗, -5; ●, 1; +, 13; □, 33; ◆, 81; ▲, 181; ○, 401; ——, DNS, R_θ =1410.

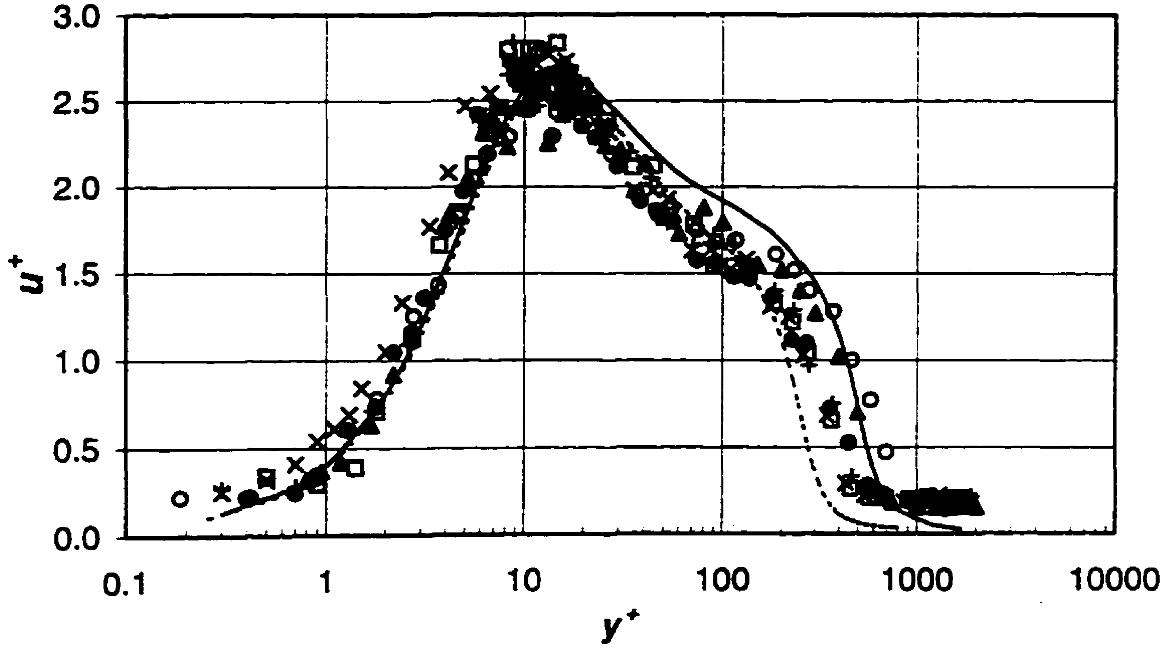

Figure 5.4.2 Streamwise turbulence intensity profiles over a smooth-wall at R_w = 645. Symbols: ×, x/w = -11; ●, 1; +, 13; □, 33; ▲, 181; ○, 401; - - -, DNS, R_θ = 670; —, R_θ = 1410.

the experimental data for $y^+ \gtrsim 200$ compared to the DNS data is due to the higher R_θ (Perry and Abbel, 1975; Purtell et al., 1981).

5.4.2 Grooved-Wall Results

The u^+ profiles along the streamwise direction for the grooved-wall at R_w = 645 are shown in Figure 5.4.5. As the streamwise distance increases, the experimental profiles more closely match the DNS profile. This is because of the increase in R_θ, and also the relaxation of the boundary layer after the perturbation due to the cavity. For example, the profiles at the last two measurement locations (x/w = 181 and 401) are in good agreement with the DNS profile. For these profiles, R_θ is 1250 and 1650 compared to 1410 for the DNS data. The location of u^+_{max} remains unaffected by the cavity at these two x/w

locations. The profile at x/w = 81 is slightly lower than the DNS profile in the inner region, and may reflect the higher value of u_τ at that location.

The u^+ profiles at selected x/w locations for R_w = 645 and 1774 are shown superimposed in Figure 5.4.7 and Figure 5.4.8, respectively, to allow a better comparison between the profiles. Though there is some deviation in the region $y^+ \leq 3$, there is, in general, good collapse of the data in the rest of the layer. The measurement error increases as the wall is approached, and is the main reason for the scatter in the data for $y^+ \leq 3$.

At R_w = 1774, the influence of the groove is discernible at locations very close to the groove (Figures 5.4.6). At x/w = -5, u^+ is lower than the DNS data. At this location, $C_f/C_{f,0}$ is 1.02, and the lower value of u^+ is probably because of the higher u_τ. At the next location (x/w = -1), the data, though still lower, is closer to the DNS data.

5.4.3 Comparison between Smooth- and Grooved-Wall u^+ Profiles

A direct comparison between the smooth- and grooved-wall u^+ profiles at two locations downstream of the cavity (x/w = 1 and 81) at R_w = 645 reveal slight differences between the two cases (Figure 5.4.9 and 5.4.10). In the near-wall region ($y^+ \leq 10$), the u^+ on the grooved-wall is lower than the smooth-wall value at both locations, however, at x/w = 81, u^+ on the grooved-wall is lower than the smooth-wall value throughout the layer (Figure 5.4.10). As mentioned previously, this is because of the higher value of u_τ at that location. The presence of the cavity is likely to weaken the streamwise vorticity in the near-wall region, and result in a decrease in u^+ at both x/w locations.

At $R_w = 645$, there is a slight reduction in u^+_{max} in the vicinity of the groove. At $x/w = 1$, where $C_f/C_{f,0} < 1.0$, u^+_{max} on the grooved-wall is lower than the smooth-wall value (Figure 5.4.9). Surprisingly, at $x/w = 81$, u^+_{max} is also lower than the corresponding smooth-wall value, although at this location $C_f/C_{f,0} > 1.0$. Therefore, it is likely there is no general correlation between u^+_{max} and the local $C_f/C_{f,0}$ in the present study. It could also be likely that, because of the small change in $C_f/C_{f,0}$ and u^+_{max}, the experimental uncertainty masks any correlation between the two.

The turbulence intensity profiles of Figures 5.4.9 and 5.4.10 are shown normalized using outer variables (U_∞ and δ) in Figures 5.4.11 and 5.4.12, respectively. The advantage of using outer variables in this instance is that U_∞ changes very little with x. This permits a direct comparison of the turbulence intensity of the two cases. On the other hand, the inner variable u_τ changes with x, and this change is also reflected in the u^+ profiles. The u/U_∞ profiles show a similar behavior to the u^+ profiles. At $x/w = 1$, u/U_∞ on the grooved-wall is lower than the smooth-wall value in the region $y/\delta \lesssim 0.02$, while at $x/w = 81$, it is lower throughout the layer.

The u^+ profiles on the smooth- and grooved-wall at $R_w = 1774$ at $x/w = 1$ and 81 are compared in Figures 5.4.13 and 5.4.14. These two locations are selected because $C_f/C_{f,0}$ is a maximum and minimum at $x/w = 1$ and 81 ($C_f/C_{f,0} = 1.05$ and 0.98, respectively). The peak value of u^+ at both x/w locations is unchanged, however, in the region $y^+ \lesssim 10$, u^+ on the grooved-wall is slightly lower than on the smooth-wall. These results are similar to those at the lower Reynolds number. The cavity attenuates the turbulence intensity in this region, and this effect seems to be confined to the near-wall region.

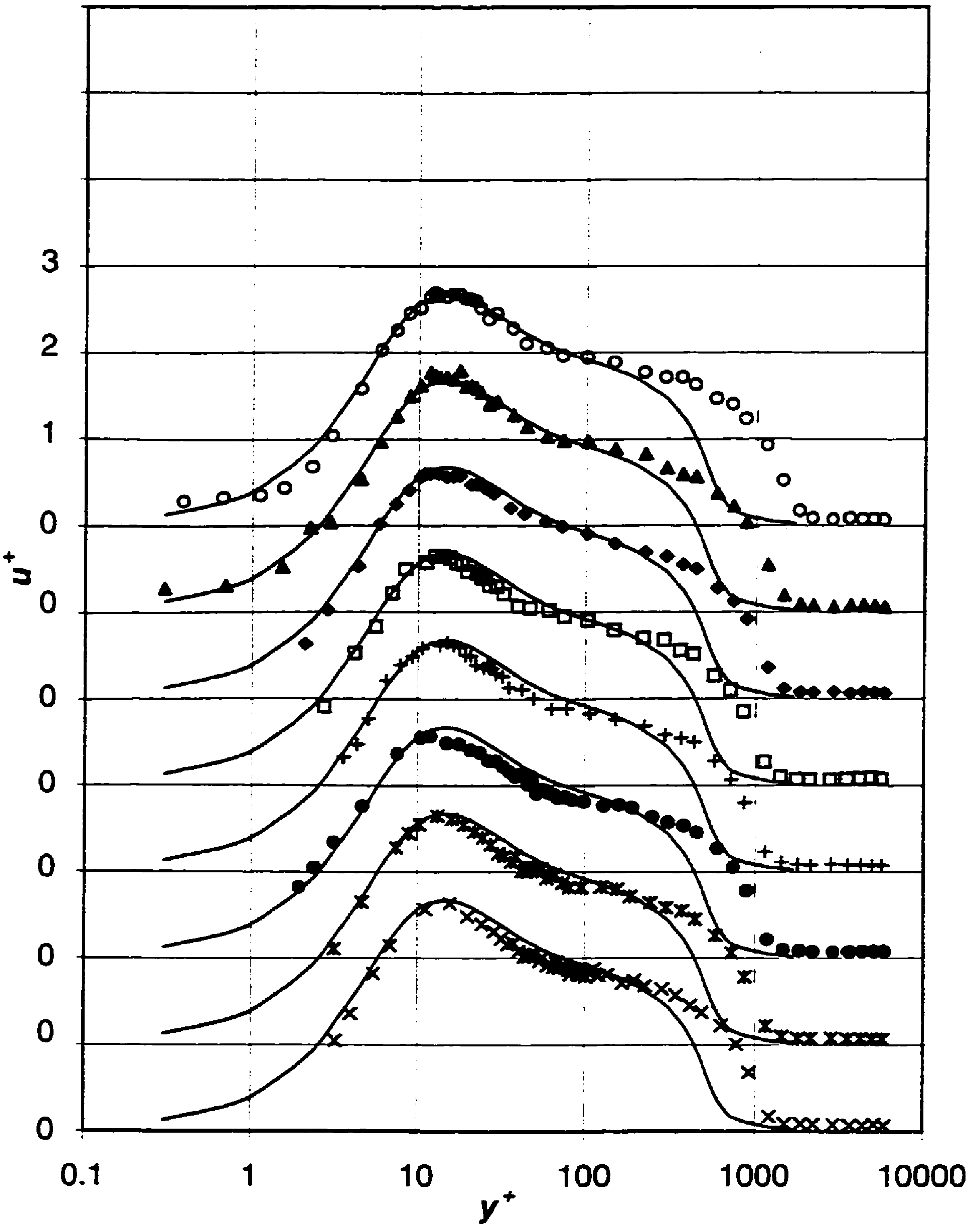

Figure 5.4.3 Streamwise turbulence intensity profiles on the smooth-wall at R_w = 1774. Symbols: ×, x/w = -11; ✱, -5; ●, 1; +, 13; □, 33; ◆, 81; ▲, 181; ○, 401; ——, DNS, R_θ =1410.

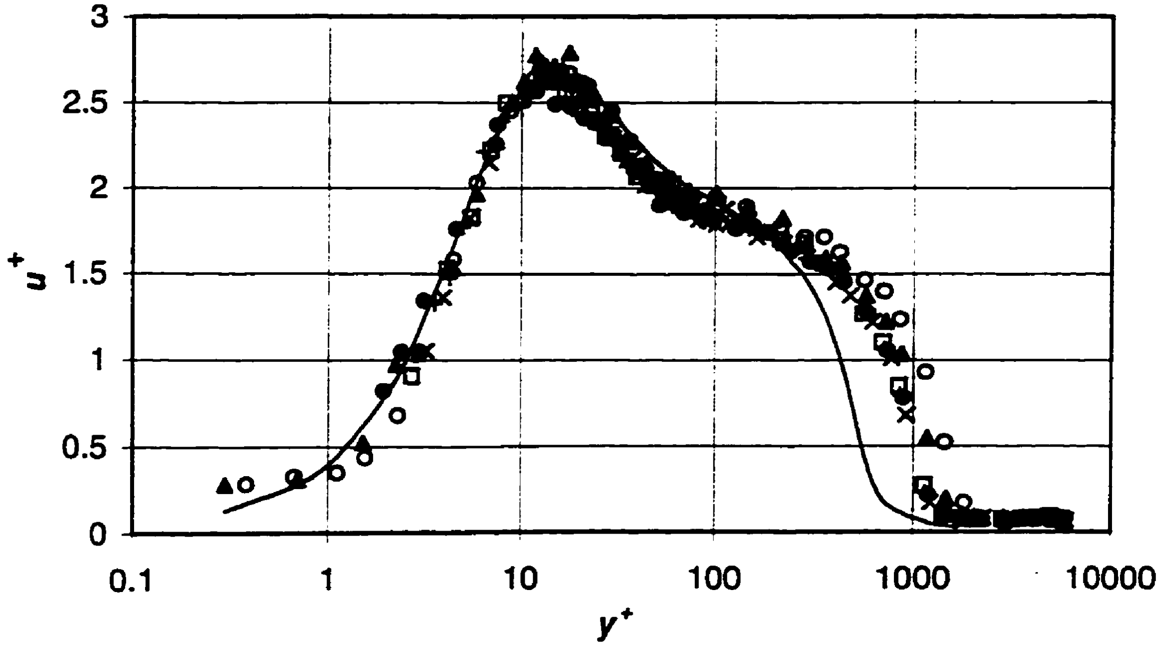

Figure 5.4.4 Streamwise turbulence intensity profiles over a smooth-wall at R_w = 1774. Symbols: ×, x/w = -11; ●, 1; +, 13; □, 33; ▲, 181; ○, 401; ——, DNS, R_θ =1410.

The turbulence intensity profiles at x/w = 1 and 81 at R_w = 1774 are shown normalized using outer variable in Figures 5.4.15 and 5.4.16, respectively. Qualitatively, the u/U_∞ profiles are similar to the u^+ profiles, with u/U_∞ for the grooved-wall slightly less than the smooth-wall value in the region $y/\delta \lesssim 0.006$.

At R_w = 645, the groove reduces u^+_{max} or $(u/U_\infty)_{max}$, however, at R_w = 1774, the effect of the groove on u^+_{max} or $(u/U_\infty)_{max}$ is not significant. At both R_w, the effect of the cavity on u^+ and u/U_∞ in the near-wall region is discernible. In this region, there is a decrease in u^+ and u/U_∞. In the region $y^+ \geq 10$, u^+ profiles on the smooth- and grooved-wall at R_w = 1774 are indistinguishable. The overall effect of the cavity on u^+ is very weak, because the ratio d/δ_1 is very small in this case.

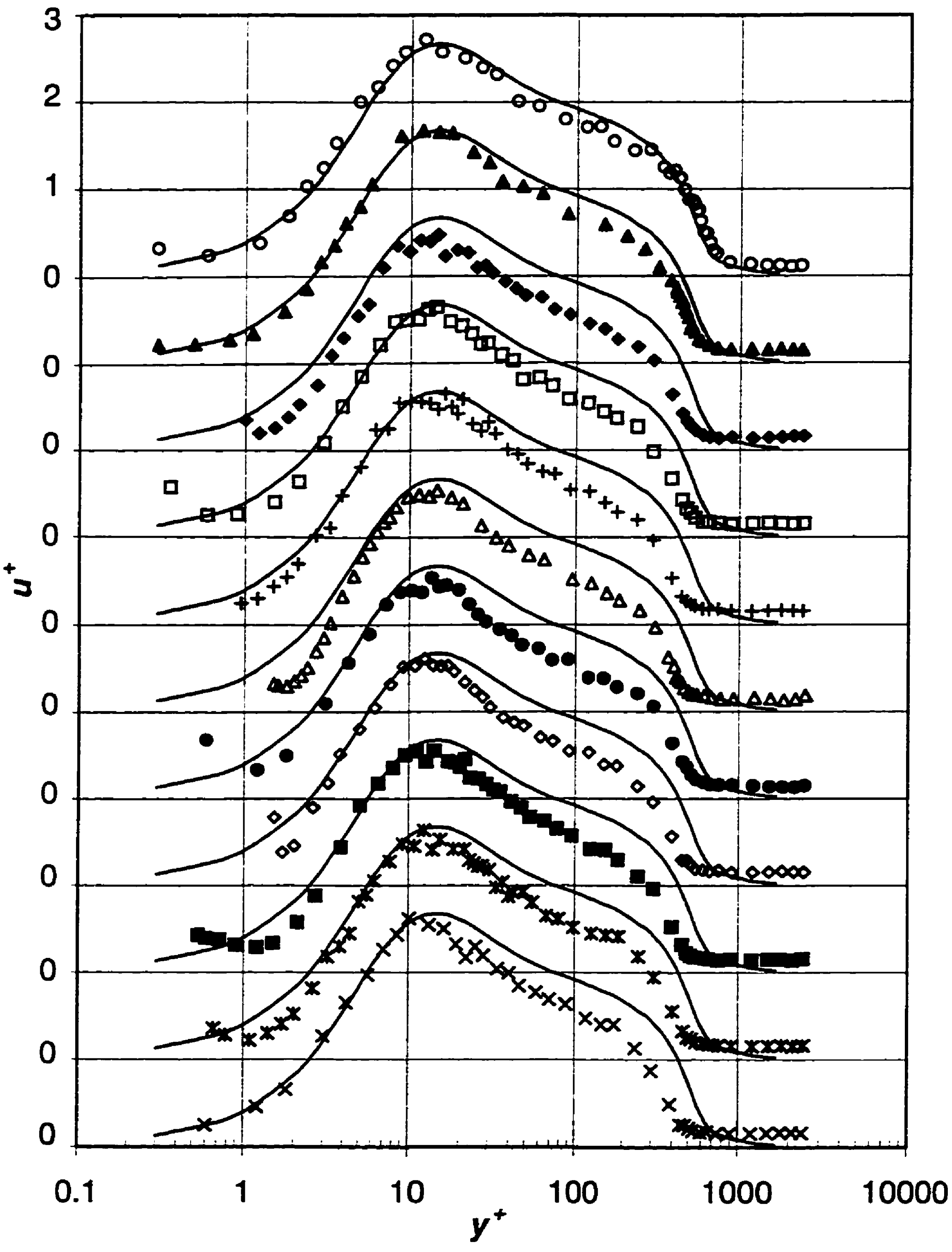

Figure 5.4.5 Streamwise turbulence intensity profiles over a grooved-wall at R_w = 645. Symbols: ×, x/w = -11; ∗, -5; ■, -1; ◇, 0.4; ●, 1; △, 1.8; +, 13; □, 33; ◆, 81; ▲, 181; ○, 401; ——, DNS, R_θ =1410.

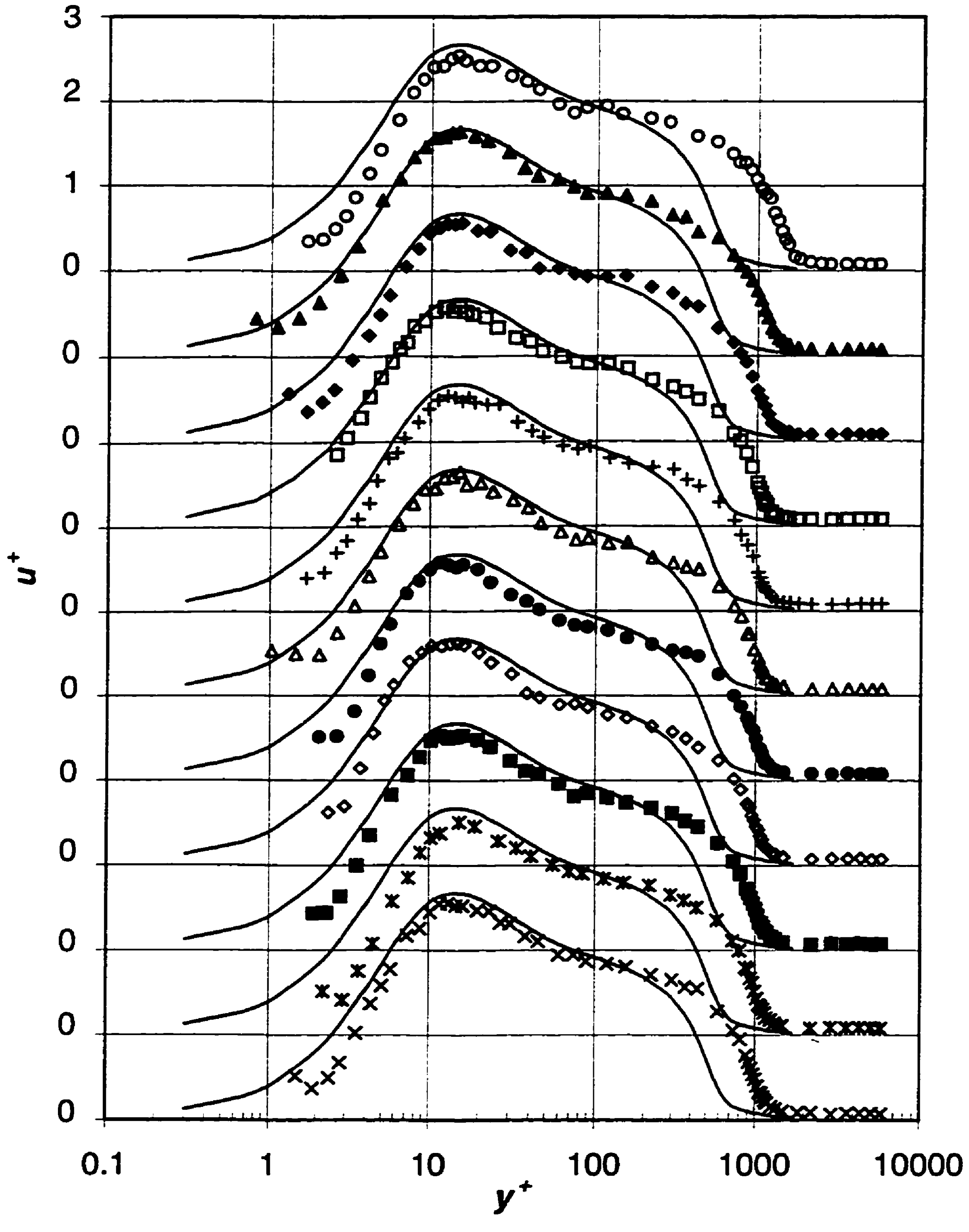

Figure 5.4.6 **Streamwise turbulence intensity profiles over a grooved-wall at R_w = 1774. Symbols: ×, x/w = -11; ∗, -5; ■, -1; ◇, 0.4; ●, 1; △, 1.8; +, 13; □, 33; ◆, 81; ▲, 181; ○, 401; ——, DNS, R_θ =1410.**

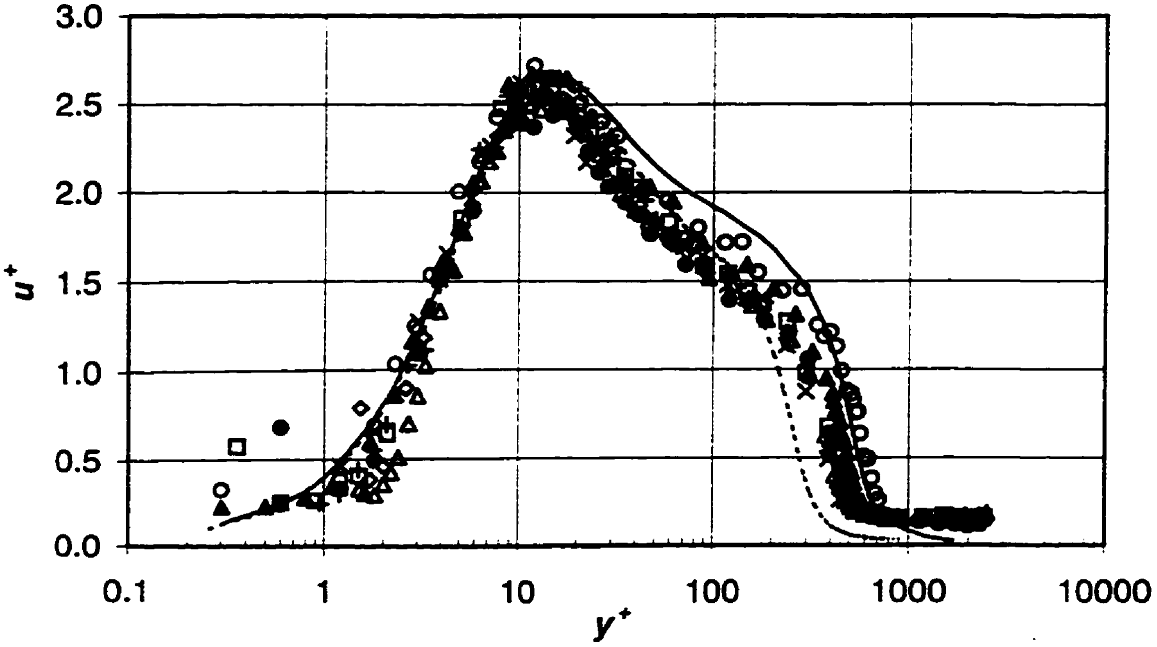

Figure 5.4.7 Streamwise turbulence intensity profiles over a grooved-wall at R_w = 645. Symbols: ×, x/w = -11; ◇, 0.4; ●, 1; △, 1.8; +, 13; □, 33; ▲, 181; ○, 401; DNS: - - - - -, $R_\theta = 670$; ——, R_θ =1410.

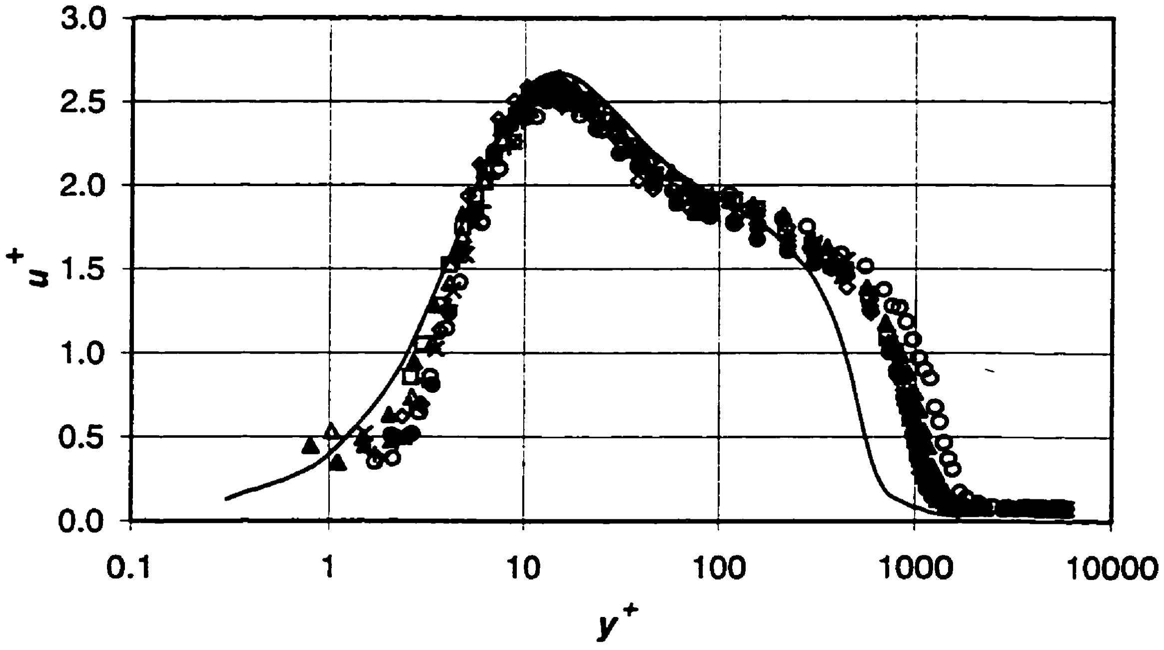

Figure 5.4.8 Streamwise turbulence intensity profiles over a grooved-wall at R_w= 1774. Symbols: ×, x/w = -11; ◇, 0.4; ●, 1; △, 1.8; +, 13; □, 33; ▲, 181; ○, 401; ——, DNS, R_θ =1410.

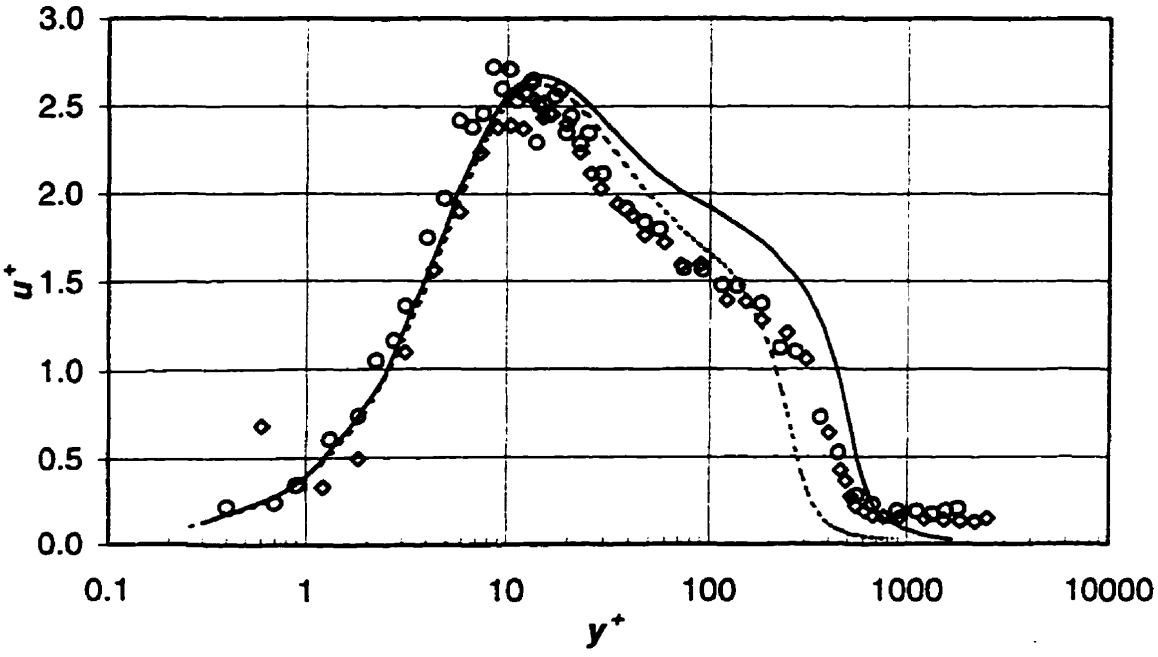

Figure 5.4.9 Streamwise turbulence intensity profiles on the smooth- and grooved-wall at R_w = 645 and x/w = 1. Symbols: ○, smooth-wall; ◇, grooved-wall; DNS data: - - - - - , R_θ = 670; ——, =1410.

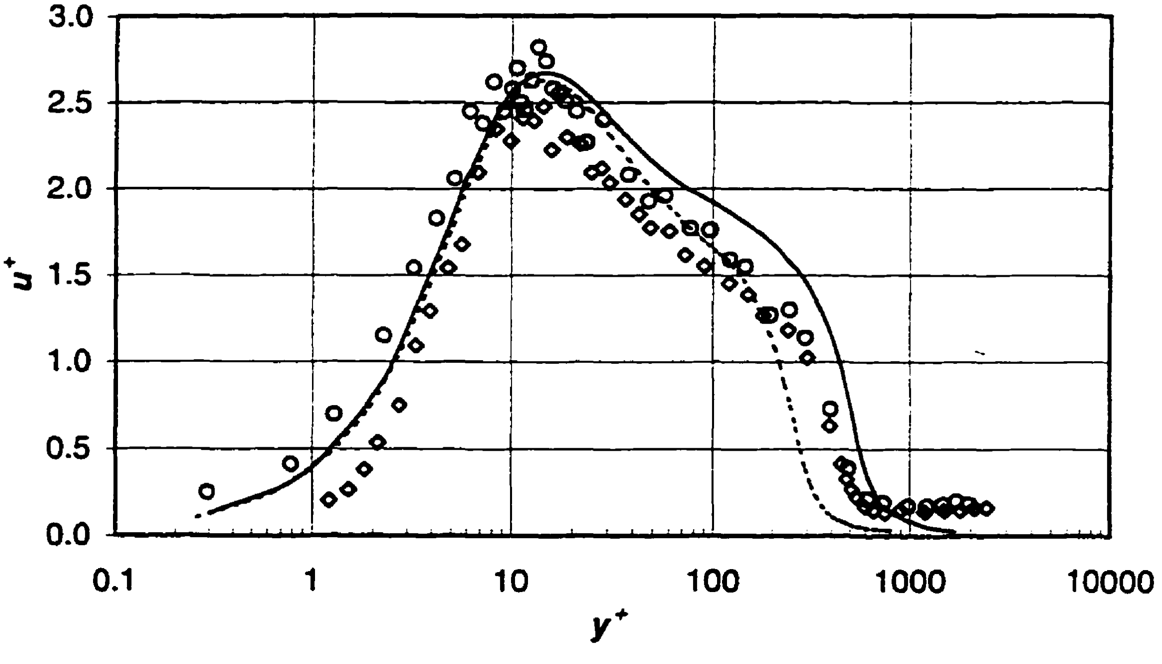

Figure 5.4.10 Streamwise turbulence intensity profiles on the smooth- and grooved-wall at R_w = 645 and x/w = 81. Symbols: ○, smooth-wall; ◇, grooved-wall; DNS data: - - -, R_θ = 670; ——, =1410.

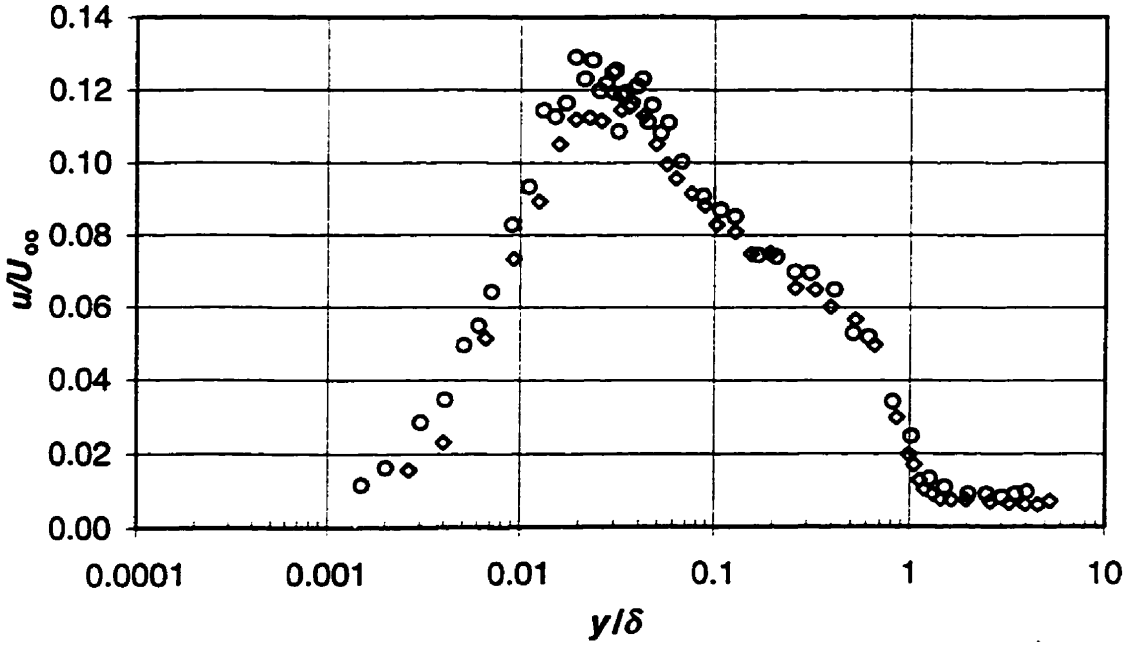

Figure 5.4.11 **Streamwise turbulence intensity profiles on the smooth- and grooved-wall at R_w = 645 and x/w = 1 normalized using outer variables. Symbols: ○, smooth-wall; ◇, grooved-wall;**

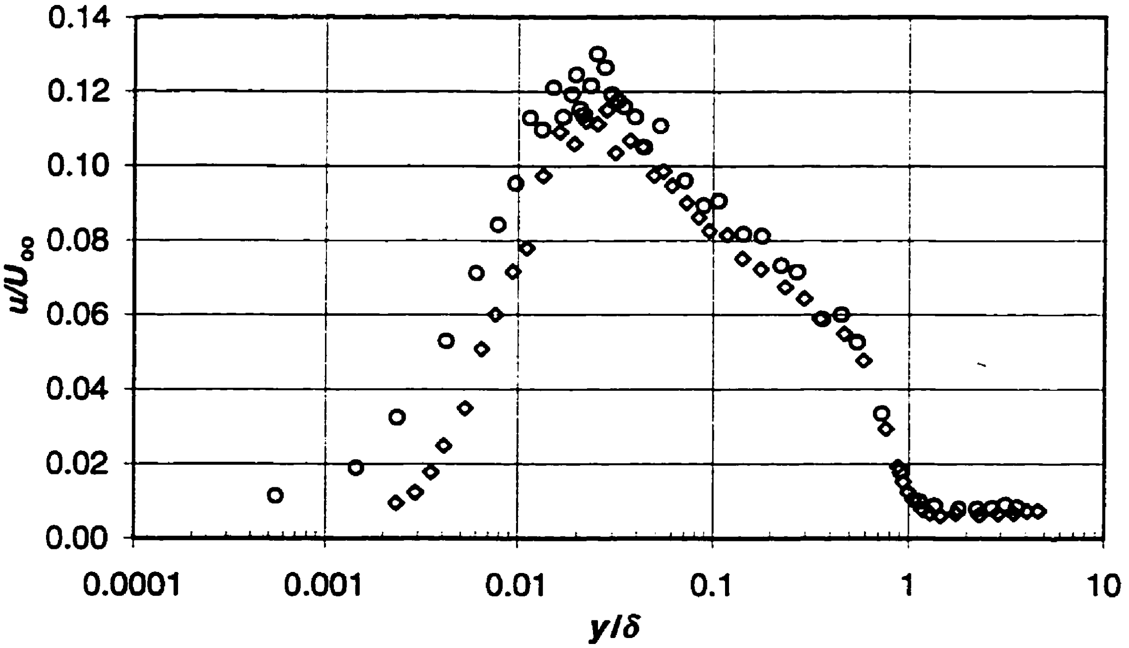

Figure 5.4.12 **Streamwise turbulence intensity profiles on the smooth- and grooved-wall at R_w = 645 and x/w = 81 normalized using outer variables. Symbols: ○, smooth-wall; ◇, grooved-wall;**

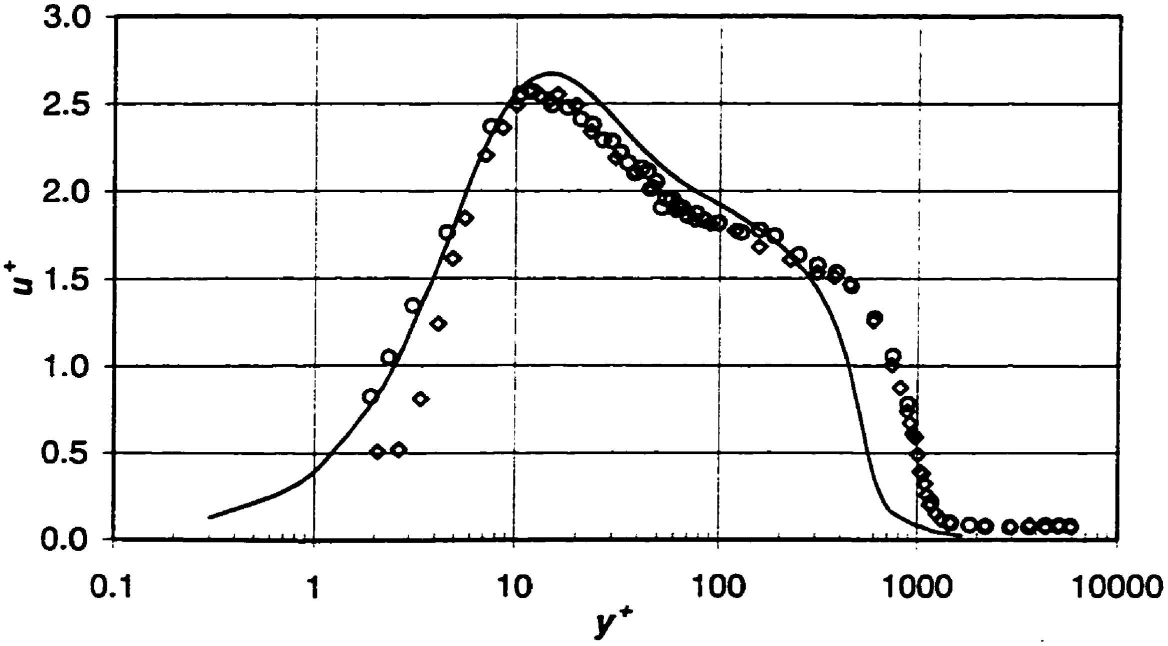

Figure 5.4.13 Streamwise turbulence intensity profiles on the smooth- and grooved-wall at $R_w = 1774$ and $x/w = 1$. Symbols: ○, smooth-wall; ◇, grooved-wall; DNS data: ——, $R_\theta = 1410$.

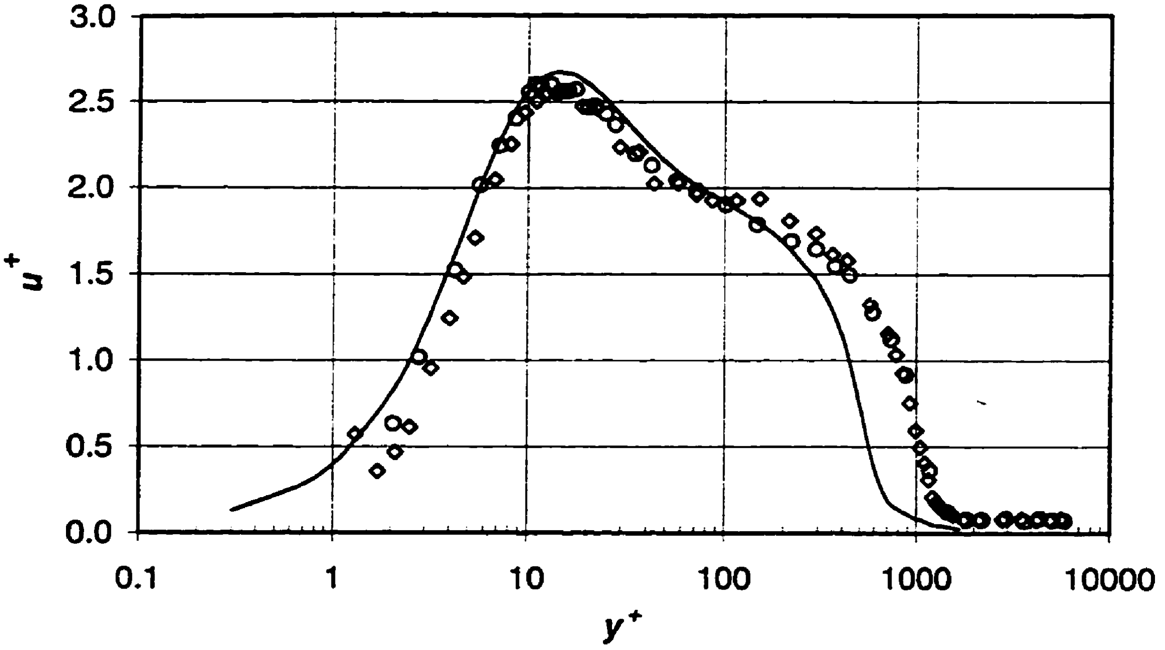

Figure 5.4.14 Streamwise turbulence intensity profiles on the smooth- and grooved-wall at $R_w = 1774$ and $x/w = 81$. Symbols: ○, smooth-wall; ◇, grooved-wall; DNS data: ; ——, $R_\theta = 1410$.

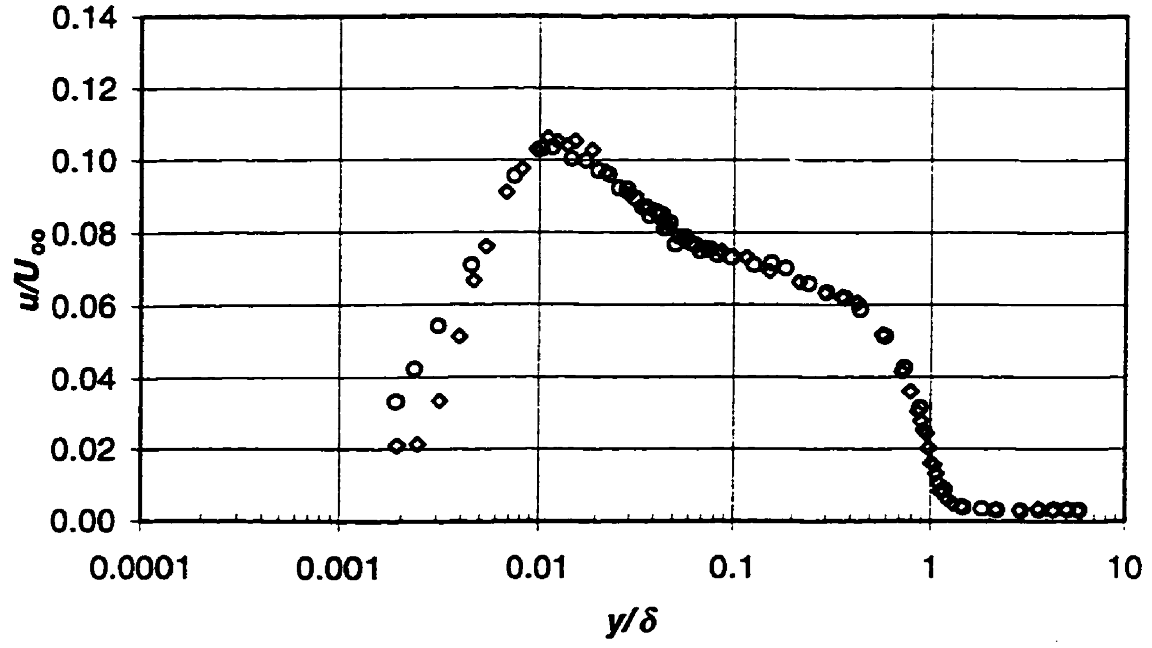

Figure 5.4.15 Streamwise turbulence intensity profiles on the smooth- and grooved-wall at R_w = 1774 and x/w = 1 normalized using U_∞ and δ. Symbols: ○, smooth-wall; ◇, grooved-wall;

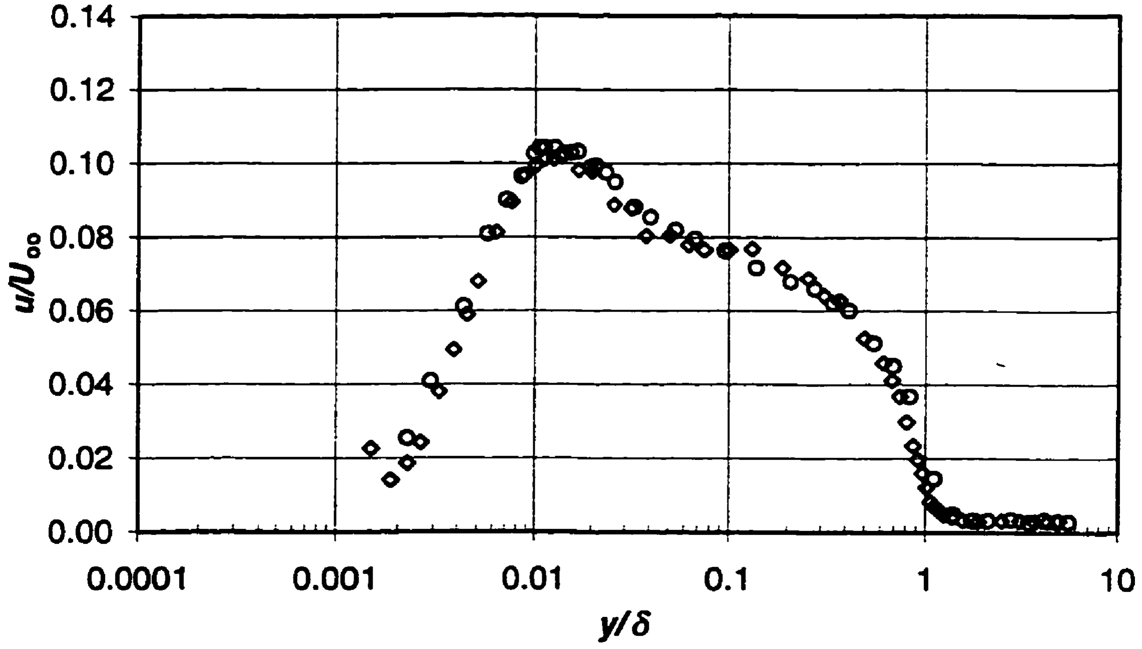

Figure 5.4.16 Streamwise turbulence intensity profiles on the smooth- and grooved-wall at R_w = 1774 and x/w = 81 normalized using U_∞ and δ. Symbols: ○, smooth-wall; ◇, grooved-wall;

5.5 Wake Parameter (π)

The wake parameter (π) characterizes the outer region of the mean velocity profile in turbulent boundary layers, and is generally dependent on x. If the boundary layer is in equilibrium, however, π is independent of x (Tani, 1987a). The streamwise distributions of π on the smooth- and grooved-wall at $R_w = 645$ are shown in Figure 5.5.1. There is an increase in π with x for the smooth-wall. Matsumoto (1994) found that a reduction in C_f results in an increase in π. In a zero pressure gradient turbulent boundary layer over a smooth-wall, C_f decreases along the streamwise direction. The systematic increase in π is consistent with this C_f distribution. The increase in π with x for the grooved-wall is less pronounced. For the smooth-wall case, π increases from 0.3 to 0.5 as x/w increases from -10 to 400. In the case of the grooved-wall, π is approximately constant at 0.38, although a slight increase with x is discernible. Matsumoto (1994) found that π was constant at 0.53 and 0.59 for a turbulent boundary layer over a sparse d-type roughness with $s/d = 10$ and 20, respectively. Choi and Fujisawa (1993) found that π varied with x in a range $0.35 \lesssim \pi \lesssim 0.40$ for a turbulent boundary layer downstream of a transverse square cavity with $d/\delta_1 = 0.4$.

It is not possible to infer any conclusive information on the C_f distribution from the π distribution at $R_w = 645$. For $x/w \lesssim 100$, π on the grooved-wall is higher than that on the smooth-wall, while for $x/w \gtrsim 100$, it is lower than that on the smooth-wall. This is not consistent with the $C_f/C_{f,0}$ distribution (Figure 5.2.5), and is probably due to the scatter of the data and the very small changes in $C_f/C_{f,0}$ and experimental error.

The distribution of π on the smooth- and grooved-walls at $R_w = 1774$ is shown in Figure 5.5.2. The value of π on the smooth-wall varies from 0.63 to 0.65 as x/w increases.

These values are higher than those at the lower R_w, because C_f is lower at $R_w = 1774$. There is a decrease in π in the vicinity of the groove. The decrease is followed by an increase and subsequent relaxation back to the smooth-wall value. There is a strong correlation between the π and C_f distributions (Figure 5.2.2) in this case. For the smooth-wall, π increases with x, while C_f decreases with x. For the grooved-wall, π is lower than that on the smooth-wall for $x/w \lesssim 30$, and higher than that on the smooth-wall value in the range $30 \lesssim x/w \lesssim 100$. This is completely opposite to the $C_f/C_{f,0}$ distribution as one would expect. In the region $x/w \gtrsim 100$, the π-distributions on the smooth- and grooved-wall are almost the same with a monotonic increase with x. The behavior of the π-distribution at $R_w = 1774$ corroborates the results of Matsumoto (1994) and Tani (1987a), that a reduction in C_f results in an increase in π and vice versa.

5.6 Energy Spectra

The energy spectra of the streamwise velocity fluctuations on the smooth-wall at $R_w = 645$ and 1774 at $x/w = 1$ are presented in Figures 5.6.1 and 5.6.2, respectively. The spectra at different locations in the layer are shown. The spectrum is evaluated by a Fast Fourier Transform applied to 29 successive blocks, each containing 1024 data points. Finally, the energy spectra from the 29 blocks are averaged.

The energy spectra ($E_1(k_1)/\overline{u^2}$) is plotted against the wave number k_1 (k_1 is the one dimensional wave number defined as $2\pi f/U$, where f and U are frequency and local mean velocity, respectively). Hinze (1959) defines the energy spectra as

$$E_1(k_1) = \frac{U}{2\pi} E_1(f) \tag{5.3}$$

so that

$$\overline{u^2} = \int_0^{\infty} E_1(k_1)dk_1 \tag{5.4}$$

The present method follows the method used by Klebanoff (1955).

The turbulent energy is spread out over about two decades in wave number at the lower R_w, and about three decades at the higher R_w. The energy at the lower wave number decreases as the wall is approached. This is because the energy containing eddies are larger at the lower wave number (i.e. lower frequency) than eddies at the higher wave number. As the wall is approached, the large eddy motions are damped. This results in a lower energy in the large eddies at distances closer to the wall.

Figure 5.6.3 compares the energy spectra on the smooth- and grooved-wall at the two R_w. The spectra are at the streamwise location immediately downstream of the cavity ($x/w = 1$) and at the y-location where the turbulence intensity is maximum ($y^+ \approx 13$). There is no distinguishable difference between the spectrum on the smooth- and grooved-wall at both R_ws. As R_w increases, the high wave number component of energy increases, while the low wave number component decreases. It may be concluded that the groove has no effect on the spectral distribution of the turbulent kinetic energy.

5.7 Turbulent Kinetic Energy Dissipation Rate (ε)

The distributions of $\varepsilon/(U_\infty)^2$ across the layer at $R_w = 645$ and 1774 at $x/w = 1$ are shown in Figures 5.7.1 and 5.7.2. The figures are presented using a semi logarithmic scale to enhance the near wall region. In each figure, the distributions of $\varepsilon/(U_\infty)^2$ for the smooth- and grooved-wall are compared.

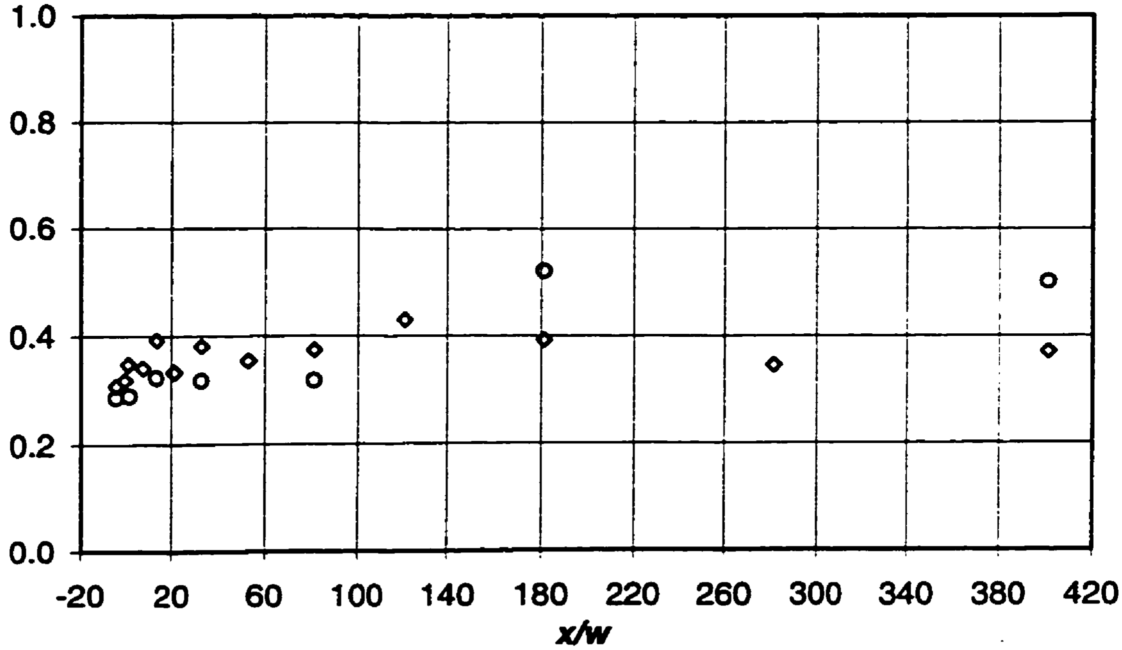

Figure 5.5.1 Wake parameter (π) distribution on the smooth- and grooved-wall at $R_w = 645$.
Symbols: ○, smooth-wall; ◇, grooved-wall;

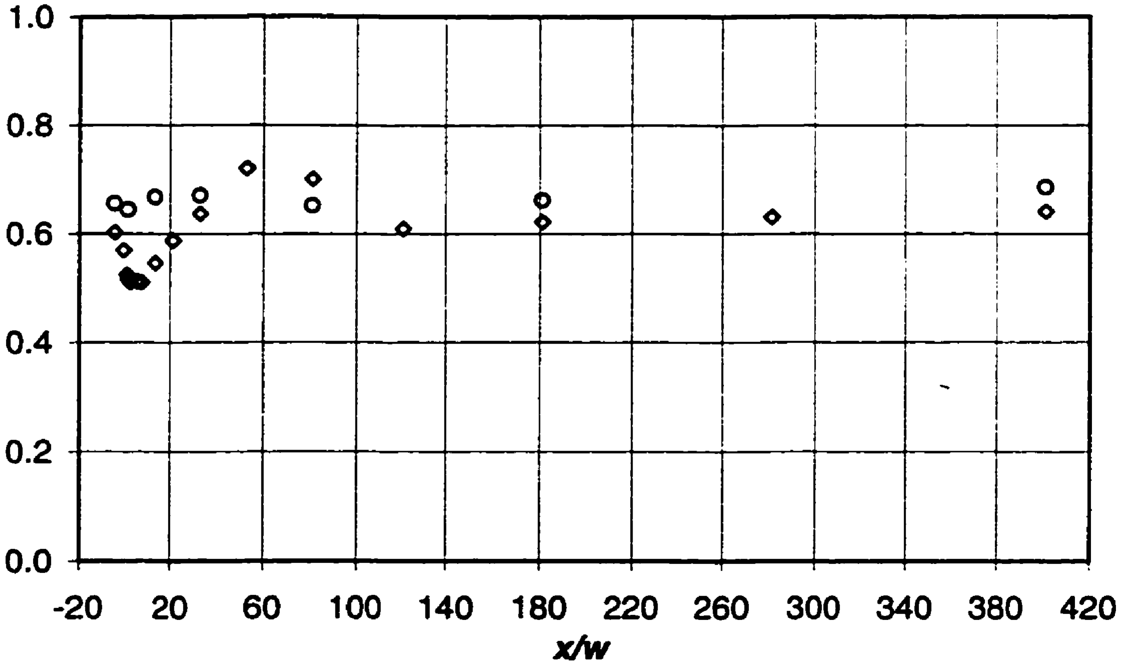

Figure 5.5.2 Wake parameter (π) distribution on the smooth- and grooved-wall at R_w = 1774. Symbols: ○, smooth-wall; ◇, grooved-wall;

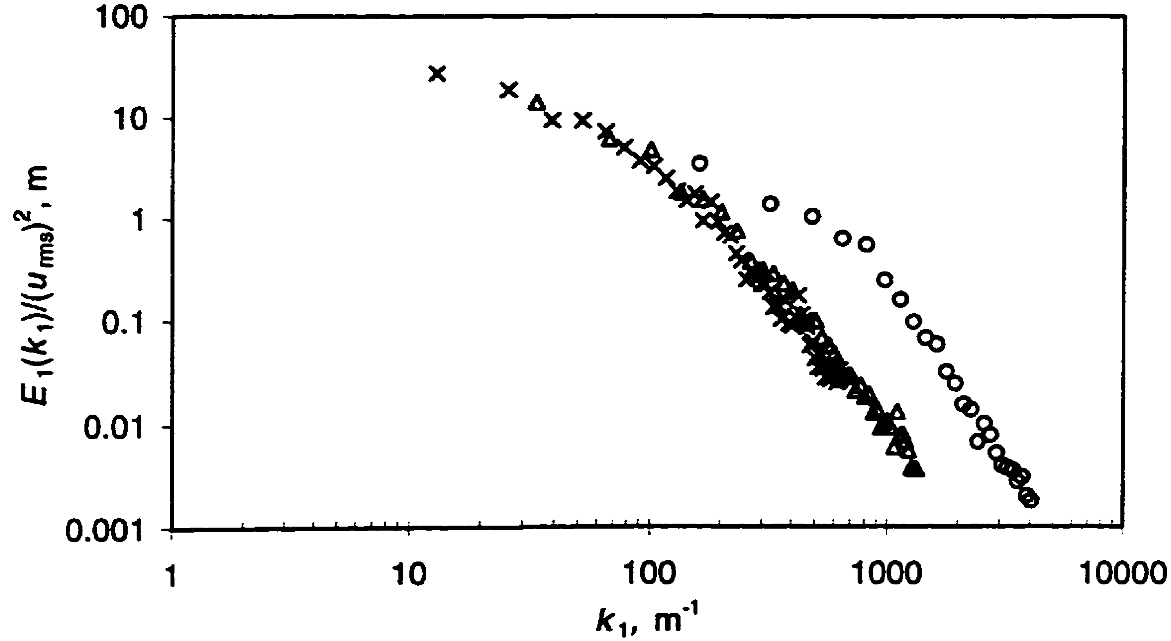

Figure 5.6.1 Energy spectra of the streamwise velocity fluctuation at $R_w = 645$. Symbols: ×, $y/\delta = 0.810$; Δ, $y/\delta = 0.020$; ○, $y/\delta = 0.004$;

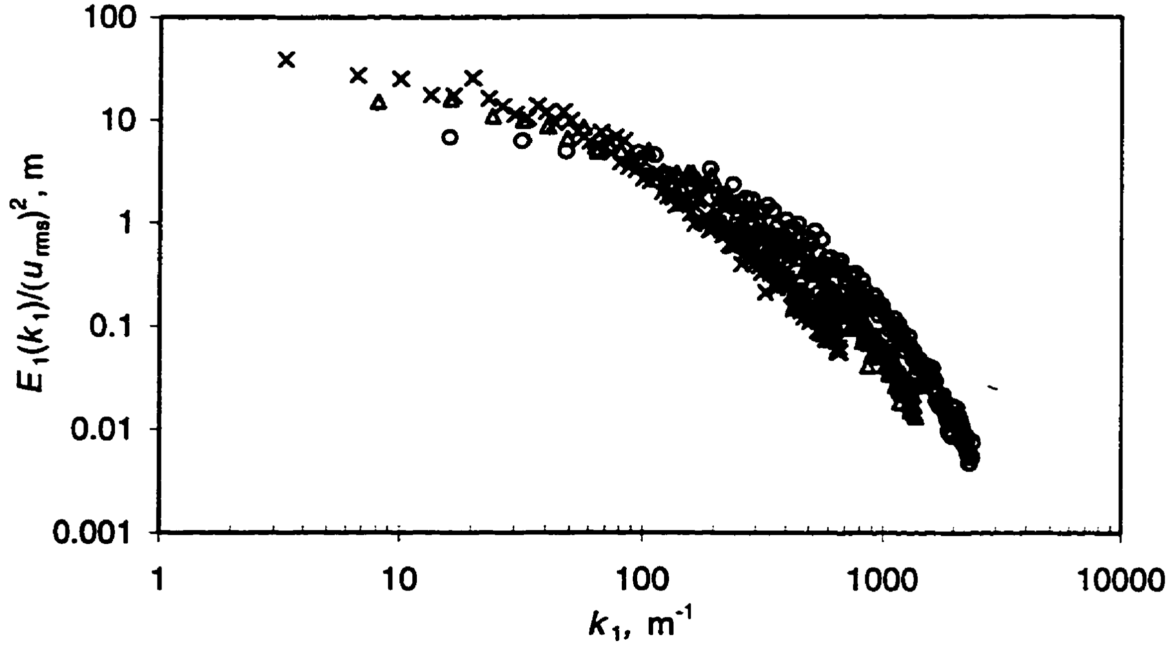

Figure 5.6.2 Energy spectra of the streamwise velocity fluctuation at $R_w = 1774$. Symbols: ×, $y/\delta = 0.880$; Δ, $y/\delta = 0.011$; ○, $y/\delta = 0.003$;

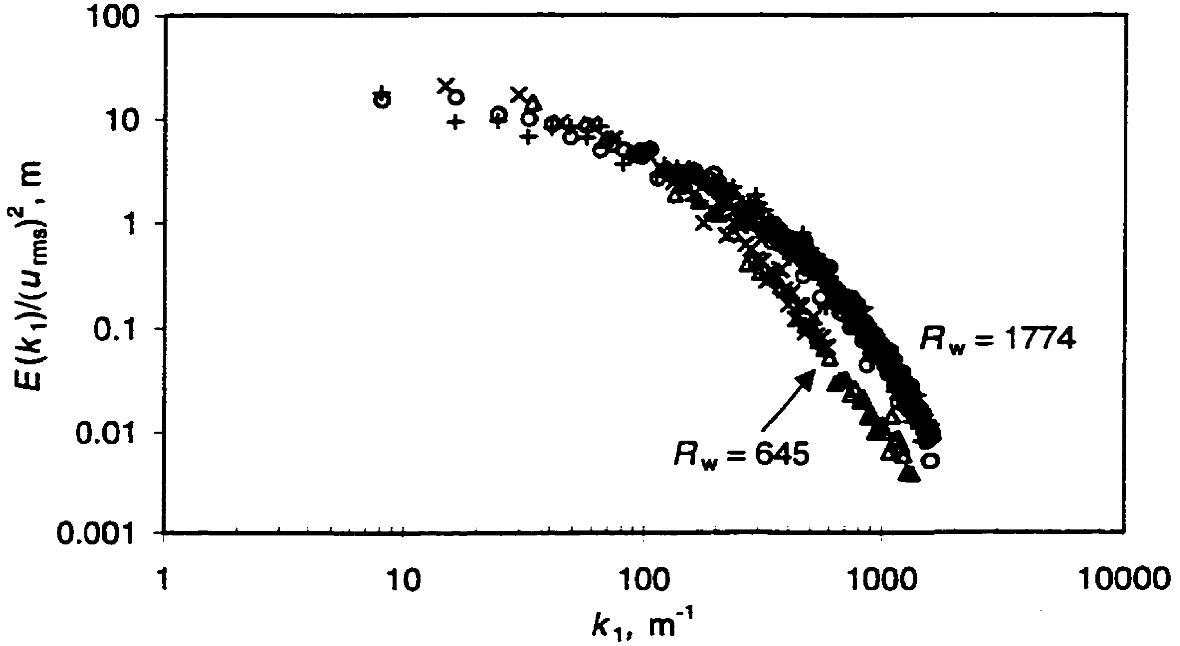

Figure 5.6.3 Energy spectra of the streamwise velocity fluctuation at x/w =1, and $y^+ \approx 13$. Symbols: At R_w = 645, △, smooth-wall; ×, grooved-wall; at R_w = 1774, ○, smooth-wall; +, grooved-wall.

At R_w = 645, there is a significant difference in $\varepsilon/(U_\infty)^2$ on the smooth- and grooved-wall. The peak values of $\varepsilon/(U_\infty)^2$ on the smooth- and grooved-wall are about 0.17 /s and 0.12 /s, respectively. At the lower R_w, $(\varepsilon/(U_\infty)^2)_{max}$ occurs at y^+ about 2.0 and 4.0 for the smooth- and grooved-wall, respectively.

At R_w = 1774, there is a good collapse of the grooved- and smooth-wall $\varepsilon/(U_\infty)^2$ data throughout the layer. At the higher R_w, $(\varepsilon/(U_\infty)^2)_{max} \approx 0.18$ /s for the smooth- and grooved-wall, and occurs at $y^+ \approx 4.0$.

At R_w = 1774, there is good agreement in $\varepsilon/(U_\infty)^2$ for the smooth- and grooved-wall throughout the layer. On the contrary, at R_w = 645, there appears to be a big difference between the two for $y^+ \lesssim 200$. The reason for this is not clear at this moment.

At both R_w, the y^+ locations of $(\varepsilon/(U_\infty)^2)_{max}$ are closer to the wall than the y^+ locations of u^+_{max}.

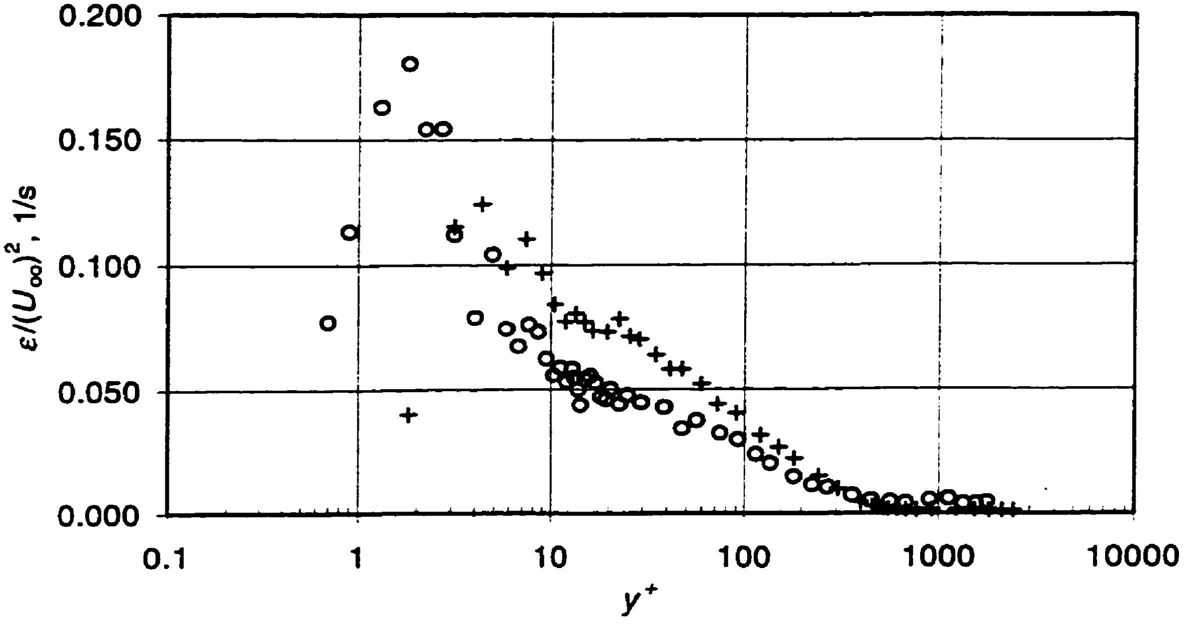

Figure 5.7.1 Rate of the turbulent kinetic energy distribution at R_w = 645. Symbols: o, smooth-wall; +, grooved-wall.

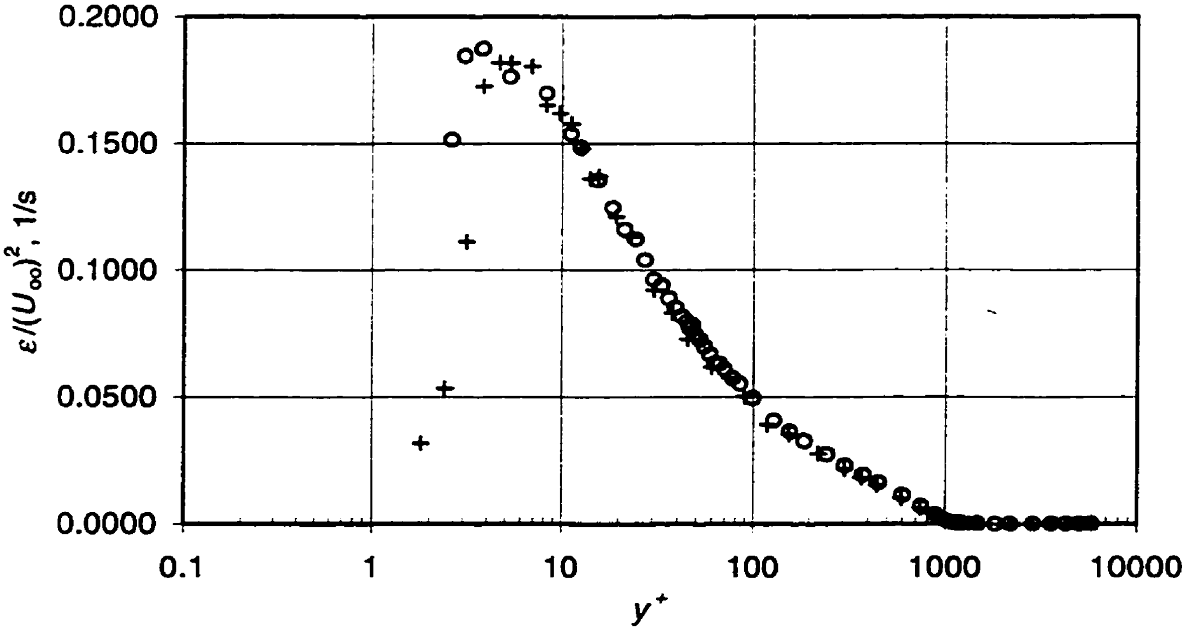

Figure 5.7.2 Rate of the turbulent kinetic energy distribution at R_w = 1774. Symbols: o, smooth-wall; +, grooved-wall.

5.8. Internal Layer Growth Downstream of the Cavity

The growth of the internal layer (δ_i) as a response of the turbulent boundary layer to the presence of the cavity is shown in Figure 5.8.1. The mean velocity profiles inside the internal layer near the step change are linear when plotted in the form U/U_∞ versus $y^{1/2}$ (Elavarasan et al. 1996). The height of the internal layer can be used to estimate the inner layer thickness. In the present study, the height of the internal layer was obtained using the '*knee*' method (Antonia and Luxton, 1971).

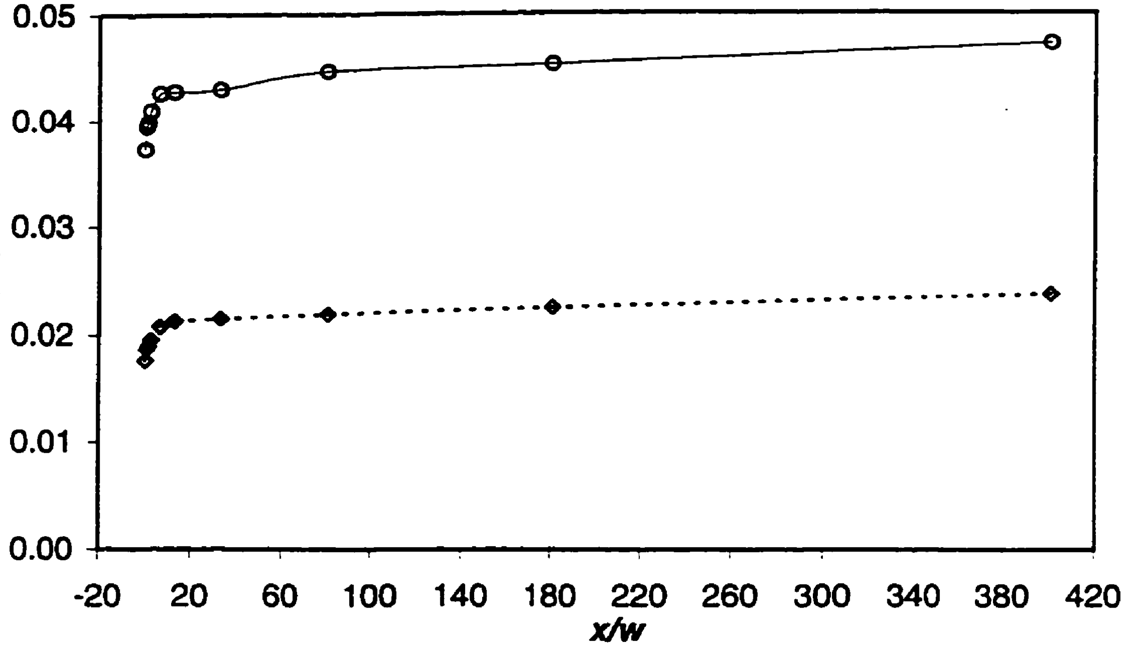

Figure 5.8.1 The internal layer growth on the grooved-wall at R_w = 645 and 1774: ○, R_w = 645; ◇, R_w = 1774. Lines are drawn only for convenience.

The height of the internal layer at $R_w = 645$ is approximately twice as high as that at $R_w = 1774$ (Figure 5.8.1). In the range $x/w \lesssim 7$, there is a rapid growth of the internal layers, however, the rate of growth of the two internal layers for $x/w \gtrsim 7$ is approximately the same. Beyond $x/w \approx 7$, the growth of the internal layers is rather slow. The rate of growth of the internal layer ($d\delta_i/dx$) is about 0.093 and 0.041 mm/mm at the lower and higher R_w, respectively, in the region $x/w \lesssim 7$. In the region $x/w \gtrsim 7$, ($d\delta_i/dx$) for both R_w is about the same at 0.00010 mm/mm.

The growth of the internal layers in the present study is compared to the data of Elavarasan et al. (1996) in Figure 5.8.2. The data are presented in a semi-logarithmic scale to enhance the region immediately downstream of the cavity. While there is a difference in the magnitude of the two layers, the rate of growth is approximately the same. The difference in the magnitude of the internal layers is primarily due to the difference in d/δ_1. In the present study, d/δ_1 is 0.072, while in the study of Elavarasan et al. d/δ_1 was 0.125.

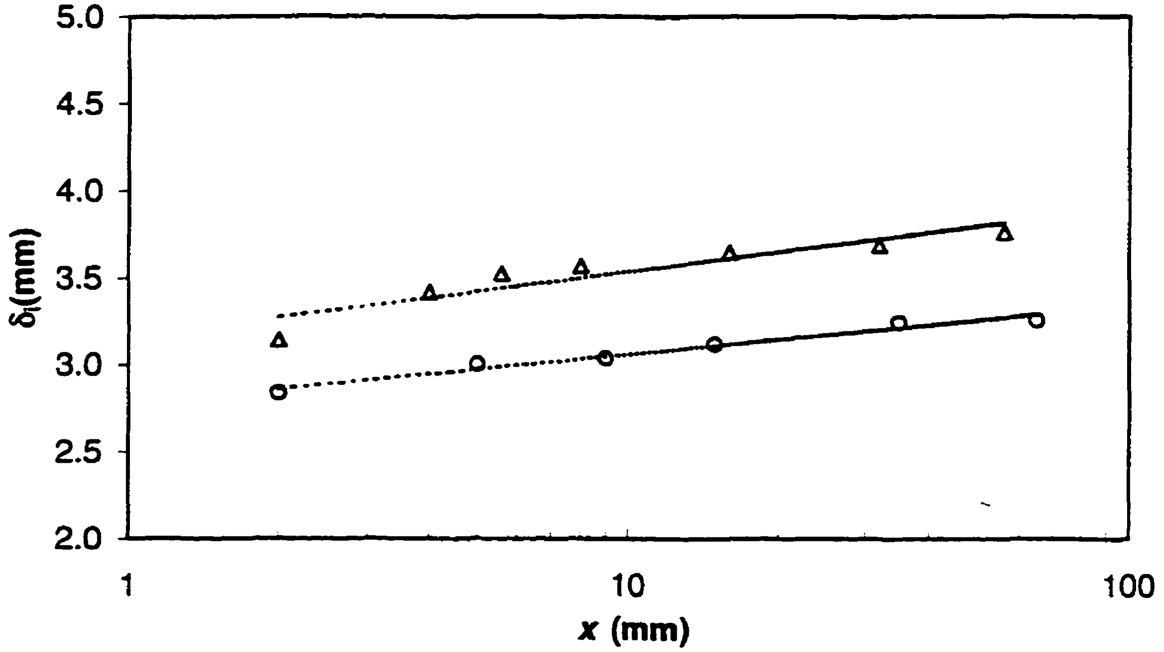

Figure 5.8.2 The internal layer growth on the grooved-wall. Symbols: ○, Current data (R_θ = 1000); △, data of Elavarasan et al. (1996, R_θ = 1300). The lines are plotted only for convenience.

5.9 X-Wire Measurement Results

Mean velocity, streamwise and wall-normal turbulence intensity profiles, and Reynolds shear stress obtained from X-wire measurements are presented in Figures 5.9.1 to 5.9.4. Representative data at two *x/w* locations on the smooth-wall are presented. The measurements were performed at $R_\theta \approx 1000$, which corresponds to a freestream velocity of 2 m/s. It is not possible to obtain near-wall data ($y \lesssim 1$mm or $y^+ \lesssim 6$), because of the probe size. In the present study, the X-wire measurements for the grooved-wall could not be obtained due to time constraints.

The U^+ and u^+ profiles from the X-wire are in very good agreement with the single-wire measurements and the DNS data, however, the wall-normal turbulence intensity and the Reynolds shear stress are lower than the DNS data. The peak values of v^+ and $-\overline{u^+v^+}$ are about 85% and 63%, respectively, of the DNS data ($R_\theta = 1410$).

There are several difficulties in measuring v^+ and $-\overline{u^+v^+}$ using X-wires. The wire separation and physical length of each sensor are important parameters for accurate measurements (Zhu and Antonia (1995); Ligrani and Bradshaw (1987); Elsner et al. (1993)). The X-wire measurements of Antonia et al. (1995) were also lower than the corresponding DNS data. In their study, $(v^+)_{max}$ and $(-\overline{u^+v^+})_{max}$ were approximately 76% and 68%, respectively, of the DNS data. The attenuation in v^+ is probably due to the angle of the instantaneous velocity vector exceeding the effective angle of the wire.

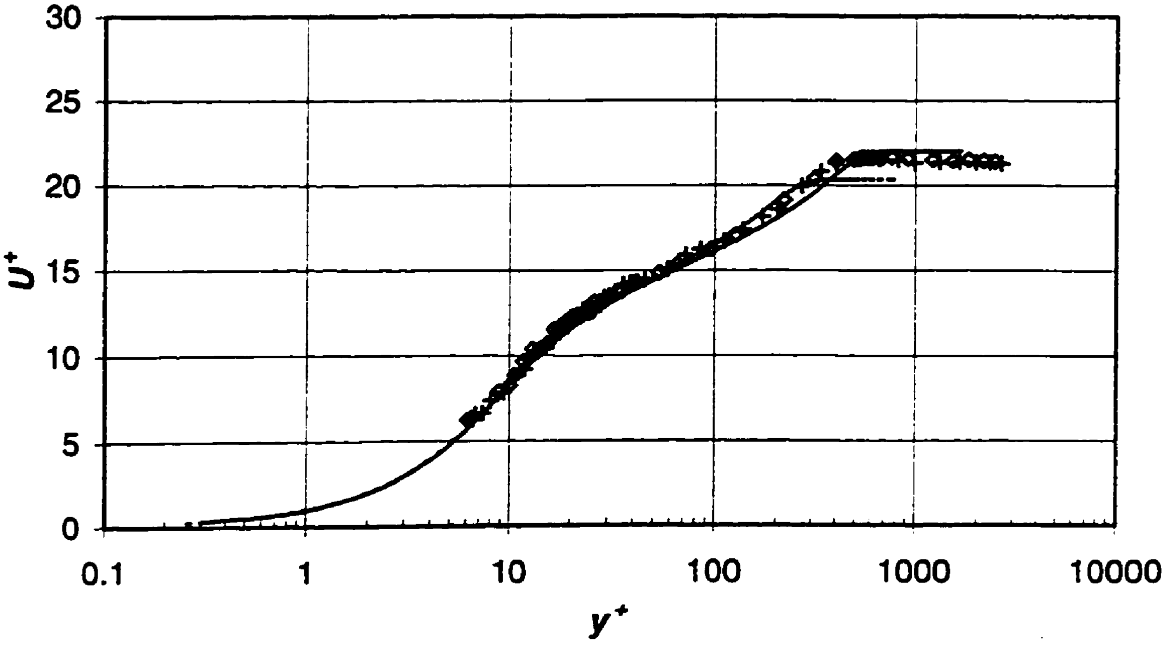

Figure 5.9.1 Streamwise mean velocity profiles obtained from X-wire measurements at R_w = 645. +, x/w = 13; ◇, x/w = 81; DNS: ——, (R_θ = 1410); - - - -, (R_θ = 670)

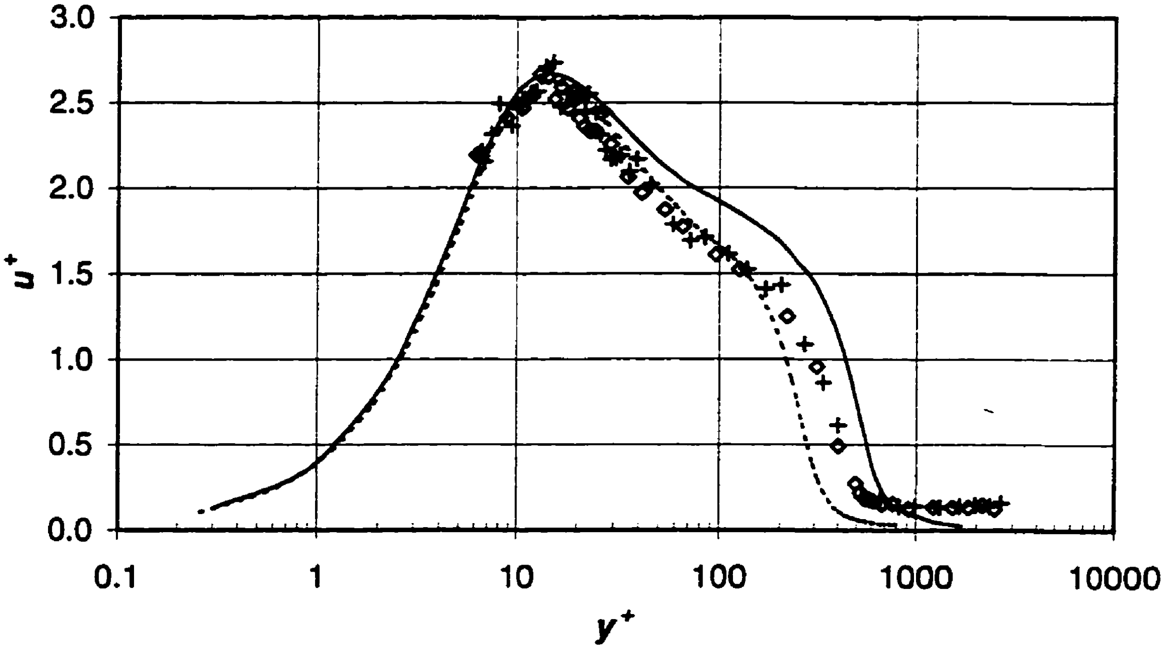

Figure 5.9.2 Streamwise turbulence intensity profiles obtained from X-wire measurements at R_w = 645. +, x/w = 13; ◇, x/w = 81; DNS: ——, (R_θ = 1410); - - - -, (R_θ = 670)

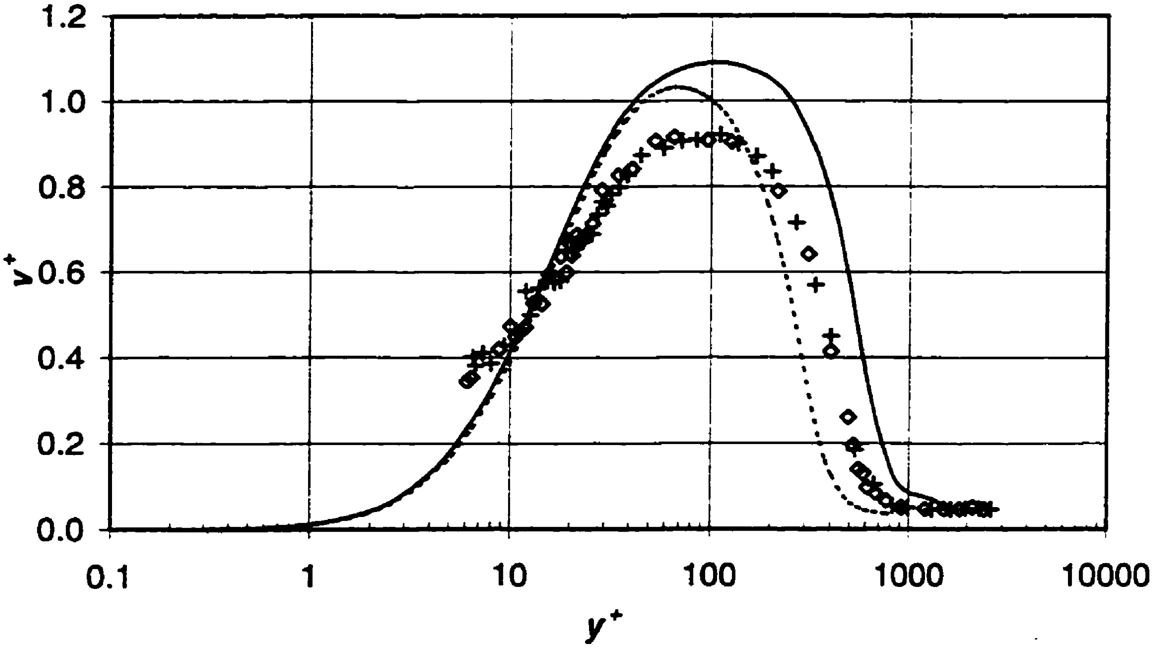

Figure 5.9.3 Wall-normal turbulence intensity profiles obtained from X-wire measurements at $R_w = 645$. +, $x/w = 13$; ◇, $x/w = 81$; DNS: ——, ($R_\theta = 1410$); - - - -, ($R_\theta = 670$)

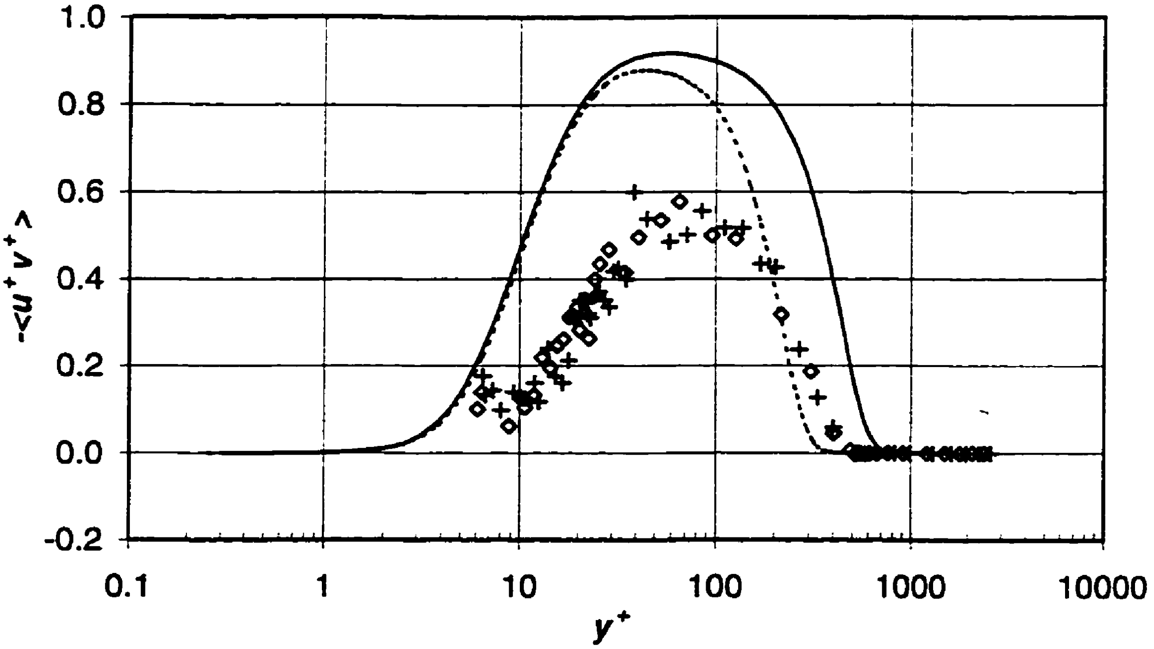

Figure 5.9.4 Reynolds shear stress obtained from X-wire measurements at $R_w = 645$.. +, $x/w = 13$; ◇, $x/w = 81$; DNS: ——, ($R_\theta = 1410$); - - - -, ($R_\theta = 670$); Note: - $\langle u^+v^+\rangle = -\overline{u^+v^+}$

Chapter 6

Concluding Remarks and Recommendations

6.1 Concluding Remarks

The development of a turbulent boundary layer downstream of a transverse square groove under a zero pressure gradient has been studied at two different R_w (645 and 1774). Experiments were performed in a low-speed wind tunnel using hot-wire anemometry. Single-normal and X-wires were used to obtain the velocity profiles and velocity fluctuations in the streamwise and wall-normal directions. The main purpose of this study is to examine the effect of the groove on the skin friction and turbulence structure. In addition, the wake parameter, power spectra, turbulent kinetic energy dissipation rate and the development of the internal layer downstream of the groove have been investigated.

At the lower R_w, the effect of the groove on C_f is insignificant. The maximum deviation of C_f on the grooved-wall from the smooth-wall is about 1% which is within the experimental uncertainty. At the higher R_w, the effect of the groove is more pronounced. There is an increase in C_f over the smooth-wall value immediately downstream of the groove until $x/w \approx 30$. This increase in C_f is followed by a decrease and a subsequent oscillatory relaxation back to the smooth-wall value. The decrease in C_f can be attributed to the weakening of the streamwise vortices due to the presence of the groove (Elavarasan et al., 1996). From this study, it can be concluded that d/δ_1 has a significant effect on the wall shear stress characteristics downstream of the groove. Qualitatively, the results for C_f at the higher R_w are similar to the results of Pearson et al.

(1997), however, the sharp rise in C_f of the current study is not as intense as in the study of Pearson et al.

It is difficult to make any conclusions on the overall drag due to the groove, but the distribution of C_f downstream of the groove suggests that surface drag reduction using a *d*-type roughness is possible. If the area under the overshoot (increase in C_f over the smooth-wall value) can be reduced, while the area under the undershoot (decrease in C_f below the smooth-wall value) is increased, a total surface drag reduction could be achieved (Ching and Parsons, 1998).

The mean velocity profiles are not affected by the presence of the groove at both R_w. The ratio d/δ_1 is probably too small to alter the mean velocity profiles. The streamwise turbulence intensity is reduced over the grooved-wall in the inner region ($y^+ \lesssim 10$) at both R_w. The cavity attenuates the turbulence intensity in this region. At $R_w = 1774$, this effect is limited to the near-wall region. In the outer region ($y^+ \gtrsim 10$), there is a good collapse of the turbulence intensity profiles between the smooth- and the grooved-wall. However, at $R_w = 645$, u^+_{max} is slightly affected by the presence of the groove. There is a decrease in u^+_{max} of about 4% on the grooved-wall. The location of u^+_{max} remains unchanged at $y^+ \approx 13$ for both the smooth- and grooved-wall at the two R_ws.

The wake parameter (π) distribution indicates that the boundary layers over the smooth- and grooved-wall are not in equilibrium as characterized by Rotta (1962). There is a strong correlation between π and C_f distributions at $R_w = 1774$. This correlation is similar to that obtained by Matsumoto (1994), where π increases as C_f decreases.

There is no significant effect of the groove on the energy spectra, at least at the location where the turbulence intensity is maximum. The effect of R_w on the spectrum is to increase the high wave number component of energy, and to reduce the low wave number component as R_w increases.

In the present study, the effect of the groove on the skin friction, mean velocity, turbulent intensity, and energy spectra is less pronounced compared with the studies of Pearson et al. (1997), Elavarasan et al. (1996), and Choi and Fujisawa (1993). This difference may be attributed to the difference in d/δ_1 of the present study and the previous three studies. In the present study, $d/\delta_1 = 0.072$, while in the previous three studies, $d/\delta_1 =$ 0.17, 0.125, and 0.4, respectively. It can be conjectured that $d/\delta_1 \approx 0.1$ for the groove to have a significant effect on the turbulent boundary layer.

At $R_w = 645$, the peak values of the turbulent kinetic energy dissipation, $\varepsilon/(U_\infty)^2$, on the grooved- and smooth-walls are about 0.12 and 0.17 /s, respectively. While there is good agreement in $\varepsilon/(U_\infty)^2$ for the smooth- and grooved-wall throughout the layer at $R_w =$ 1774, there is a significant difference between the two at $R_w = 645$. The reason for this is not clear at this moment. At both R_w, the y^+ location of $\varepsilon/(U_\infty)^2_{max}$ is closer to the wall than the y^+ location of u^+_{max}.

The height of the internal layer at the lower R_w is approximately twice that at the higher R_w. The internal layer grows rapidly immediately downstream of the cavity. $(d\delta_i/dx)$ is about 0.093 and 0.041 mm/mm for $x/w \lesssim 7$ at the lower and higher R_w, respectively. Beyond $x/w \approx 7$, the growth of the internal layer is much slower at both R_ws.

6.2 Recommendations

It is recommended that further X-wire measurements using a smaller probe (miniature X-wire probe) be performed. This would provide information on v^+ and $-\overline{u^+v^+}$

in the near-wall region, and lead to an improved understanding of the turbulent structure in the vicinity of the groove.

The present hot-wire traverse is manually controlled, and a computer controlled traverse is highly desirable. This will improve the accuracy of the measurement of probe locations, and facilitate performing the experiments.

Near-wall measurement with hot-wires is very difficult because of the wall conduction. Laser Doppler Anemometry (LDA) can be used to overcome this problem. Very accurate measurements in the near-wall region have been obtained using LDA (Djenidi and Antonia (1993); Djenidi et al (1994)). This will also allow the wall shear stress to be obtained directly from the mean velocity gradient very close to the wall.

Experiments using a slightly larger d/δ_1 are recommended. This will allow one to determine if an optimum d/δ_1 can be obtained to increase the undershoot in C_f downstream of the groove. The effect of different groove shapes on the turbulent boundary layer needs to be investigated (Figure 6.2.1). While keeping the basic dimensions of the groove (d and w) constant, groove shapes suggested in Figure 6.2.1 can be investigated. This may potentially reduce the intense favorable pressure gradient that emanates from the downstream edge of the groove and reduce the sharp rise in C_f immediately downstream of the groove.

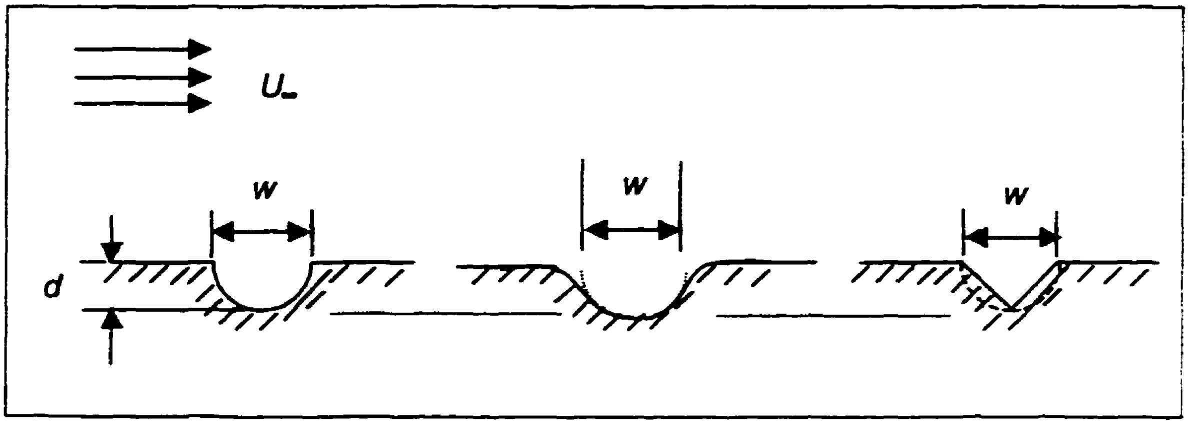

Figure 6.2.1 Alternative groove shapes

References

1. Andreopoulus, J. and Wood, D. H. (1982), The Response of a Turbulent Boundary Layer to a Short Length of Surface Roughness, *J. Fluid Mech.*, Vol. **118**, pp. 143-164
2. Antonia, R. A. and Luxton, R. E. (1971), The Response of a Turbulent Boundary Layer to a Step Change in Surface Roughness: Part 1, Smooth to Rough, *J. Fluid Mech.*, Vol. **48**, part 4, pp. 721-761
3. Antonia, R. A. and Luxton, R. E. (1972), The Response of a Turbulent Boundary Layer to a Step Change in Surface Roughness: Part 2, Rough to Smooth, *J. Fluid Mech.*, Vol. **53**, part 4, pp. 737-757
4. Antonia, R. A., (1993), Direct numerical simulations and hot wire experiments: A Possible Way Ahead?, in *New Approaches and Concepts in Turbulence* (eds. Th. Dracos and A. Tsinober), pp. 349-365, Birkh ä user Verlag, Basel, Switzerland
5. Antonia, R. A. (1994), The Effect of Different Types Surfaces Conditions on a Turbulent Boundary Layer, *First International Conference on Flow Interaction*, Hong Kong
6. Antonia, R. A., Zhu, Y., and Sokolov, M., (1995), Effect of concentrated wall suction on a turbulent boundary layer, *Phys. Fluids*, Vol. 7(10), pp. 2465-2474
7. Bandyopadhyay, P. R. (1986), Drag reducing outer-layer devices in rough-wall turbulent boundary layers, *Experiments in Fluids*, Vol. **4**, pp. 247-256
8. Barenblatt, G. I. (1993), Scaling Laws for Fully Developed Shear Flows. Part 1. Basic Hypotheses and Analysis, *J. Fluid Mech.*, Vol. **248**, pp. 521-529
9. Barenblatt, G. I. and Protokishin, V. M. (1993), Scaling Laws for Fully Developed Shear Flows. Part 2. Processing of Experimental Data, *J. Fluid Mech.*, Vol. **248**, pp. 513-520
10. Bechert, D. W.(1995), Calibration of Preston Tube, *AIAA Journal*, Vol. **34**, No: 1, pp. 205-206
11. Bendat, J. S. and Piersol, A. G., (1971), *Random Data: Analysis and Measurement Procedures*, Wiley-Interscience, John Wiley & Sons, Inc., New York
12. Bradshaw, P., (1971), *An Introduction to Turbulence and Its Measurement*, 1st edition, Pergamon Press, Oxford
13. Browne, L. W. B, Antonia, R. A., and Chua, L. P., (1989) Calibration of X-probes for Turbulent Flow Measurements, *Experiments in Fluids*, Vol. **7**, pp. 201 – 208
14. Bruun, H. H., Nabhani, N., Al-Kayiem, H. H., Fardad, A. A., Khan, M. A., and Hogarth, E.,(1990a), Calibration and analysis of X hot-wire probe signals, *Meas. Sci. Technol.*, Vol. **1**, pp. 782-785
15. Bruun, H. H., Nabhani, N., Fardad, A. A., and Al-Kayiem, H. H.,(1990b), Velocity components measurements by X hot-wire anemometry, *Meas. Sci. Technol.*, Vol. **1**, pp 1314-1321
16. Bruun, H. H. (1995), *Hot-Wire Anemometry: Principles and Signal Analysis*, Oxford University Press, Oxford
17. Carpenter, P.(1997), The right sort of roughness, *Nature*, Vol. **388**, pp. 713-714

18. Cary, A. M., Weinstein, L. M. and Bushnell, D. M., (1980), Drag Reduction Characteristics of Small Amplitude Rigid Surface Waves, in *Progress in Astronautics and Aeronautics*, (ed. Gary R. Haugh), Vol. **72**, pp. 143-167
19. Cebeci, T. and Smith, A. M. O., (1974), *Analysis of Turbulent Boundary Layers*, 1st edition, Academic Press, New York
20. Ching, C.Y., Djenidi, L., and Antonia, R.A. (1995a), Low-Reynolds-number Effects in a Turbulent Boundary Layer, *Experiments in Fluids*, Vol. **19**, pp. 61-68
21. Ching, C. Y., Elavarasan, R., and Antonia, R.A. (1995b), Visualization of Near Wall Region in a Turbulent Boundary Layer Over a *d*-Type Roughness, *7th International Symposium on Flow Visualization*, Seatle
22. Ching, C.Y. and Parsons, B.L., (1998), Drag characteristics of a turbulent boundary layer over a flat plate with transverse square grooves, *Experiments in Fluids*, (to be published)
23. Choi, K. S., Fujisawa, N., and Savill, A. M. (1989), Studies of Drag Reduction *d*-Type Roughness - Including Flow Visualization, Image Enhancement and Quantitative Measurements. In Reznicek, R. (ed.), *Flow Visualization V*, Hemisphere, New York
24. Choi, K.-S. and Fujisawa, N. (1993), Possibility of Drag Reduction Using *d*-type Roughness, *Applied Scientific Research*, Vol. **50**, pp. 315-324
25. Clauser, F. H., (1954), Turbulent Boundary Layer in Adverse Pressure Gradient, *Journal of Aeronautical Sciences*, Vol. **21**, pp. 91-108
26. Clauser, F. H.(1956), The Turbulent Boundary Layer, *Advances in Applied Mechanics*, Vol. **4**, pp. 1-51, Academic Press, New York
27. Coles, D. (1956), The Law of The Wake in The Turbulent Boundary Layer, *J. Fluid Mech.*, Vol. **1**, pp.191-226.
28. Coustols, E. and Savill, A. M., (1991), Turbulent Skin Friction Drag Reduction by Active and Passive Means. Special Course on Skin Friction Drag Reduction, *AGARD Report*, Vol.**786**, pp. 8.1-8.80
29. Djenidi, L. and Antonia, R. A., (1993), LDA measurements in low Reynolds number turbulent boundary layer, *Experiments in Fluids*, Vol. **14**, pp. 280-288
30. Djenidi, L., Anselmet, F., and Antonia, R.A. (1994), LDA Measurements in Turbulent Boundary Layer over a *d*-type Rough Wall, *Experiments in Fluids*, Vol. **16**, pp. 323-329
31. Djenidi, L. And Antonia, R. A., (1995), LDA measurements: Power spectrum estimation, *DANTEC Information*, No. **14**, pp. 12 - 15
32. Djenidi, L., Dubief, Y., and Antonia, R.A. (1997), Advantages of Using a Power Law in a Low R_θ Turbulent Boundary Layer, *Experiments in Fluids*, Vol. **22**, pp. 348-350
33. Elavarasan, R., Ching, C.Y., and Antonia, R.A. (1996), Turbulent Boundary Layer over a Smooth Wall with Widely Separated Transverse Square Cavities, *Applied Scientific Research*, Vol. **55**, pp. 227-243
34. Elliott, W. P. (1958), *Trans. Am. Geophys.*, Union, **39**, 1048
35. Elsner, J.W., Domagala, P., and Elsner, W.,(1993), Effect of finite spatial resolution of hot-wire anemometry on measurements of turbulence energy dissipation, *Meas. Sci. Technol.*, Vol. **4**, pp. 517-523

36. Gatski, T. B., Sarkar, S., and Speziale, C. G., (1992), *Studies in Turbulence*, Springer-Verlag, New York.
37. Goldstein, R. J.,(1983), *Fluid Mechanics Measurements*, Hemisphere Publishing Corporation, Washington
38. Granger, R.A., (1988), *Experiments in Fluid Mechanics*, First Edition, Holt, Rinehart and Winston, Inc., New York
39. Haugen, R. L., Dhanak, A. M. (1966), Momentum Transfer in Turbulent Separated Flow Past a Rectangular Cavity, *J. App. Mech.*, Vol. **33**, pp. 641-646
40. Haugh, G. R. (1980), Viscous Drag Reduction, *Progress in Astronautics and Aeronautics*, Vol. 72, AIAA
41. Head, M. R. and Ram, V. (1971), Simplified Presentation of Preston Tube Calibration, *Aeronautical Quarterly*, Vol. **22**, pp. 295-300
42. Head, M. R. and Bandyopadhyay, P., (1981), New aspects of turbulent boundary layer structure, *J. Fluid Mech.*, Vol. **107**, pp. 297-338
43. Hefner, J. N., Weinstein, L. M., and Bushnell, D. M., (1980), Large-Eddy Breakup Scheme for Turbulent Viscous Drag Reduction, in *Progress in Astronautics and Aeronautics*,(ed. Gary R. Haugh), Vol. **72**, pp. 110-127
44. Hefner, J. N., and Bushnell, D. M., (1984), Turbulent boundary layer relaxation with application to skin-friction drag reduction, *AIAA Journal*, Vol. **22**(7), pp. 871-872
45. Hinze, J. O., (1975), *Turbulence*, second edition, McGraw-Hill, New York
46. Hu T. F. And Hsu, Y. Y. (1994), A probe manipulator for wind tunnel experiments, *Meas. Sci. Technol.*, Vol. **5**, pp. 829-834
47. Johansson, A.V. and Alfredsson, P.H. (1983), Effects of imperfect spatial resolution on measurements of wall-bounded turbulent shear flows, *J. Fluid Mech.*, Vol. **137**, pp. 409-421
48. Khoo, B. C., Chew, Y. T., and Li, L.(1997), Effects of Imperfect Spatial Resolution on Turbulence Measurements in the Very near-Wall Viscous Sublayer Region, *Experiments in Fluids*, Vol. **22**, pp. 327-335
49. Klebanoff, P. S.,(1955), Characteristics of turbulence in a boundary layer with zero pressure gradient, *NACA Rep.* 1247
50. Lekakis, I (1996), Review Article : Calibration and Signal Interpretation for Single and Multiple Hot-Wire/Hot-Film Probes, *Meas. Sci. Technol.*, Vol. **7**, pp. 1313-1333
51. Ligrani, P. M. and Bradshaw, P. (1987), Subminiature hot-wire sensors: development and use, *J. Phys. E: Sci. Instrum.*, Vol. **20**, pp. 323-332
52. Matsumoto, A.,(1994), Some Features of Turbulent Boundary Layers over Grooved Rough Walls, *Transc. of The Japan Soc. for Aeronautical and Space Sc.*, Vol. **37**, No. 115, pp. 27-41.
53. Mochizuki, S. and Nieuwstadt, F. T. M. (1996), Reynolds-number Dependence of the Maximum in the Streamwise Velocity Fluctuations in Wall Turbulence, *Experiments in Fluids*, Vol. **21**, pp. 218-226, Springer-Verlag
54. Munson, B. R., Young, D. F., and Okiishi, T. H., (1990), *Fundamentals of Fluid Mechanics*, First edition, John Wiley & Sons, New York
55. Nikuradse. J. (1933), Stromungsgesetze in rauhen Rohren, Forchg., Arb. Ing. Wes. No. 361

56. Osaka, H. and Mochizuki, S. (1988), Coherent structure of a *d*-type rough wall boundary layer, in Transport Phenomena, in H. Hirata and N. Kasagi (eds.) *Turbulent Flows: Theory, Experiments and Numerical Simulations*, Hemisphere, New York, pp. 199-211
57. Osaka, H. and Mochizuki, S. (1991), Turbulent drag reduction of a *d*-type rough wall boundary layer with longitudinal thin ribs placed within the transverse cavities, In *Recent Developments in Turbulent Management*, (ed. K. S. Choi), Dordrecht, Kluwer, Academic Publishers
58. Patel, V. C.(1965), Calibration of the Preston Tube and Limitations on Its Use in Pressure Gradients, *J. Fluid Mech.*, Vol. **23**, part I, pp. 185-208
59. Pearson, B. R., Elavarasan, R., and Antonia, R. A. (1995), The Effect of a Square Groove on a Boundary layer, *Twelfth Australasian Fluid Mechanics Conference*, The University of Sydney, pp. 477-480
60. Pearson, B. R., Elavarasan, R., and Antonia, R. A. (1997), The Response of a turbulent boundary layer to a Square Groove, *J. Fluids Engg.*, Vol. **119**, pp. 466-469
61. Perry, A. E., Schofield, W. H., and Joubert, P. N. (1969), Rough Wall Turbulent Boundary Layers, *J. Fluid Mech.*, Vol. **37**, part 2, pp. 383-413
62. Perry, A. E. And Abbel, C. J., (1975), Scaling laws for pipe-flow turbulence, *J. Fluid Mech.*, Vol. **67**, part 2, pp. 257 - 271
63. Preston, J. H. (1954), The Determination of Turbulent Skin Friction by Means of Pitot Tubes, *J. of the Royal Aeronautical Society*, Vol. **14**, pp. 109-121
64. Purtell, L. P., Klebanoff, P. S., and Buckley, F. T., (1981), Turbulent boundary layer at low Reynolds number, *Phys. Fluids*, Vol. **24**(5), pp. 802-811
65. Richardson, L. F. (1922), *Weather Prediction by Numerical Process*, Cambridge University Press, England
66. Robinson, S. K. (1991), Coherent Motions in the Turbulent Boundary Layer, *Ann. Rev. Fluid Mech.*, Vol. **23**, pp. 601-639
67. Roshko, A. (1955), Some Measurements of Flow in a Rectangular Cut-out, *NACA Technical Note*, No. **3488**
68. Rotta, J.C.(1962), Turbulent boundary layers in incompressible flow, in *Progress in Aeronautical Sciences*, (A. Ferri, D. Kuchemann, and L.H.G. Sterne (eds)), Vol. **2**, Pergamon Press, New York, pp. 1-219
69. Schetz, J. A., (1993), *Boundary Layer Analysis*, 1st edition, Prentice-Hall Inc., New Jersey
70. Schlichting, H., (1979), *Boundary Layer Theory*, 7th edition, McGraw-Hill Book Company, New York
71. Sherman, F. S., (1990), *Viscous Flow*, 1st edition, McGraw-Hill Publishing Company, New York
72. Sirovich, L. and Karlsson, S.(1997), Turbulent drag reduction by passive mechanism, *Nature*, Vol. **388**, pp. 753-755
73. Smits, A.J. and Wood, D.H.,(1985), The response of turbulent boundary layers to sudden perturbations, *Ann. Rev. Fluid Mech.*, Vol. **17**, pp. 321-358
74. Spalart, P. R.(1988), Direct Simulation of a Turbulent Boundary Layer up to R_θ = 1410, *J. Fluid Mech.*, Vol. **187**, pp. 61-98

75. Tani, I., Iuchi, M., and Komoda, H. (1961), Experimental investigation of flow separation associated with a step or groove, *Aero. Res. Inst.*, Univ. Tokyo, 363
76. Tani, I. (1987a), Equilibrium, or non-equilibrium, of turbulent boundary layer flows, *Proc. Japan Acad.*, **63**, Seri B, pp. 96 – 100
77. Tani, I.,(1987b), Turbulent boundary layer development over rough surfaces, in *Perspectives in Turbulent Studies* (H. U. Meier and P. Bradshaw, eds), Berlin, Springer, pp. 223-249
78. Tani, I., Munakata, H., Matsumoto, A., and Abe, K. (1987), Turbulence management by groove roughness, in *Turbulence Management and Relaminarisation*, (H. W. Liepmann and R. Narasimha, eds.), IUTAM Symposium, Bangalore, India, pp. 161-172
79. Taylor, G. I. (1935), The transport of vorticity and heat through fluids in turbulent motion, *Proceedings of Royal Society of London*, Series A, Vol. **135**, pp. 685
80. Taylor, R.P, Taylor, J.K, Hosni, M.H, and Coleman, H.W.(1993), Relaxation of the turbulent boundary layer after an abrupt change from rough to smooth wall, *J. Fluids Engg.*, Vol. **115**, pp. 379-382
81. Tennekes,H. and Lumley, J.L.,(1972), *A First Course in Turbulence*, first edition, The MIT Press, Cambridge
82. Townsend, A.A, (1956), *The Structure of Turbulent Shear Flow*, Cambridge University Press
83. Townsend, A.A.(1965), Self-preserving flow inside a turbulent boundary layer, *J. Fluid Mech.*, Vol. **22**, pp. 773-797
84. Walsh, M. J.,(1980), Drag Characteristics of V-Groove and Transverse Curvature Riblets, in *Progress in Astronautics and Aeronautics*, (ed. Gary R. Haugh), Vol. **72**, pp. 168-184
85. Walsh, M.J. and Lindermann, A.M. (1984), Optimization and Application of Riblets for Turbulent Drag Reduction, *AIAA Paper* **84**, -0347
86. Walsh, M. J. (1990), Viscous Drag Reduction in Boundary Layers, in *Progress in Astronautics and Aeronautics*, (eds. D. M. Bushnell and J. N. Hefner), Vol. **123**, pp. 203-261
87. White, F. M., (1986), *Fluid Mechanics*, second edition, McGraw-Hill, Inc., New York
88. White, F. M., (1991), *Viscous Fluid Flow*, second edition, McGraw-Hill, Inc., New York
89. Wood, D. H. and Antonia, R. A., (1975), Measurements in a turbulent boundary layer over *d*-type surface roughness, *J. App. Mech.*, Vol. **42**, pp. 591-597
90. Yuan, S.W., (1988), *Foundation of Fluid Mechanics*, S.I. Unit Ed., Third Edition, Prentice-Hall of India, New Delhi
91. Zagarola, M.V. and Smits, A. J., (1997), Scaling of the mean velocity profile for turbulent pipe flow, *Phys. Rev. Letters*, Vol. **78**(2), pp. 239-242
92. Zagarola, M. V., Perry, A. E., and Smits, A. J., (1997), Log laws or power laws: The scaling in the overlap region, *Physics of Fluids*, Vol. **9**, no. 7, pp. 2094-2100
93. Zhu, Y. and Antonia, R. A., (1995), Effects of Wire separation on X-probe measurements in a turbulent flow, *J. Fluid Mech.*, Vol. **287**, pp. 199-223

Appendices

A: Program Listings

A1: Program listing to analyze SN-wire data

```
*************************************************************
clear

% MEAN AND RMS CALCULATION +++

load ps_0831              % Third order polynomial constants

% generate sequence of file names, velocity at a certain
% distance off the wall

file = ['s400_0.dat';
       's300_0.dat';
       's200_0.dat';
       's150_0.dat';
       's100_0.dat';
       's090_0.dat';
       's080_0.dat';
       's070_0.dat';
       's060_0.dat';
       's055_0.dat';
       's050_0.dat';
       's045_0.dat';
       's040_0.dat';
       's035_0.dat';
       's030_0.dat';
       's027_5.dat';
       's025_0.dat';
       's022_5.dat';
       's020_0.dat';
       's019_0.dat';
       's018_0.dat';
       's017_0.dat';
       's016_0.dat';
       's015_0.dat';
       's014_0.dat';
       's013_0.dat';
       's012_0.dat';
       's011_0.dat';
       's010_0.dat';
       's009_0.dat';
```

```
        's008_0.dat';
        's007_0.dat';
        's006_0.dat';
        's005_0.dat';
        's004_0.dat';
        's003_5.dat';
        's003_0.dat';
        's002_5.dat';
        's002_0.dat';
        's001_5.dat';
        's001_0.dat';
        's000_9.dat';
        's000_8.dat';
        's000_7.dat';
        's000_6.dat';
        's000_5.dat';
        's000_4.dat';
        's000_3.dat';
        's000_2.dat';
        's000_1.dat';
        's000_0.dat';];

for n=1:size(file,1);                       % file incrementer
    fid       = fopen(file(n,1:size(file,2)),'r');
    data      = fscanf(fid, '%i %i', [1, inf]);
    ndata_1   = data(1,:);
    u         = polyval(ps_0831,ndata_1);
    u_mean(n)= mean(u(1,1:size(u,2)));
    u_prime   = u-u_mean(n);
    clear data ndata_1;
    fclose(fid);

    u_rms(n)   = 0;
       for m   = 1:size(u,2);
          u_rms(n)  = u_rms(n)+(u_prime(m))^2;
       end;
   u_rms(n)  = (u_rms(n)/size(u,2))^0.5;
    fclose(fid);

    clear u;                            % make some room
end;                                    % repeat for every file

clear n m fid file fsaved;              % tidy up

************************************************************
```

A2: Program listing to analyze X-wire data

```
****************************************************************
clear

% MEAN AND RMS CALCULATION +++

  load px0917_1;  % Third order polynomial constants for
                  % wire 1
  load px0917_2;  % Third order polynomial constants for
                  % wire 2

% generate sequence of file names, velocity at a certain
% distance from the wall

file = [  'x400_0.dat';
          'x300_0.dat';
          'x200_0.dat';
          'x150_0.dat';
          'x100_0.dat';
          'x090_0.dat';
          'x080_0.dat';
          'x070_0.dat';
          'x060_0.dat';
          'x055_0.dat';
          'x050_0.dat';
          'x045_0.dat';
          'x040_0.dat';
          'x035_0.dat';
          'x030_0.dat';
          'x027_5.dat';
          'x025_0.dat';
          'x022_5.dat';
          'x020_0.dat';
          'x018_0.dat';
          'x017_0.dat';
          'x016_0.dat';
          'x015_0.dat';
          'x014_0.dat';
          'x013_0.dat';
          'x012_0.dat';
          'x011_0.dat';
          'x010_0.dat';
          'x009_0.dat';
          'x008_0.dat';
          'x007_0.dat';
```

```
          'x006_0.dat';
          'x005_0.dat';
          'x004_0.dat';
          'x003_5.dat';
          'x003_0.dat';
          'x002_5.dat';
          'x002_0.dat';
          'x001_5.dat';
          'x001_0.dat';
          'x000_9.dat';];

tteta_1 = 47.1539;            % teta 1 effective in degrees
tteta_2 = 44.2203;            % teta 2 effective in degrees
teta1   = tteta_1*pi/180;      % teta 1 effective in radiant
teta2   = tteta_2*pi/180;      % teta 2 effective in radiant

tanteta1 = tan(teta1);
tanteta2 = tan(teta2);
costeta1 = cos(teta1);

for n       = 1:size(file,1);            %file incrementer
    fid     = fopen(file(n,1:size(file,2)),'r');
    data    = fscanf(fid, '%i %i', [2, inf]);
    ndata_1 = data(1,:);
    ndata_2 = data(2,:);
    u1      = polyval(px0917_1,ndata_1);   % wire 1
    u2      = polyval(px0917_2,ndata_2);   % wire 2

    for q = 1:size(u1,2);
      u(q) = (costeta1*u1(q))/(cos(teta1-atan((u1(q)/u2(q)-
             1)/(tanteta2*u1(q)/u2(q)+tanteta1))))*cos(atan
             ((u1(q)/u2(q)-1)/(tanteta2*u1(q)/u2(q)+
             tanteta1)));      % x-component of velocity

      v(q) = (costeta1*u1(q))/(cos(teta1-atan((u1(q)/u2(q)-
             1)/(tanteta2*u1(q)/u2(q)+tanteta1))))*sin(atan
             ((u1(q)/u2(q)-1)/(tanteta2*u1(q)/ u2(q)+
             tanteta1)));   % y-component of velocity
     end;

    u_mean(n)  = mean(u(1,1:size(u,2)));
    v_mean(n)  = mean(v(1,1:size(v,2)));
    u_prime    = u-u_mean(n);
    v_prime    = v-v_mean(n);
    clear data ndata_1 ndata_2;
    fclose(fid);
```

```
      for m = 1:size(u,1);
        uv_prime(m) = u_prime(m)*v_prime(m);
      end;

    u_rms(n)    = std(u);
    v_rms(n)    = std(v);
    uv_mean(n) = mean(uv_prime);

    fclose(fid);
    clear u1 u2 beta s u_prime v_prime uv_prime u v;
                % make some room
end;            % repeat for every file

clear n m fid file xsaved q pitot_vel press rho temp;
                % tidy up

*************************************************************
```

B: Physical Properties of Air at Standard Atmospheric Pressure

Temperature (°C)	Density, ρ (kg/m^3)	Dynamic Viscosity, μ (N.s/m^2)	Kinematic Viscosity, ν (m^2/s)	Speed of Sound, c (m/s)
-40	1.514	1.57×10^{-5}	1.04×10^{-5}	306.2
-20	1.395	1.63×10^{-5}	1.17×10^{-5}	319.1
0	1.292	1.71×10^{-5}	1.32×10^{-5}	331.4
5	1.269	1.73×10^{-5}	1.36×10^{-5}	334.4
10	1.247	1.76×10^{-5}	1.41×10^{-5}	337.4
15	1.225	1.80×10^{-5}	1.47×10^{-5}	340.4
20	1.204	1.82×10^{-5}	1.51×10^{-5}	343.3
25	1.184	1.85×10^{-5}	1.56×10^{-5}	346.3
30	1.165	1.86×10^{-5}	1.60×10^{-5}	349.1
40	1.127	1.87×10^{-5}	1.66×10^{-5}	354.7
50	1.109	1.95×10^{-5}	1.76×10^{-5}	360.3
60	1.060	1.97×10^{-5}	1.86×10^{-5}	365.7
70	1.029	2.03×10^{-5}	1.97×10^{-5}	371.2
80	0.9996	2.07×10^{-5}	2.07×10^{-5}	376.6
90	0.9721	2.14×10^{-5}	2.20×10^{-5}	381.7
100	0.9461	2.17×10^{-5}	2.29×10^{-5}	386.9
200	0.7461	2.53×10^{-5}	3.39×10^{-5}	434.5
300	0.6159	2.98×10^{-5}	4.84×10^{-5}	476.3
400	0.5243	3.32×10^{-5}	6.34×10^{-5}	514.1
500	0.4565	3.64×10^{-5}	7.97×10^{-5}	548.8
1000	0.2772	5.04×10^{-5}	1.82×10^{-4}	694.8

Note: Data from Munson et al. (1990)

IMAGE EVALUATION
TEST TARGET (QA-3)

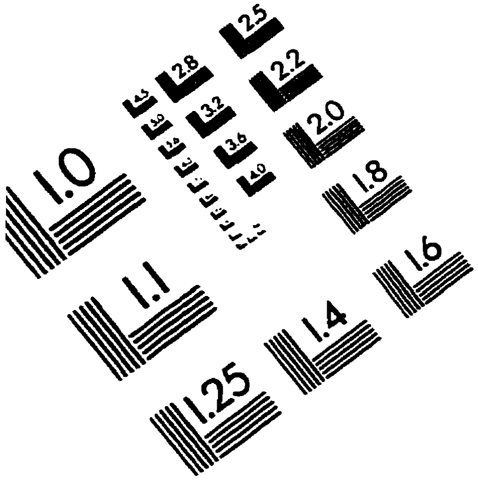

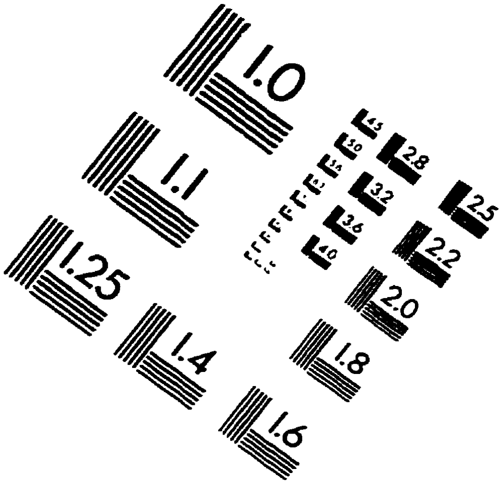

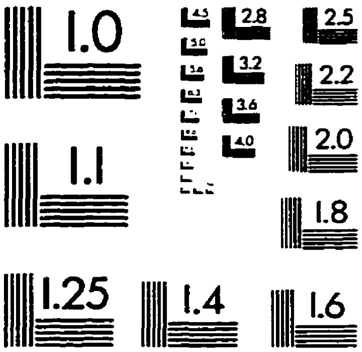

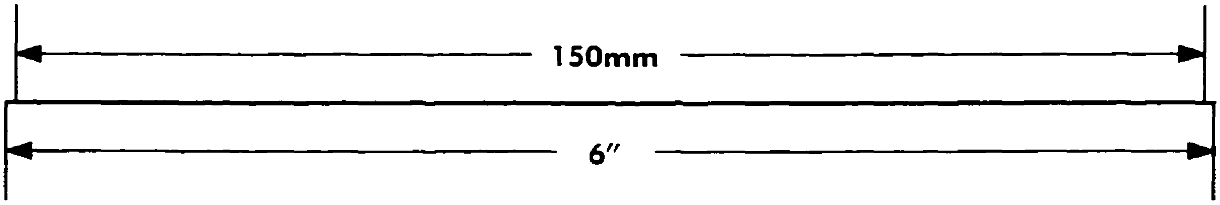

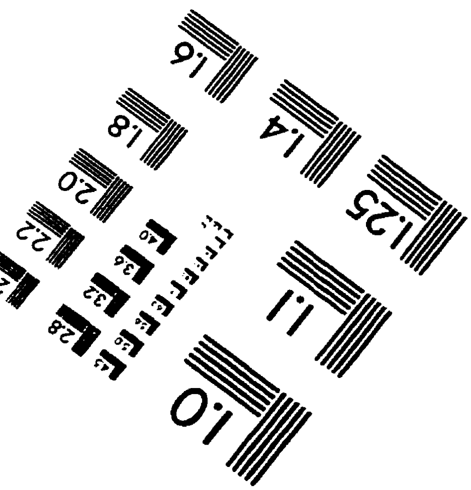

APPLIED IMAGE, Inc
1653 East Main Street
Rochester, NY 14609 USA
Phone: 716/482-0300
Fax: 716/288-5989